INFORMATION TO USERS

This dissertation was produced from a microfilm copy of the original document. While the most advanced technological means to photograph and reproduce this document have been used, the quality is heavily dependent upon the quality of the original submitted.

The following explanation of techniques is provided to help you understand markings or patterns which may appear on this reproduction.

1. The sign or "target" for pages apparently lacking from the document photographed is "Missing Page(s)". If it was possible to obtain the missing page(s) or section, they are spliced into the film along with adjacent pages. This may have necessitated cutting thru an image and duplicating adjacent pages to insure you complete continuity.

2. When an image on the film is obliterated with a large round black mark, it is an indication that the photographer suspected that the copy may have moved during exposure and thus cause a blurred image. You will find a good image of the page in the adjacent frame.

3. When a map, drawing or chart, etc., was part of the material being photographed the photographer followed a definite method in "sectioning" the material. It is customary to begin photoing at the upper left hand corner of a large sheet and to continue photoing from left to right in equal sections with a small overlap. If necessary, sectioning is continued again — beginning below the first row and continuing on until complete.

4. The majority of users indicate that the textual content is of greatest value, however, a somewhat higher quality reproduction could be made from "photographs" if essential to the understanding of the dissertation. Silver prints of "photographs" may be ordered at additional charge by writing the Order Department, giving the catalog number, title, author and specific pages you wish reproduced.

© Copyright

Robert Hall Manka

1972

RICE UNIVERSITY

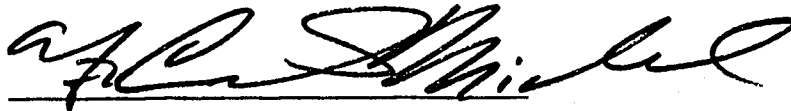LUNAR ATMOSPHERE AND IONOSPHERE

by

Robert Hall Manka

A THESIS SUBMITTED
IN PARTIAL FULFILLMENT OF THE
REQUIREMENTS FOR THE DEGREE OF

DOCTOR OF PHILOSOPHY

Thesis Director's Signature:

Houston, Texas

May, 1972

PLEASE NOTE:

Some pages may have

indistinct print.

Filmed as received.

TABLE OF CONTENTS

I.

LUNAR ATMOSPHERE AND IONOSPHERE

A.   ## History and Description of the Lunar Atmosphere

The brief history of the study of the lunar atmosphere is a fascinating story. Until the past couple of years, very little data was available about the moon's atmosphere and the studies have primarily been estimates based on knowledge of the lunar plasma and field environment. As pointed out by Manka and Michel (1971), the lunar atmosphere is a good example of a "prototype" planetary atmosphere as it has relatively straightforward sources and losses and interactions between the atmospheric constituents are negligible, though as we show in this thesis, interaction of the atmosphere with the lunar surface can be significant.

Early measurements looked for sunlight scattered by the lunar atmosphere and yielded only a relatively high upper limit of 10^{10} molecules cm^{-3} (Dollfus, 1956). The occultation of signals from radio stars was studied by Elsmore (1957) and Hazard et al. (1963), who deduced an upper limit on the election density of 10^2 to 10^3 cm^{-3}. The technique used then was to deduce how much neutral

atmosphere would be expected for this election density,
by calculating the fraction of the atmosphere that would
be ionized; neutral densities less than 10^5 to 10^6 cm^{-3}
were implied. We will show in this thesis that the rela-
tionship of neutral to ionized consituents will be con-
siderably altered when we consider removal of the ionized
particles by fields in the solar wind. With this relatively
sketchy experimental data available, several scientists
began, about 1960, to evaluate the lunar environment and
calculate properties of the resulting atmosphere. Öpik
and Singer (1960) and Öpik (1962) concluded that the sur-
face potential would be important for ejecting ions from
the atmosphere. They also concluded that a daytime number
density in the lunar atmosphere would be about 5 x 10^5
cm^{-3} and would be 50 to 70 percent CO_2 and 27 to 45 per-
cent H_2O (the water being created chemically from solar
wind hydrogen impact on the surface)! Errors in the
calculations stem from poor numbers for plasma temperatures
in the solar wind and neglecting interaction of the ions
with solar wind fields.

B. Recent Theories and Measurements

A series of more recent, comprehensive calculations were made by Bernstein et al. (1963), Hinton and Taeusch (1964), and Michel (1964), all of which looked at interaction of the atmosphere with the solar wind. Bernstein et al. considered the possible presence of Ar^{40} in the atmosphere due to election-capture decay of K^{40} in the upper 10 km of the lunar surface and release into the atmosphere; however, conclusions were not drawn about the interaction of ions with the solar wind fields and a very low ion temperature of 400 °K was assumed. Hinton and Taeusch did a closed calculation, balancing sources and losses, and concluded that Ne and Ar from the solar wind will be the primary constituents; however, they neglected interaction of ions with solar wind fields (which we see is the dominant interaction). Michel made a quantitative self contained calculation of atmospheric constituents based on two possible models for solar wind flow at the moon: undeviated flow and potential flow (deviated), and the loss rates for ions swept away along the flow lines were calculated.

While the above calculations summarized many of the

physical process in the lunar atmosphere, they had been carried to the point where further data was needed in order to define some of the variable parameters. Several important pieces of information came from lunar orbiter Explorer 35 (e.g. Colburn et al., 1967; Ness, 1968) which indicated that the solar wind impacts directly on the front side of the moon, leaving a plasma void behind the moon and perturbed plasma and magnetic field region at the solar wind-void boundary. Thus, the possible lunar bow shock does not appear to be present and the undeviated flow model is appropriate. However, we will show that a consequence of the ion dynamics is that loss from the atmosphere occurs from an area greater than just the limb regions.

Significant new information on the lunar atmosphere first became available from an unlikely source: the analysis of Apollo 11 lunar surface samples. There was evidence that, in addition to large amounts of solar wind gases trapped in the surface, there was also gas from the moon itself, and specifically that Ar^{40} was surface-correlated in the grains and thus was possibly trapped out of the lunar atmosphere (Heymann et al., 1970).

About this time calculations begun by <u>Manka and Michel</u>

(1970 a,b,c) on the dynamics of lunar ions showed that

ions are accelerated by the interplanetary electric and

magnetic fields and that some ions can impact the lunar

surface with sufficient energy to be trapped. In parti-

cular, they showed that atmospheric Ar^{40} can be trapped

efficiently enough to account for the anomalous amounts

found in lunar samples.

At about this same time, data began to return from

the first ALSEP experiments placed on the lunar surface

by Apollo 12. The Suprathermal Ion Detector Experiment

(SIDE) detected "cloudlike" sporadic bursts of ions

(<u>Freeman et al.</u>, 1971) while the solar wind spectrometer

saw ions from the solar wind and an S IV B impact on the

moon (<u>Snyder et al.</u>, 1971). An experiment of importance

to the lunar atmosphere was the measurement of the lunar

surface magnetic field, found to be of the order of 40

to 100 gamma (<u>Dyal et al.</u>, 1970 a,b, 1971 a) and indicat-

ing the absence of a global lunar field with attendant

implications of a source due to a hot lunar interior and

a resulting magnetosphere around the moon.

Related to the ion measurement was a measurement of

the neutral atmospheric pressure by the Cold Cathode

Gauge Experiment (CCGE); densities of about 10^5 cm^{-3}

were found from sunset through the night to sunrise, thus

providing a direct measurement of the lunar atmosphere

(Johnson et al., 1971). In a related brief review paper,

Johnson (1971) estimated the concentrations of various

species of the atmosphere in a manner similar to the

recent theoretical work discussed above.

Another exciting new measurement in the lunar program

was a direct measurement of some of the most common noble

gas elements in the solar wind. Previous satellite ex-

periments had measured the hydrogen and helium content

as well as some isotopes of oxygen; however, the Solar

Wind Composition experiment, carried to the moon on the

Apollo 11 and succeeding flights, measured the ratios of

the helium and neon isotopes (Geiss et al., 1970).

C.   Characteristics of the Lunar Atmosphere to be

     Calculated

A number of the results from this thesis have al-

ready been mentioned above in discussing the other work

done on the lunar atmosphere. The thesis makes one of

the next steps forward in the theory by examining the
acceleration of lunar ions by the interplanetary and sur-
face electric and magnetic fields. This acceleration model
has consequences for the dynamics of the lunar ionosphere.
The acceleration also has significant implications for the
study of the neutral atmosphere: the atmosphere is photo-
and charge-exchange ionized and lost due to acceleration by
the solar wind electric and magnetic fields. We will show
that the resulting trajectories allow loss from a portion
of the sunlit atmosphere that is much greater than just
the limb region.

We predict a number of properties of the dynamics of
the lunar ionosphere, including the direction, energy and
flux of ions. Consequences are that the relation that was
assumed by earlier researchers between the densities of
neutrals and ionized components was not correct. Neither
is the ion temperature of 400 $^{\circ}$K correct, as was assumed
in several papers. Because of the large ion trajectories
calculated by this model, we find that the exact flow
pattern of the solar wind is not very critical in calculat-
ing loss rates. Also, based on the model of ion dynamics,
we make some predictions about energy, flux and direction

of the ion events which are seen by surface ion detectors and we study some SIDE data, correlated with magnetometer data, which support the model. In addition, some characteristics of the "water vapor" event, seen by SIDE, are interpreted on the basis of this model.

Furthermore, the acceleration model is related to gases found in lunar samples and we calculate the trapping effectiveness of several noble gases and show that there can be an isotopic fractionation of the trapped atmosphere.

Finally, we use the model to calculate the density of neutral Ar^{40} in the lunar atmosphere from data obtained of lunar samples. Also, the total neutral density on the lunar atmosphere is calculated from ion detector data.

II.

LUNAR ORBIT AND MAGNETIC ENVIRONMENT

A.   Lunar Surface and Orbital Experiments

Since we will be using data from several lunar experiments, a brief discussion of these experiments and their data is in order. We primarily use data from the lunar surface SIDE and LSM and from the Ames Explorer 35 magnetometer. Very useful information is also obtained from the Solar Wind Composition experiment and the Solar Wind Spectrometer.

SURFACE EXPERIMENTS:

Supratherimal Ion Detector Experiment (SIDE):

The SIDE was carried on Apollos 12, 14 and 15 as part of the ALSEP (Apollo Lunar Surface Experiments Package). The instrument makes two basic measurements, the Total Ion Detector (TID) measures the total ion counts in a series of energy channels while the Mass Analyzer (MA) measures ions in various mass channels and at six relatively low energy steps. The schematic is shown in Figure 1. A summary of the measurements in the two parts of the instrument is:

Figure 1:   Block diagram of the SIDE
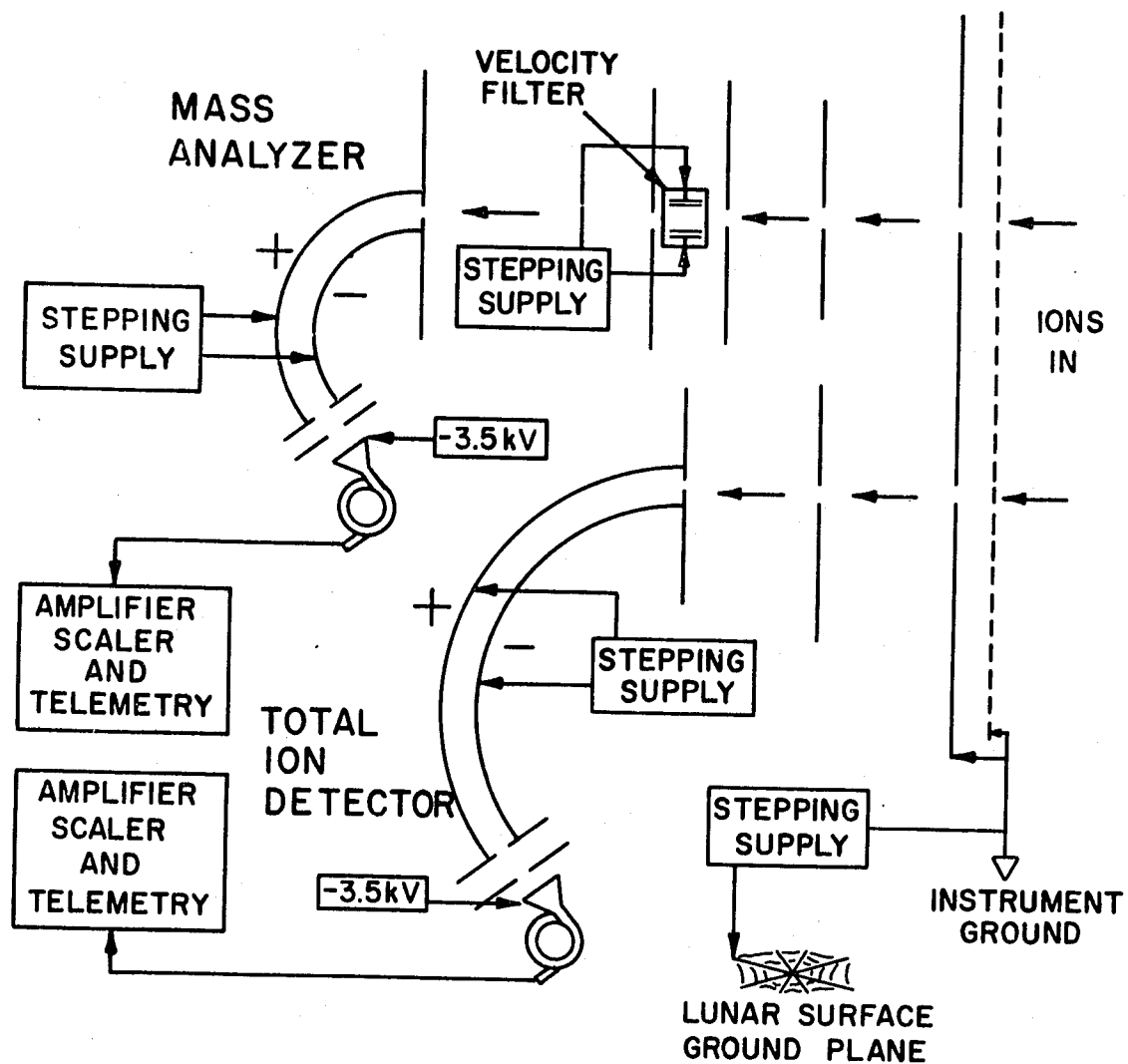
FIGURE I

TID   Measures: positive ion counts

       Energy range: 3500 ev to 10 ev in 20 steps

       Energy band: ~10% of each energy step

       Time to cycle through 20 energy steps: 24 sec.

       Time actually taking data at each step: 1.13 sec.

MA   Measures: positive ion mass ranges

       Mass ranges: 6 to 750 amu

       Range width: $\Delta m/m \simeq 0.2$ for low masses

       Energy range of measured ions: 48.6, 16.2, 5.4,

                                  1.8, 0.6 and 0.2 ev

The TID measures counts/SIDE frame, and calibration constants are used to convert to ion flux.

$$\text{Flux}_{\text{isotropic}} \left(\frac{\text{ions}}{\text{cm}^2 \text{ ster sec}} \right) = \frac{C}{G} \qquad (2\text{-}1)$$

$$\text{where } C \left(\frac{\text{Counts}}{\text{Sec}} \right) = \frac{\text{Counts}}{\text{SIDE frame}} \cdot \frac{1 \text{ SIDE frame}}{1.13 \text{ Sec}} \qquad (2\text{-}2)$$

$$\text{and} \qquad G = EFF \cdot A \cdot \Omega \qquad (2\text{-}3)$$

where   Eff = efficiency = $4.8 \times 10^{-2} \dfrac{\text{counts}}{\text{ion}}$

A = area = 0.24 cm^2

Ω = solid angle = 0.0086 ster.

so

$$G = 0.99 \times 10^{-4}$$

The differential flux is given by

$$\text{Diff flux}_{\text{isotropic}} = \frac{\text{Flux}_{\text{isotropic}}}{\Delta \mathscr{E}} \qquad (2\text{-}4)$$

where $\Delta \mathscr{E}$ = band width of energy channel
$= \sim 10\%$ of $\mathscr{E}$
$\mathscr{E}$ = channel energy

Generally, the SIDE data has been assumed to be isotropic and plotted per steradian (e.g. Freeman, 1972). However, as shown by Manka and Michel (1970a) and discussed in this thesis, the acceleration model predicts that ion fluxes will be very directional. Thus, we suggest here that for ions from the lunar atmosphere, the flux is approximately uni-directional and should be expressed as:

$$\text{Flux} \left(\frac{\text{ions}}{\text{cm}^2 \text{ sec}} \right) = \text{Flux}_{\text{isotropic}} \times 0.0086 \text{ ster.} \qquad (2\text{-}5)$$

Actually this is the flux into the 5° cone of acceptance of the SIDE, which is effectively a uni-directional flux. Similarly,

$$\text{Diff. Flux} \left(\frac{\text{ions}}{\text{cm}^2 \text{ sec ev}} \right) = \text{Diff. Flux}_{\text{isotropic}} \quad \text{x .0086 ster.}$$

$$(2-6)$$

The data format is shown in Figure 2. Shown in Figure 2a is a sample of one SIDE cycle of ion count data. The beginning time is Day 16, Hour 19, 1 min., 42.607 sec. Each of the numbers in the matrix is the number of counts at a given measurement energy. The top row of numbers represents one cycle through the measurement energies, the first value in the row being at 3500 ev with succeeding measurements at 3250, 3000, 2750, 2500, 2250, 2000, 1750, 1500, 1250, 1000, 750, 500, 250, 100, 70, 50, 30, 20 and finally, the last measurement on the right at 10 ev. The second line of the matrix begins measurements during a new energy cycle, beginning at 3500 ev again (see Lindeman, 1971, for a discussion of the matrix). Simultaneously, the Mass Analyzer obtains twenty mass steps (channels) for each of six different energies from 48.6 to 0.2 ev. Thus, a complete SIDE cycle is represented in the six line matrix of 120 measurements plus 8 housekeeping frames which occur between the data matrices. The time between frames is approximately 1.2075 seconds, though data is taken for only 1.13 seconds.

Figure 2a: Matrix of ion count data (see text)

Figure 2b: Differential fluxes corresponding to
              the first two rows of the ion count
              matrix

2a

16 19 1 42607

0	0	0	0	0	0	0	0	2	0	0	0	0	0	0	0	8	0	0	0	0	0	0
0	0	0	0	0	0	0	0	0	0	0	0	0	0	2	0	0	1	1	0	0	0	0
0	0	1	0	0	0	0	0	1	0	0	2	0	3	0	0	0	1	2	4	1	0	0
0	0	0	0	0	0	1	0	1	2	0	0	2	2	7	2	0	1	0	2	0	0	0
0	0	0	0	0	0	1	0	0	0	0	0	0	3	4	3	0	2	2	3	0	0	0

16 19 4 17166

2b

TIME IS 16 19 1

DIFFERENTIALS
2

0.	0.	0.	177.	0.	0.	0.	0.	0.	0.
0.	0.	0.	0.	0.	8850.	0.	0.		
0.	0.	0.	0.		2832.				

INTEGRAL FLUX= 699115. IONS/[SEC SQ CM STER]

DIFFERENTIALS

0.	0.	0.	0.	0.	0.	0.	0.	0.	0.
0.	0.	0.	0.	0.	0.	708.	0.		
885.	12642.	0.	5900.	0.					

INTEGRAL FLUX= 6611188. IONS/[SEC SQ CM STER]

FIGURE 2

Thus, the time between SIDE cycles is 128 x 1.2075 =

154.6 seconds = 2.59 minutes.

In addition, there is a "ground screen" which consists

of a loose mesh of wires deployed under the SIDE and in con-

tact with the lunar surface. The screen is connected to

one side of a stepped voltage supply, the other side of

which is connected to the internal ground of the detector

and to a small grid immediately above the ion entrance

apperture. The voltage is stepped from 0 to ± 27.6 volts

in 24 steps, one step for each SIDE cycle. The idea is

for the instrument potential to be stepped relative to the

lunar surface potential in order to compensate for surface

potentials and thus measure true ion energies. However,

as we show in the section on surface potentials and electric

fields, it is unlikely that the "ground screen" is at the

surface potential or that the instrument is actually stepped

in potential by the amounts applied by the voltage stopper.

Figure 2b is a sample of differential flux data from

the SIDE. The first block of data represents the same

measurements combined in the first line (energy cycle) of

the count matrix in 2a. Each count has been converted to

differential flux per steradian as given in equation (2-4).

Listed at the bottom of the set of differential fluxes is the integral flux summed over that energy cycle and the program used again calculates flux per steradian. As noted in equation (2-5), this number can be converted to uni-directional flux by multiplying by 0.0086 steradians.

The look direction of the Apollo 12 SIDE experiment is upward, 15° east of vertical, with the look angle lying approximately in the east-west plane. With respect to the solar ecliptic plane, the SIDE looks out nearly in the ecliptic (actually 3° south due to the landing site) and 15° east of vertically outward. The Apollo 14 SIDE is deployed about 6° east of Apollo 12, also looks approximately in the solar ecliptic, but 15° west of local vertical. Thus, the two look directions are nearly in the ecliptic but about 36° apart in azimuth. The Apollo 15 SIDE is deployed at a relatively high lunar latitude of $+26^{\circ}$ but the SIDE is canted at an angle so that it again looks in the ecliptic.

The SIDE experiments primarily see solar wind ions, magnetosheath ions, ions from the bow shock, and ions from the ambient lunar atmosphere or gas release events.

Lunar Surface and Portable Magnetometers:

The Lunar Surface Magnetometer (LSM) was deployed on Apollos 12 and 15 and consists of three orthogonal flux-gate sensors (Dyal et al., 1970a).

Measures: dc and slowly-varying vector magnetic
            fields

Range: 0 to   400 gammas

Frequency Response: dc to 2 Hz

Resolution: 0.2 gammas

The coordinate system used to plot data is a rectangular one with the x-axis vertically out from the surface, the y-axis tangent to the surface and pointing east, and the z-axis tangent to the surface and along the monidian to the north. Thus, for the Apollo 12 LSM, the x-axis is approximately in the ecliptic, y is to the east, and z is approximate vertically north out of the ecliptic.

The Lunar Portable Magnetometer (LPM) was deployed on Apollo 14 and because of its compact portable construction, was positioned and operated by the astronauts at several positions in the vicinity of the Lunar Module (Dyal et al., 1971a). The properties of the instrument are:

Measures: essentially dc vector magnetic fields

Range: 0 to ± 100 gammas, 0 to ± 50 gammas

Frequency response: dc to 0.01 Hz

Resolution: $\pm$ 1.0 gammas

The coordinate system for these measurements is the same as for the LSM.   Both instruments measure the total surface magnetic field, as discussed in section B of this chapter.

Solar Wind Composition Experiment (SWC):

The SWC is a passive experiment deployed by Apollo 11 and subsequent flights.   It simply consists of a high purity aluminum foil 30 cm wide and 140 cm long which is unrolled from a spool and held upright by a staff so that the solar wind impacts and is imbedded in the foil.   The foil is returned to earth by the astronauts and then analyzed in a mass spectrometer to determine the fluxes and isotopic ratios of solar wind elements (Geiss et al., 1970).   The fluxes of the more abundant isotopes are given in Table 1 (Geiss et al., 1970a).

Solar Wind Spectrometer (SWS).

The SWS consists of an array of seven wide-angle Faraday cups such as to be sensitive to solar-wind plasma from any direction above the local horizon.   The central

TABLE 1: Fluxes and Ion Abundances Ratios Determined for the Foil Exposure Periods of Apollo 11 and 12 (Geiss et al., 1970a)

	Apollo 11	Apollo 12
^{4}He Flux (cm^{-2} sec^{-1})	$(6.2 \pm 1.2) \times 10^6$	$(8.1 \pm 1.0) \times 10^6$
^{3}He Flux (cm^{-2} sec^{-1})	$(3.3 \pm 0.7) \times 10^3$	$(3.3 \pm 0.4) \times 10^3$
^{20}Ne Flux (cm^{-2} sec^{-1})	$(14 \pm 4) \times 10^3$	$(13 \pm 2) \times 10^3$
^{4}He/^{3}He	1860 ± 140	2450 ± 100
^{4}He/^{20}Ne	430 ± 90	620 ± 70
^{20}Ne/^{22}Ne	13.5 ± 1.0	13.1 ± 0.6
^{22}Ne/^{21}Ne		26 ± 12

Apollo 11 foil exposure period: July 21, 1969, 0335-0452 GMT

Apollo 12 foil exposure period: November 19, 1969, 1235 GMT, to
                                 November 20, 1969, 0717 GMT

cup faces in the direction of the local vertical and the other six face 60° off vertical. (Snyder et al., 1970). The instrument is designed to measure high fluxes from any desirable direction and is not highly sensitive to the lower fluxes of lunar ions. The instrument primarily sees solar wind and magnetosheath plasma but also saw ions from the Apollo 13 SIVB impact which apparently produced a relatively dense gas cloud over the lunar surface. We will comment on this event from the standpoint of our model and will also use solar wind velocity data from the SWS in order to calculate the interplanetary electric field for certain events.

Another particle detector of interest is the Charged-Particle Lunar Environment Experiment (CPLEE) which measures both ions and electrons from tens to a few thousand electron volts. An important measurement has been made of the high energy tail of the lunar surface photoelectron spectrum (O'Brien and Reasoner, 1971).

ORBITAL EXPERIMENTS:

Ames Explorer 35 Magnetometer (Ex 35 M):

Lunar orbiting Explorer 35 returned the first direct

data about the environment of the moon; in particular it appears that the solar wind impacts the moon directly leaving a void on the trailing side. Periselene of Explorer 35 is 1.4 R_M (lunar radii) and aposelene is 5.4 R_M. Figure 3 shows the orbit for Day 338, 1969 (D. S. Colburn, private communication); this orbit occurs during an ion event that we will study in considerable detail in later chapters (see Colburn et al., 1971, for a discussion of the Ex 35 magnetometer measurements).

When Explorer 35 is in the solar wind, the data is generally plotted in Solar Equatorial Coordinates where z is northward in a plane containing the solar direction and the solar spin axis, x is in the solar direction, and $y = \bar{z} \quad \bar{x}$. The polar angle $\theta = \sin^{-1} (B_z/B)$ and is the angle of $\bar{B}$ out of the ecliptic. $\emptyset$ is the azimuth angle, in the ecliptic plane, from the solar direction. Some properties of the instrument are:

Measures: dc and slowly-varying fields (≤ 0.5 Hz)

Ranges: 0 to ± 20, ± 60, ± 200 gamma

Resolution: Depends on digital windows and scale,

is 0.4, 1.2, and 4.0 gammas respectively

Sampling occurs every 2.05 second but is commutated among

Figure 3:   Plot of the Explorer 35 orbit

trajectory for Day 338, 1969.

The orbit occurs during an

ion event to be discussed later

START AT DEC. 3, 1969
337D 23H 0M

337/23

338/10

338/9

338/8

TO SUN

338/7

338/6

338/5

338/4

338/3

338/2

338/1
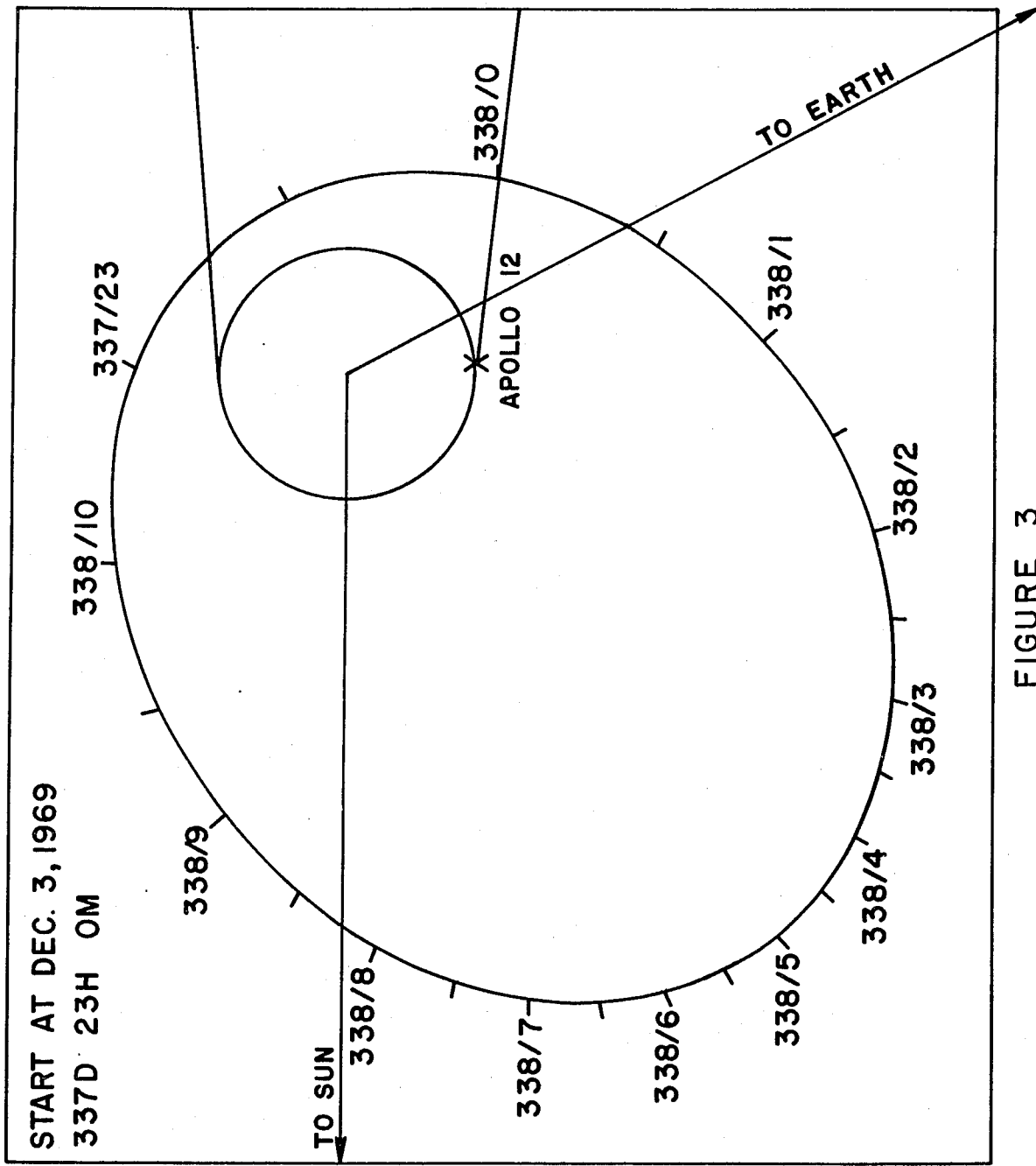
338/0

APOLLO 12

TO EARTH

FIGURE 3

the three ranges. Thus, a full vector measurement on the 20 gamma scale occurs every 6.14 seconds.

Other orbital experiments of general interest are the MIT Plasma Cup on Explorer 35 and the recently deployed partide detectors and magnetometer on the Apollo 15 Lunar Sub-Satellite.

B. Surface Magnetic Field

Magnetic measurements made on Explorer 35 indicated that the moon has a small intrinsic magnetic field (Colburn et al., 1967). No pronounced interaction of the solar wind with the lunar magnetic field was apparent in the Explorer 35 data. However, with the deployment of the LSM and LPM, our expectation of the surface magnetic field has essentially reversed. The steady surface field measured at the Apollo 12, 14, and 15 sites varies from about 6 to 100 gammas. Table 2 taken from Dyal et al. (1972) summarizes the field measurements at the three sites. Most of the values are about 40 to 100 gammas with only the Apollo 15 site being very "clean" at 6 gammas. Figure 4 shows the vector fields at the Apollo 12 and 14 sites which are generally down (with respect to the ecliptic) and into

TABLE 2: Remanent Magnetic Field Measurements at Apollo 15, 14, and 12 Sites (Dyal et al., 1972)

Site	Coordinates, deg.	Field Magnitude, gamma	Magnetic Field Components, gamma		
			Up	East	North
Apollo 15	26.4°N,3.5°E	6 ± 4	+4 ± 4	+1 ± 3	+4 ± 3
Apollo 14	3.7°S,17.5°W				
Site A		103 ± 5	-93 ± 4	+38 ± 5	-24 ± 5
Site C′		45 ± 6	-15 ± 4	-36 ± 5	-19 ± 8
Apollo 12	3.2°S,23.4°W	38 ± 3	-24.4 ± 2.0	+13.0 ± 1.8	-25.6 ± 0.8

Figure 4: Vector surface magnetic fields

measured at the Apollo 12 and 14

sites (Dyal et al, 1971b)

Figure 5: Some representative lunar surface

magnetic field data in LSM coordinates

for Day 338
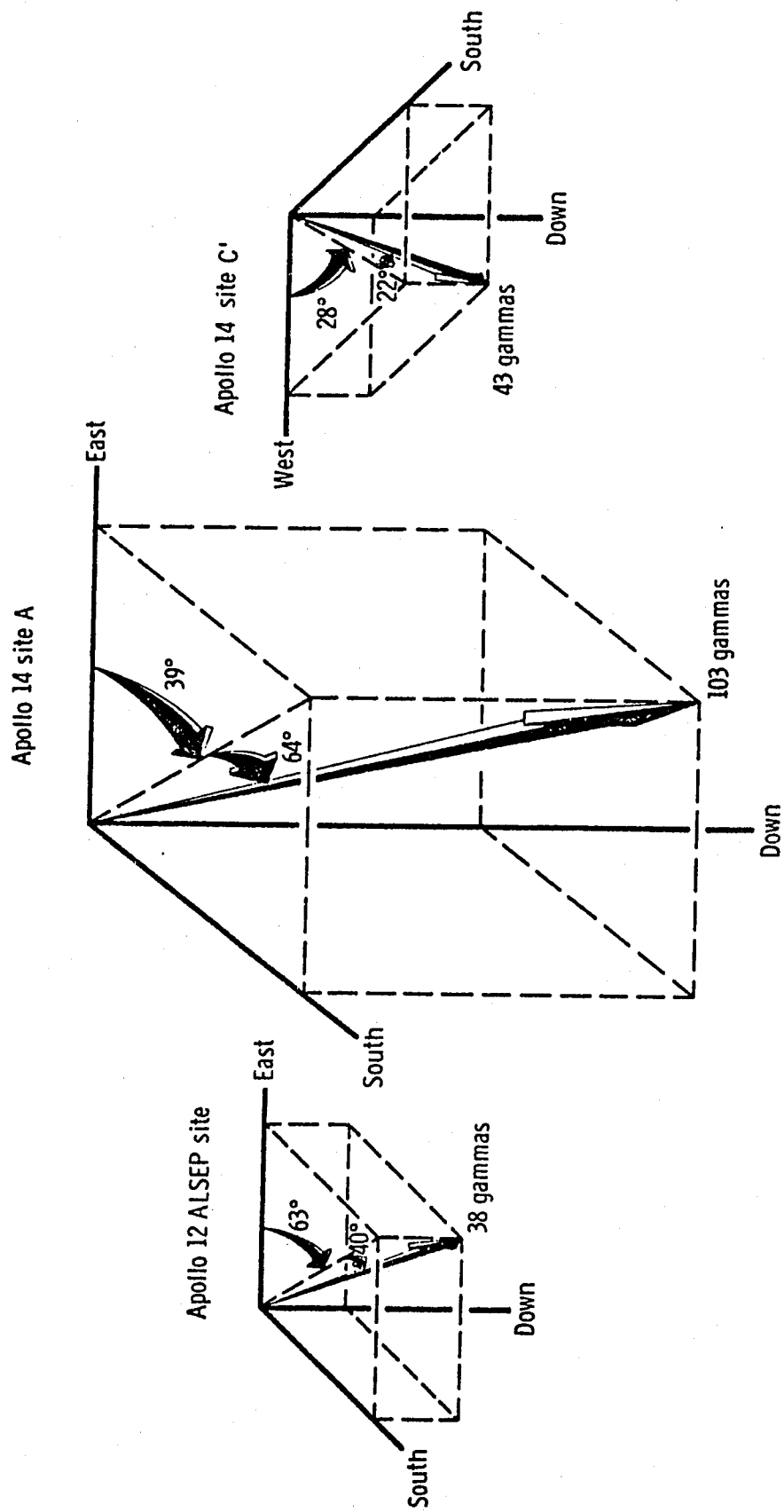
Apollo 14 site C'

South

Down

43 gammas

West

28°

22°

East

Apollo 14 site A

South

39°

64°

103 gammas

Down

Apollo 12 ALSEP site

East

South

63°

40°

38 gammas

Down

FIGURE 4

START YEAR 1969   TIME (MIN.)
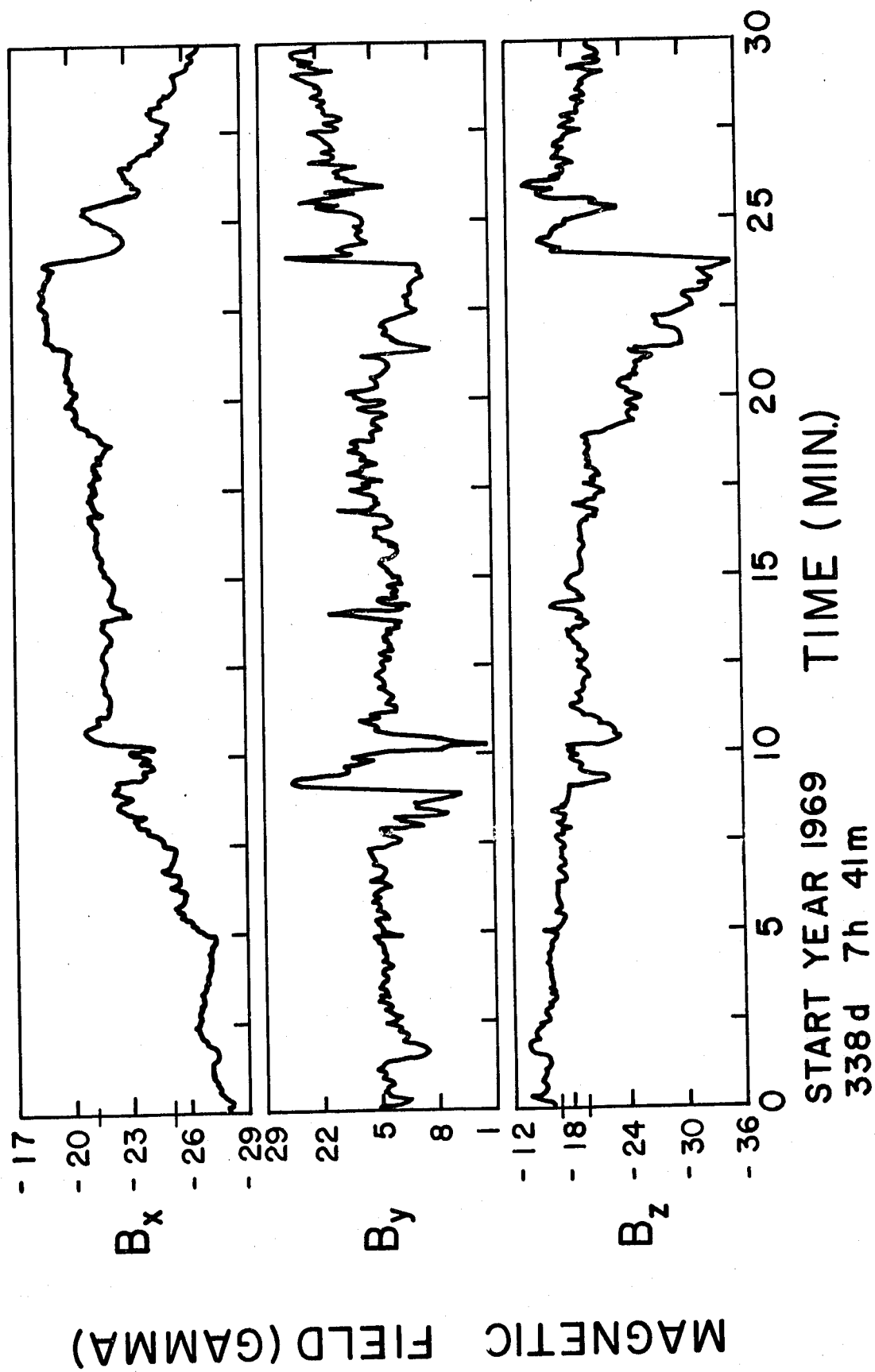338d 7h 41m

FIGURE 5

the moon.

The magnetic field measured at the surface is ex-
pressed by <u>Dyal et al.</u>, 1972 as

$$\bar{B}_A = \bar{B}_E + \bar{B}_S = \bar{B}_\mu + \bar{B}_P + \bar{B}_T + \bar{B}_D + \bar{B}_F \qquad (2-7)$$

where $\bar{B}_E$ ($\bar{B}_{sw}$ in the solar wind) is the total external
(driving) magnetic field while $\bar{B}_S$ is the steady reminant
field at the surface; $\bar{B}_\mu$ is the permeable magnetization
field, $\bar{B}_P$ is the poloidal field due to changing external
fields, $\bar{B}_T$ is the toroidal field generated by currents
driven by the solar wind electric field $\bar{E}_{sw} = -\bar{V}_{sw} \times \bar{B}_{sw}$,
$\bar{B}_D$ is the diamagnetic lunar cavity field and $\bar{B}_F$ is the
total field associated with hydromagnetic flow past the
moon. For comparison purposes, the Ex 35 magnetometer
measurements of $\bar{B}_{sw}$ are often plotted in LSM coordinates
and compared with the LSM data <u>Dyal and Parkin</u>, 1971 and
we will use data in this form later in this thesis. Shown
in Figure 5 is a sample of data courtesy of the LSM group
(P. Dyal, private communication) which shows the total
field at the lunar surface measured in LSM coordinates.

Our present knowledge about the surface magnetic field
would indicate that the solar wind impacts relatively

undeviated. However, lower energy lunar ions could be deviated and this question will be considered in more detail later.

C.   Lunar Orbit and External Magnetic Fields

The plasma properties of the lunar environment will be discussed in the next chapter; here we preview the external fields in these regions. Figure 6 shows the orbit of the moon around the earth at about 60 R_E. About three-fourths of the orbit is in the flowing solar wind and when the moon passes through the bow shock it enters the post shock magnetosheath which is also flowing and at 60 R_E is still "hotter" than the solar wind but is in the process of returning to solar wind conditions.

The properties of the interplanetary, or solar wind, magnetic field, $\bar{B}_{sw}$, have recently been reviewed by Schatten (1971). The average magnitude of $\bar{B}_{sw}$ is about 6 gammas and on the average, the field lies in the ecliptic at the "garden hose angle" of 45° to the sun-earth line. However, there is a great deal of fluctuation about these average values and quite different field orientations and magnitudes are not uncommon. As we shall see later, the

Figure 6:   Lunar orbit around the earth showing

the look directions of the Apollo 12,

14 and 15 SIDE experiments
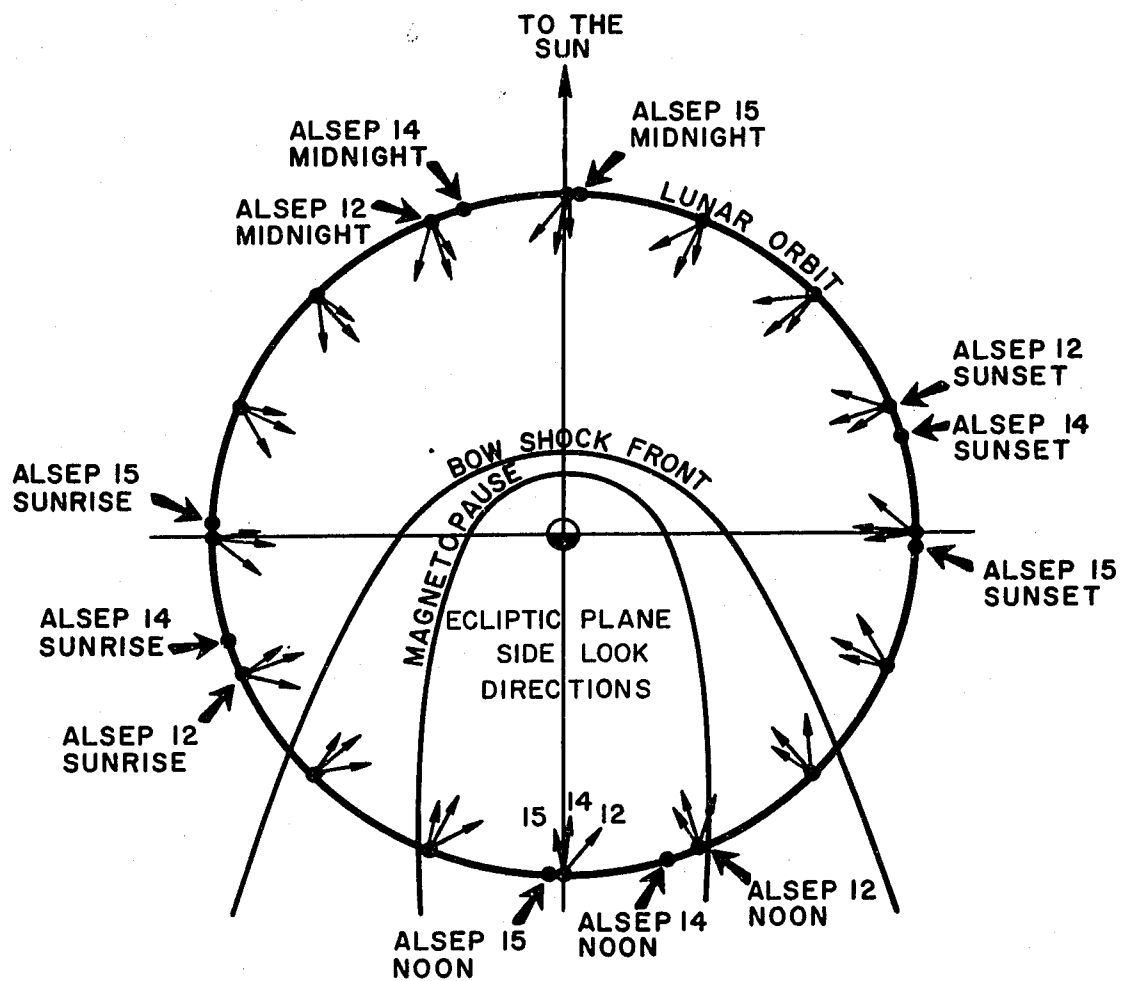
FIGURE 6

detection of lunar ions depends on just such fluctuations.

The magnetic field in the magnetosheath is similar to $\bar{B}_{sw}$, but the field is somewhat compressed from flowing around the magnetosphere and is thus stronger and changed somewhat in orientation from $\bar{B}_{sw}$. The magnetospheric tail is separated into upper and lower halves by the neutral sheet. The upper region has tail field directed toward the earth while in the lower region the field is directed away. The particle density in these regions is low but near the neutral sheet there is the relatively dense plasma sheet and at the neutral sheet itself, where the field approaches zero value, the entire pressure balance is maintained by the particles.

When the moon is in the solar wind, then in the lunar frame of reference there is an interplanetary electric field given by

$$\bar{E}_{sw} = - \bar{V}_{sw} \times \bar{B}_{sw} \tag{2-8}$$

A similar electric field exists in the magnetosheath while in the tail the plasma is stationary and thus there is no motional electric field. We will see later that $\bar{E}_{sw}$ plays a key role in ionospheric dynamics.

III.

LUNAR SURFACE PLASMA, POTENTIAL
AND ELECTRIC FIELD

In this thesis we primarily study acceleration of
lunar ions by the interplanetary electric and magnetic
fields. However, an ion which reaches the lunar surface
must first traverse the surface-related electric and mag-
netic fields and if these fields are strong enough, they
will greatly alter the ion energy and trajectory. The
surface magnetic field was discussed briefly in Chapter
II and its effects are considered again in Chapter IV.
Some knowledge of the surface potential and electric field
is especially important since the electric force alters
both the particle energy and direction; also the potential
might be of the same order as the energy of some lunar
ions. In order to apply the acceleration model with any
degree of confidence, we need an understanding of the
surface potential as a function of local lunar position.

A.   Discussion

The electrostatic potential of the moon and its effect

on the lunar surface environment has been discussed by a number of authors. The problem is complex due to the fact that there are the competing but interrelated charging mechanisms of positive and negative plasma flux to the surface, production of photo electrons, and production of secondary electrons, the magnitude of these not all being well known for the lunar surface. A dominant photoelectric effect was considered by Öpik and Singer (1960) to obtain potentials of +20 and +30 volts resulting in significant loss processes in the lunar atmosphere while Bernstein et al. (1963) estimated that the solar wind electron flux may exceed the photoelectron flux resulting in a neutral or negative surface potential and less effective ejection of ions from the lunar atmosphere. Grobman and Blank (1968) did a calculation of potential as a function of position over a portion of the sunlit side of the moon. The lunar surface electric field was estimated for the possible plasma environments by Manka and Anderson (1968, 1969) and Anderson and Manka (1968, 1970).

B.   Theory-Probe Equations

The current density per unit solid angle at the probe

due to a positive or negative species of the plasma is pro-
portional to the radial component of the velocity times the
distribution function, evaluated at the probe, integrated
over all velocity space; the current to the probe is given
by an integral of the current density over all solid angle.

For an isotropic, thermal plasma, the ambient plasma
distribution function at infinity is given by the Maxwell-
Boltzmann distribution and at finite distances from the
probe in the presence of a spherically summetric electro-
static potential $\phi(\bar{r})$, the distribution function is

$$f(\bar{r}, \bar{v}) = n \left(\frac{m}{2\pi kT} \right)^{3/2} \exp \left[\frac{-1}{2} \frac{mv^2}{kT} - \frac{e\phi(\bar{r})}{kT} \right] \qquad (3-1)$$

where n is the ambient plasma electron density, m is the
species mass, k is the Boltzmann constant, and T is the
species temperature. For a Maxwellian plasma with a super-
imposed flow velocity, v, the distribution at infinity of
the ambient plasma is

$$f(\bar{r}, \bar{v}) = n \left(\frac{m}{2\pi kT} \right)^{3/2} \exp \left[\frac{-m(\bar{v}-\bar{V})^2}{2kT} \right] \qquad (3-2)$$

For a stationary plasma, we use the basic probe equations

assuming spherical symmetry first derived by <u>Langmuir and</u> <u>Mott-Smith</u> (1926) and summarized by <u>Whipple</u> (1965) and <u>Fahleson</u> (1967); in general, these will be a good approximation. The solution is readily obtained for the isotropic plasma surrounding a spherical probe; however in the case of a flowing solar wind, a special expression for the plasma current must be used. This expression reduces to the stationary plasma solution when flow goes to zero (<u>Whipple</u>, 1959). The sheath can be assumed to be thin in comparison to the lunar radius for most of the cases considered (at least on the sun-ward side) and in addition, the dc conductivity at the lunar surface can be assumed to be very small so that the potential of the local lunar surface can be calculated as if the equilibrium condition at that point existed over the entire surface.

The local lunar surface will reach a potential such that the net current to it is zero ,

$$I_e + I_i + I_p + I_s = 0 \qquad (3-3)$$

where I_e = electron current, I_i = ion current, I_p = photoelectric current, and I_s = secondary electron current. Since these currents depend on the surface potential, the

equation can be solved for the equilibrium potential. The form of the expressions for current as a function of potential depends on whether the species is attracted or repelled.

The form of the current equations depends on whether the potential is positive or negative. The complete set of current equations for both stationary and flowing plasma and either positive or negative potentials is given in the Appendix. Below the equations for a couple of cases are discussed.

Positive Potential, $\phi > 0$

The current density due to repelled thermal plasma ions is

$$I_i = ne \sqrt{\frac{k\,T_i}{2\pi m_i}} \quad \exp\left(\frac{-e\phi}{k\,T_i}\right)$$

$$= I_{io} \exp\left(\frac{-e\phi}{k\,T_i}\right)$$

(3-4)

The current density due to attracted thermal plasma electrons is

$$I_e = -ne\sqrt{\frac{kT_e}{2\,m_e}}\ \frac{a^2}{r^2}\left[1 - \frac{(a^2 - r^2)}{a^2}\exp\left(\frac{-r^2}{a^2 - r^2}\ \frac{e\phi}{kT_e}\right)\right]$$

$$\simeq -ne\sqrt{\frac{kT_e}{2\,m_e}}\ \left[1 + \frac{2t}{r}\right]\ ,\ \text{thin sheath}$$

$$\simeq -ne\sqrt{\frac{kT_e}{2\,m_e}}\ ,\ \text{very thin sheath} \tag{3-5}$$

$$= I_{eo}$$

in which $a = r + t$, $\quad t = \lambda\,0.83\left(\dfrac{r}{\lambda}\right)^{1/3}\left(\dfrac{e\phi}{kT_e}\right)$ $\qquad$ (3-6)

with r the body radius, a the sheath radius, t the sheath thickness, and λ is the Debye length given by

$$\lambda = 6.9 \times 10^{-2}\sqrt{\frac{T}{n}}\quad\text{meters} \tag{3-7}$$

where T is in degrees Kelvin and n is per cm^3. For a probe large compared to the sheath thickness, the current is weakly dependent on potential since the area collecting the current is hardly increased by a large potential. I_{io}

and I_{eo} are the flux currents when the lunar potential is at the plasma potential (i.e., zero).

The current density of photoelectrons can approximately be written

$$I_p = i_p \exp\left(\frac{-e\phi}{kT_p}\right) \cos\theta \qquad (3\text{-}8)$$

where i_p is the photo current density from an area of the lunar surface at the plasma potential with normally incident sunlight and θ is the polar angle of the local surface with respect to the subsolar point. This expression assumes that for purposes of calculation the photoelectric distribution function can be taken to be Maxwellian with an equivalent temperature, T_p.

The secondary electron current is proportional to the flux of primary particles and is given by

$$I_s = (I_e \delta_e + I_i \delta_i) \exp\left(\frac{-e\phi}{kT_s}\right) \qquad (3\text{-}9)$$

where δ_e and δ_i are the secondary production coefficients for primary electrons and protons respectively and depend in a complicated fashion on the primary energy, angle of incidence and lunar surface material. In general

the coefficient for protons is assumed to be small, and
only for primary electrons with one hundred to several
hundred electron volts energy is the electron coefficient
likely to be significant.

For the flowing plasma, the thermal contribution to
the current (such as given in equation 3-5) is interrelated
with the flow contribution, and for example the electron
current becomes

$$I_e = \frac{nev_{me}}{2\sqrt{\pi}} \left[e^{-U_e^2} + \sqrt{\pi} \, U_e \left(1 + \mathrm{erf}(U_e) \right) \right] \qquad (3\text{-}10)$$

where

$$U = \frac{V \cos\theta}{v_m} \qquad (3\text{-}11)$$

and v_m is the species' mean speed. We note that when $V \to 0$,
that (3-10) reduces to (3-5); likewise, if the thermal
velocity, v, goes to zero, the equation reduces to the
pure flow current. Thus the equations in the Appendix give
the complete description of the plasma currents to the
sunlit hemisphere of the lunar surface.

Negative Potential, $\phi < 0$

When the thermal electron current exceeds the ejected electron currents the potential becomes increasingly negative until the remaining repelled electron current reaching the surface equals the positive current to the surface.

The repelled electron current density is given by (for a stationary plasma)

$$I_e = -ne \sqrt{\frac{kT_e}{2\pi m_e}} \quad \exp\left[\frac{e\phi}{kT_e}\right] \qquad (3-12)$$

while the attracted ion current has the same form as the attracted electrons in the previous section and in the limit of a very large body.

$$I_i = ne \sqrt{\frac{kT_i}{2\pi m_i}} \qquad (3-13)$$

The emitted photoelectron current density will be

$$I_p = i_p \cos\theta \qquad (3-14)$$

and the secondary current density is

$$I_s = I_e \delta_e + I_i \delta_i . \qquad (3-15)$$

C.   The Lunar Environment

Lunar Properties and Orbit

The orbit of the moon takes it through several environments as shown in Figure 6:   the solar wind, the earth's magnetosheath, and the geomagnetic tail. In addition to the general environment of the moon, the charging of the local surface will sepend on the direction of the photon and plasma fluxes and on the physical properties of the lunar surface. Also, it is important to note that the lunar orbital plane has an inclination with respect to the ecliptic plane of about 5 degrees and a relatively long precession period of 18.6 years; thus when the moon is in the geomagnetic tail, its position can vary as much as $\pm 5 \ R_E$ with respect to the ecliptic plane, depending upon the time of the year.

Solar Electromagnetic Radiation and Lunar Photocurrents

The solar spectrum and resulting photoemission has been discussed by several authors and is reviewed by Whipple (1965), who gives an integrated photocurrent form metals $I_p = 2 \times 10^{-9}$ to 8×10^{-9} amp cm^{-2} while Hinteregger et al. (1959) gave 4×10^{-9} amp cm^{-2}. If we assume an effective emissivity ϵ_o for metals corresponding to a photo current

of 5×10^{-9} amp cm^{-2}; then an emissivity $\epsilon = 10^{-1} \epsilon_o$

corresponds to a photocurrent of 5×10^{-10} amp cm^{-2}, etc.

The energy distribution of the emitted photoelectrons

is a complicated function of the energy of the photon and

the characteristics of the emitter (see, for example,

McDaniel, 1964); typical photoelectron energies are one to

several electron volts. Fahleson (1967) quotes equivalent

temperature, T_p, of 1 electron volt while Whipple found an

equivalent temperature of about 2 electron volts from

satellite photocurrents (private communication).

Secondary Electron Currents

It is difficult to estimate the role of secondaries

in determining the lunar potential, however, in a few cases

they may be important. If the secondary spectrum is

assumed to be quasi-Maxwellian, then an equivalent tempera-

ture is about 2 electron volts (Whipple, 1968). The

secondary coefficient, δ , is largest when the incident

primaries are electrons striking at oblique angles with

energies of 200 to 1000 electron volts and δ may be as

large as 4 to 6 for some insulators (McDaniel, 1964). One

case where the secondary electrons may be important is that

of the dark side of the moon in the plasma sheet where

electron temperatures are higher than in the solar wind; here the secondary current, like a weak photocurrent, may act to limit the large negative potentials which are expected as shown later in this chapter. The value of δ is difficult to predict since it depends on the material and the condition of the surface; however, by choosing values of 0.1, 0.8, and 2, it is possible to get a complete picture of the effect of the secondary current on the potential.

The Plasma Sheet

Measurements made on Vela satellites at 15 to 20 R_E have been reported by Bame et al. (1967) and by Bame (1968) who found a plasma sheet extending across the tail with a thickness of 4 to 6 R_E. The omnidirectional electron flux is typically 10^8 to 10^9 cm^{-2} sec which corresponds to an electron current range of 2×10^{-11} to 2×10^{-10} amp cm^{-2} while the average electron energy is 0.6 kev but varies from 200 ev to 12 kev. The electron density varies from 0.1 to 1 cm^{-3} and has an average of about 0.5 cm^{-3}. It is important to note for our calculations that the spectrum is quasi-Maxwellian so that it can be characterized with a temperature. The plasma pressure in the region of the neutral sheet is sufficient to balance the magnetic pressure

outside of the plasma sheet; thus even though there are large fluctuations of plasma energy and number density, the plasma pressure and flux are expected to stay more constant.

Similar results are reported by Vasyliunas (1968) of measurements made at distances of 20 to 24 R_E in the geomagnetic tail. The electron density is found to vary from 0.3 to 30/cm^3 and the average electron energy from 50 to 1600 ev.

Observations to greater distances in the geomagnetic tail were made during the outbound passage of Pioneer 7 (Lazarus et al., 1968) which stayed mostly in the plasma sheet until it passed through the side of the magnetosphere at an anti-solar distance of 40 R_E. Typical electron fluxes are $\dot{\Phi}_e = 1.25 \times 10^8$ cm^{-2} sec so $I_{eo} = 2 \times 10^{-11}$ amp cm^{-2}; the number density and thermal speed stay fairly constant throughout the flight.

The Low-Density Regions

From the data reported it is clear that the tail regions above and below the plasma sheet contain a plasma with only relatively low number and energy densities and that the magnetic field provides most of the pressure; we

will refer to these regions as the low density or high latitude regions. The Vela detectors were able to see some high latitude plasma and Bame (1968) shows a sample spectra. The average electron energy is about 70 ev and the proton energy appears to be somewhat higher and an electron density of 0.04 cm^{-3} was calculated. If we take $n \leq 0.05$ cm^{-3} and $\bar{E}_e = 50$ ev, then $\Phi_e \leq 6 \times 10^6$ cm^{-2} sec and $I_{eo} \leq 10^{-12}$ amp cm^{-2}. Since this is a magnetosheath like plasma, if we take the same number density for ions and an average energy $\bar{E}_i = 500$ ev, then $\Phi_i = 4.5 \times 10^5$ and $I_{io} = 7 \times 10^{-14}$ amp cm^{-2}.

Further measurements will give more exact information on the plasma parameters at 60 R_E, whether there is a net flow toward or away from the earth and the thickness of the sheet. Because of the shift of the location of the plasma sheet with the tilt of the geomagnetic poles, along with the ± 5 R_E latitude variation in the lunar orbit, it is possible that the moon will not be in the plasma sheet on all passes but will instead be in the low density region.

Plasma Fluxes in the Solar Wind

The average properties of the solar wind at 1 AU have been reviewed by several authors (Dessler, 1967; Axord, 1968).

Some average properties which we will use for our calculations are a flow velocity V_{sw} = 430 km/sec, a proton flow energy E_{swi} = 1 kev, superimposed thermal temperatures $T_i \approx T_e \approx$ 10 ev, particle densities $n_i = n_e = 10/cm^3$ with a range of 5 to $15/cm^3$.

On the dark side of the moon, while there is generally a plasma void, we expect that there will be a few high temperature particles from the solar wind which reach the lunar surface by traveling along magnetic field lines. In the absence of the interplanetary magnetic field, the condition for a particle flowing in the solar wind to reach a given point on the lunar surface is that its transverse thermal velocity be great enough that the particle velocity vector in the lunar system be at least tangent to the lunar surface at that point. The consequence is that increasingly higher temperatures are required to reach the surface at locations approaching the antisolar point. However, we will not calculate the plasma fluxes quantitatively as a function of position since two factors strongly modify this picture: one is that the presence of the interplanetary magnetic field will introduce a large asymmetry in the fluxes; the other factor is the apparently significant

affect on particle motion by the flow structure at the edge
of the lunar wake. However, it is apparent that ion energies
of the order of the flow energy are required to reach some
positions on the dark side.

A summary of some possible, average plasma properties
at 60 R_E are given in Table 3.

D.   The Lunar Surface Potential

There are three quite different plasma environments
for the moon: the solar wind, possibly the plasma sheet of
the geomagnetic tail, and the low density plasma in the
high latitude regions of the tail; the magnetosheath is not
considered in detail as it is similar to the solar wind.
The potential is found by solving equation (3-3) using the
appropriate expressions for the currents depending on
whether the ambient positive or negative current dominates.

Moon in Solar Wind

The most likely answers to the question of the sign
of the potential of the lunar surface in the solar wind can
now be formulated. In the absence of an external magnetic
field, the deciding parameter on the sunlit surface is the
photoelectric emissivity; it appears that for most of the

Table 3: Estimated properties of the geomagnetic tail plasma at 60 R_E. Question marks indicate uncertainty in the value(s).

	Flux Φ (cm^{-2}sec^{-1})	Current I_o (amp/cm^2)	Average Energy E (kev)	Energy Range E (kev)	Average Density n(cm^{-3})	Average Density Range n(cm-3)
Plasma Sheet						
Electrons	10^8 to 10^9	2×10^{-11} to 2×10^{-10}	0.6	0.3 to 1	0.5	0.1 to 1
Protons	10^7 to 10^8	10^{-12} to 10^{-11}	5.0	3 to 10	0.5	0.1 to 1
High Latitude Magnetotail						
Electrons	$\lesssim 6 \times 10^6$	10^{-12}	0.05 (?)	(?)	0.05(?)	(?)
Protons	$\lesssim 5 \times 10^5$	$\lesssim 7 \times 10^{-14}$	0.5 (?)	0.2 to 1(?)	0.05(?)	(?)
Magnetosheath						
Electrons	5×10^8	10^{-10}	0.025	(?)	10	5 to 20 (?)
Protons (thermal)	10^7	2×10^{-12}	0.25	(?)	10	5 to 20 (?)
Solar Wind						
Electrons (thermal and flow)	8×10^8	1.3×10^{-10}	0.010	0.006 to 0.020	10	4 to 15
Protons (flow)	4×10^8	7×10^{-11}	1.0	0.5 to 1.5	10	4 to 15

values in the expected range of emissivities that the
photocurrent will exceed the plasma electron current and
the central area of the sunlit side will be positive.
The potential for different values of ϵ as a function of
angle from the subsolar point is shown in Figure 7 and
sketched in Figure 8. Note that the thermal electron
current in the solar wind dominates as the angle approaches
90° and that the potential goes to -38 volts at the solar
wind terminator.

Moon in Geomagnetic Tail

Plasma Sheet:

Using the equations for a stationary plasma and the
currents from the lower end of the expected range in Table
3, we calculate that at the subsolar point the potential
varies from +1.8 to +20 volts and is equal to +11 volts for
$\epsilon = \epsilon_o$.

The potential at the terminator and on the dark side
will tend to be negative and since the plasma temperature
is high, large negative potentials could exist. However,
the secondary current will tend to limit these potentials
and could even make the surface potential positive. For
the plasma currents $I_{eo} = 2 \times 10^{-11}$ amp cm^{-2} and $I_{io} = 10^{-12}$

Figure 7:   Plot of the lunar surface potential

as a function of angle from the sub-

solar point.   Potentials are calculated

for five effective photoelectron

emissivities.

Figure 8:   Sketch of the expected potential and

field distribution when the moon is

in the solar wind.   The interplanetary

magnetic field is neglected.

FIGURE 7

SOLAR WIND

MOON
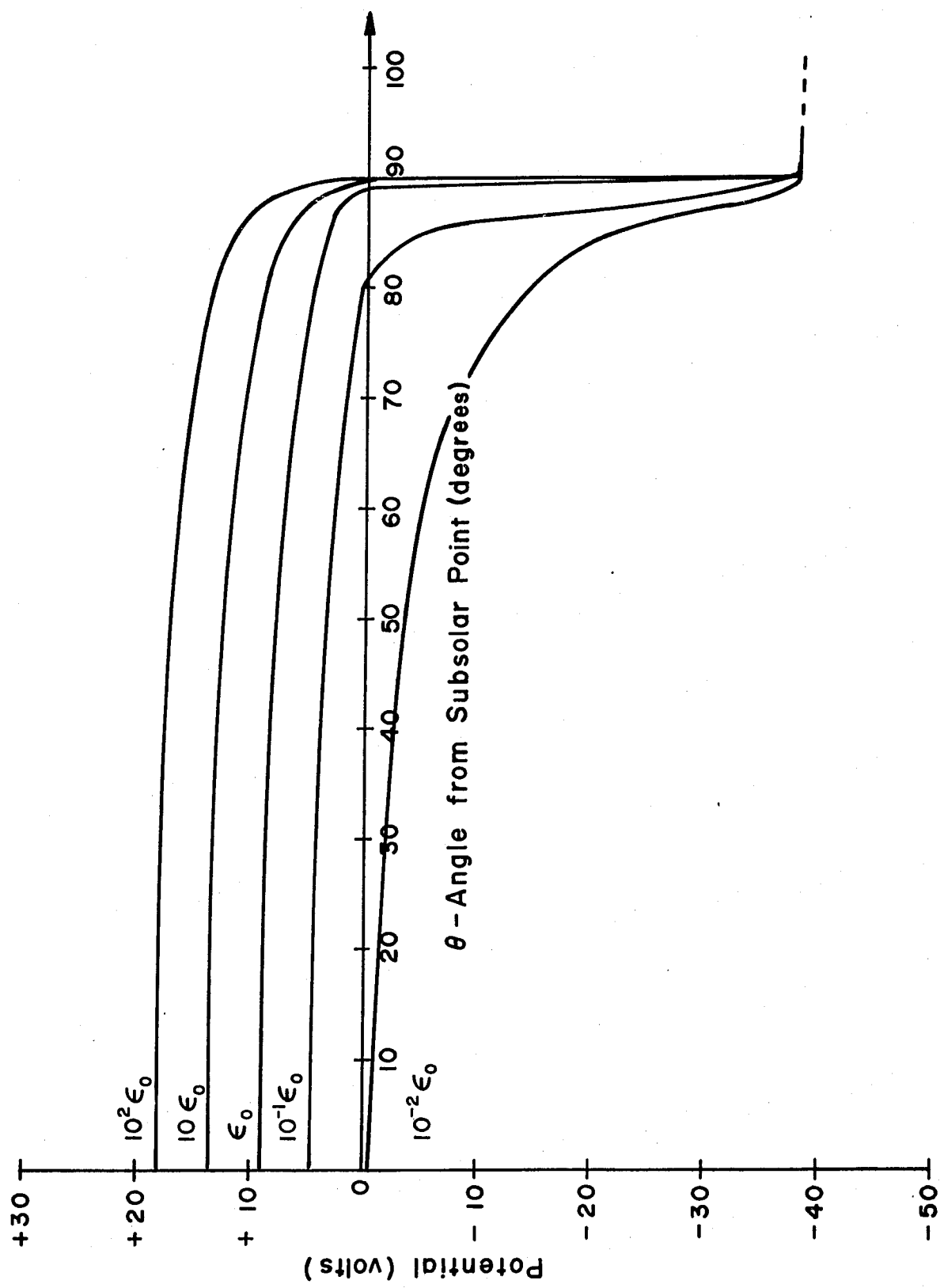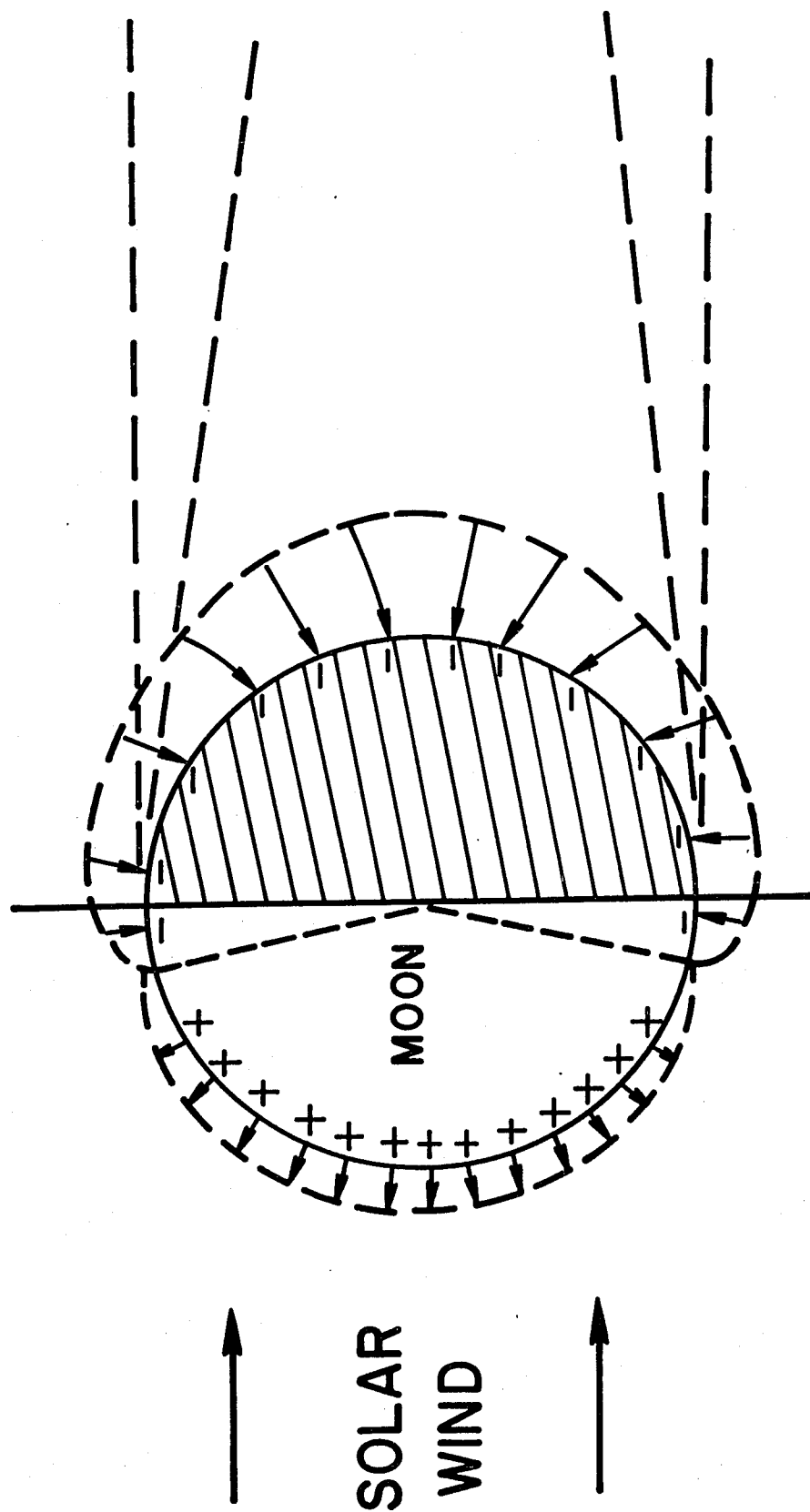
FIGURE 8

amp $\overline{cm}^2$ then $I_{io} = 0.05 \, I_{eo}$ and $\delta_{ec} \simeq 0.95$ is the critical value for crossover from negative to positive potential. Assuming that the above current ratios occur uniformly from the terminator over the entire dark side, and using the approximation that the sheath is very thin, then the potential is constant and is given by Table 4.

TABLE 4:   Potential at terminator and over the dark side
           when the moon is in the plasma sheet, as a
           function of secondary electron coefficient.

Secondary Coefficient δ	Potential at Terminator and on Dark Side (volts)
0	-1800
0.1	-1730
0.8	- 830
$\delta_{ec} = 0.95$	~ 0
2	+ 1.5

Since a reasonable estimate for the lunar secondary coefficient could be either less than or greater than the critical value, the range of secondary coefficients from 0.1 to

2 should be considered. The interesting effect on the
potential is that if the secondary coefficient is greater
than δ_{ec}, then the potential will be several hundred
volts negative and will vary with the plasma sheet electron
temperature.

High Latitude Regions

As was pointed out when the plasma fluxes were dis-
cussed, at certain times conditions are favorable for the
lunar orbit through the tail to be out of the plasma sheet
and in the high latitude region. From Table 3 the plasma
currents are quite low, $I_{eo} = 10^{-12}$ amp cm^{-2} and $I_{io} =$
7×10^{-14} amp cm^{-2}, so that the photocurrent will dominate
over most of the sunlit surface. The potential at the sub-
solar point varies from +8.0 to +26.4 volts for $\epsilon = 10^{-2} \epsilon_o$
and we get +17.2 volts for $\epsilon = \epsilon_o$. At the terminator the
potential goes to -135 volts which is simply the probe
potential corresponding to the given ion and electron
temperatures.

It is important to note that the recent measurements
of lunar surface photoelectrons by CPLEE (O'Brien and
Reasoner, 1971) could increase these subsolar potentials.
They measure the high energy tail (>40 eV) of the spectrum

and find the expected power law rather than Maxwellian response. In all calculations in this chapter we have used a Maxwellian spectrum and in the other regions when the plasma fluxes are greater, then the quasi-Maxwellian peak of the photoelectron spectrum determines the potential. However, in the low density regions, the plasma electron flux is so low that it is sufficiently balanced by the high energy tail of the photoelectron spectrum whose power law distribution may give larger positive potentials when equation (3-3) is solved.

E. Surface Electric Field

We can now immediately calculate the surface electric field in the plasma sheath. When the currents determining the potential are Maxwellian then the surface field decays exponentially above the surface, and the field at the surface is given by

$$E = \frac{\phi}{\lambda} \qquad\qquad (3\text{-}16)$$

where λ is the Debye length which is determined by the density and temperature of the attracted species of the plasma. All of the relevant parameters and the resulting

fields are summarized in Table 5.

F.   Relation to Ion Dynamics and Lunar Atmosphere

The concepts and results developed in this chapter will

be of considerable use in the proceeding discussion of the

atmosphere and ionosphere.

As mentioned earlier, the surface electric field con-

stitutes one mechanism for the ejection of ions from the

lunar atmosphere. We will show in this thesis that the

surface field determines the initial conditions on the tra-

jectories of some lunar ions. Of even greater importance

to this thesis, the surface potential can affect the energies

of ions observed at the lunar surface and the potentials

determined in this chapter allow us to proceed with confi-

dence when we calculate the energy given to ions by the

interplanetary electric field.

Futhermore, in some cases, such as ion trajectories to

the dark side of a moon in the solar wind, the surface

potential may be a major source of ion energy. It is even

possible that some lunar atmosphere ions, which are

accelerated toward the dark side by the interplanetary fields,

could then be further accelerated by the dark side surface

TABLE 5: Electric potential and field at the lunar surface for different plasma environments.

POSITION OF MOON	LOCATION ON SURFACE	T (ev)	λ (m)	Φ (volts)	E (volts/m)
SOLAR WIND	SUBSOLAR	$T_p = 2$	0.41	9.0	22
"	TERMINATOR	$T_i = 10$	7.4	-38	-5.1
HIGH LATITUDE TAIL	SUBSOLAR	$T_p = 2$	0.41	17.2	42
"	TERMINATOR AND DARK SIDE:	$T_i = 500$	738	-135	-0.18
PLASMA SHEET	SUBSOLAR	$T_p = 2$	0.41	11.0	27
	TERMINATOR AND DARK SIDE.($\delta = 0$):	$T_i = 5 \times 10^3$	744	-1800	-2.4
	TERMINATOR AND DARK SIDE ($\delta = 2$):	$T_s = 2$	4.6	1.5	0.33

electric field and given sufficient energy for implantation.

IV.

ION DYNAMICS

A.   Acceleration of Atmospheric Ions

As we show in this chapter, the principal acceleration

of lunar ions is by electric and magnetic fields in the

solar wind.

With respect to lifetimes against photo- and charge-

exchange ionization of about 10^6 to 10^7 seconds, atmospheric

species other than hydrogen and helium can generally be

considered to be gravitationally bound. For a lunar sur-

face temperature of $400^{\circ}K$, monatomic nitrogen has a mean

life against thermal escape of about 10^7 seconds (Michel,

1964); however, since diffusion times to the terminator are

generally less than 24 hours, an average surface tempera-

ture of $300^{\circ}K$ can be used for the surface nearer to the

terminator and carbon can be considered bound. Hydrogen

and helium will be in an outflow-inflow equilibrium but

their density distribution as a function of height will

not obey the scale height law of the heavier species.

The number density of bound species decreases approximately

exponentially with height. This can qualitatively be seen

from the fact that a Maxwellian gas in a slowly varying

potential field, $\phi(\bar{r})$, has a spatial distribution

$$n(r) = n_o e^{\frac{\phi(\bar{r})}{kT}} \quad . \tag{4-1}$$

If r is the height in the lunar atmosphere, and we assume

the vertical scale of the atmosphere to be small compared

to the lunar radius, then $\phi(\bar{r}) \simeq mgr$, so that

$$n(r) \simeq n_o e^{\frac{-r}{h}} \tag{4-2}$$

where h is the scale height for the species given by

$$h = \frac{kT}{mg} \tag{4-3}$$

and n_o is the density per cm^3 at the surface, k is the

Boltzmann constant, T and m are the species temperature

and mass and g is the lunar gravitational acceleration.

The Ar^{40} scale height is about 50 km on the sunlit hemisphere.

The approximately Maxwellian distribution in the atmosphere

is maintained by repeated collisions with the lunar surface .

Interplanetary Electric and Magnetic Fields:

We examine the transformation equations which give rise to the interplanetary electric field. If the lunar frame of reference is taken to be the stationary (unprimed) frame, the solar wind frame the moving (primed) frame, and we assume that a solar wind velocity $\bar{V}$ and magnetic field $\bar{B}$ are measured in the lunar frame, then the fields in the moving and rest frames are simply related.

We first look at the special case where $\bar{B}$ is perpendicular to $\bar{V}$. The fields parallel to the flow velocity are

$$\bar{B}'_{\parallel} = \bar{B}_{\parallel} = 0, \quad \bar{E}'_{\parallel} = \bar{E}_{\parallel} \doteq 0 \tag{4-4}$$

while the fields perpendicular to $\bar{V}$ are:

$$\bar{B}'_{\perp} = \gamma\,(\bar{B}_{\perp} - \frac{\bar{V} \times \bar{E}}{c^2}) = \gamma\,(\bar{B} - \frac{\bar{V} \times \bar{E}}{c^2}) \tag{4-5}$$

and $\quad \bar{E}_{\perp} = \gamma\,(\bar{E}_{\perp} + \bar{V} \times \bar{B}) = \gamma\,(\bar{E} + \bar{V} \times \bar{B}) \tag{4-6}$

where $\gamma = (1 - V^2/c^2)^{1/2}$. However, since the solar wind is a good conductor, we expect $\bar{E} = 0$ in its vest frame. This implies that

$$\bar{E} = - \bar{V} \times \bar{B} \tag{4-7}$$

If $\bar{B}$ is not perpendicular to $\bar{V}$, then

$$\bar{B}'_{\shortparallel} = \bar{B}_{\shortparallel} , \quad \bar{E}'_{\shortparallel} = \bar{E}_{\shortparallel} = 0 \tag{4-8}$$

and $\quad \bar{B}'_{\perp} = (\bar{B}_{\perp} \frac{-\bar{V} \times \bar{E}}{c^2})$

$$\bar{E}'_{\perp} = (\bar{E}_{\perp} + \bar{V} \times \bar{B}) = 0 \Rightarrow \bar{E} = -\bar{V} \times \bar{B} \tag{4-9}$$

But solving this last expression for $\bar{V}$ gives

$$\bar{V}_D = \frac{\bar{E} \times \bar{B}}{B^2} = \text{drift velocity} \tag{4-10}$$

which would not be along the original direction of $\bar{V}$.

Actually, as pointed out by Dessler (1967), there are two

components of the solar wind velocity with respect to the

magnetic field direction:

$$V_{\perp} = V_D = \frac{B_{\perp}}{B} = V \cos \theta = \text{drift across } \bar{B} \tag{4-11}$$

$$V_{\shortparallel} = V \sin \theta = \text{drift along } \bar{B} \tag{4-12}$$

and the solar wind flows with velocity $\bar{V}$.

In this thesis we are primarily studying the accelera-

tion of ions formed at rest in the lunar atmosphere. Thus

the initial velocity is essentially zero and the particle

trajectory is in a plane defined by $\bar{V}_D$ and $\bar{E}_{sw}$; the equa-

tions in this chapter are general and describe trajectories

in this plane with $|\bar{V}_D| = |\bar{V}_{sw}| \cos\theta$. A simplifying

situation exists when $\bar{B}_{sw}$ is perpendicular to $\bar{V}_{sw}$; this may

help in understanding a drawing such as Figure 11 as the

plane of the trajectories simply becomes the noon-midnight

maridian plane. However Figure 11 can be interpreted

exactly with the ion trajectories occuring in a cross section

plane, containing $\bar{V}_D$ and through the center of the moon.

Such a plane essentially defines a "magnetic longitude", in

analogy to the "electric latitude" to be introduced later.

In other words, the ion trajectories are determined by $\bar{E}_{sw}$

and $\bar{B}_{sw}$, and these fields define the relevant coordinate

system to be used. A sketch of the top view of the moon

showing the relative orientations of $\bar{V}_D$, $\bar{V}_{sw}$ and $\bar{B}_{sw}$ is

given in Figure 9.

Trajectory Equations

Whether an ion, once formed, escapes or is accreted

will be determined primarily by electric fields at the lunar

surface and in the interplanetary medium. The interaction

Figure 9: Sketch of top view of the moon showing

the solar wind velocity, and the drift

velocity which is orthogonal to $\bar{B}_{sw}$;

when $\bar{B}_{sw}$ is perpendicular to $\bar{V}_{sw}$, then

$\bar{V}_D$ is along $\bar{V}_{sw}$. The ion trajectory is

always in a plane parallel to the plane

defined by $\bar{V}_D$; however for simplicity,

in some figures the trajectory plane is

idealized to the noon-midnight meridian

plane, which is equivalent to assuming

that $\bar{V}_D$ is along $\bar{V}_{sw}$.
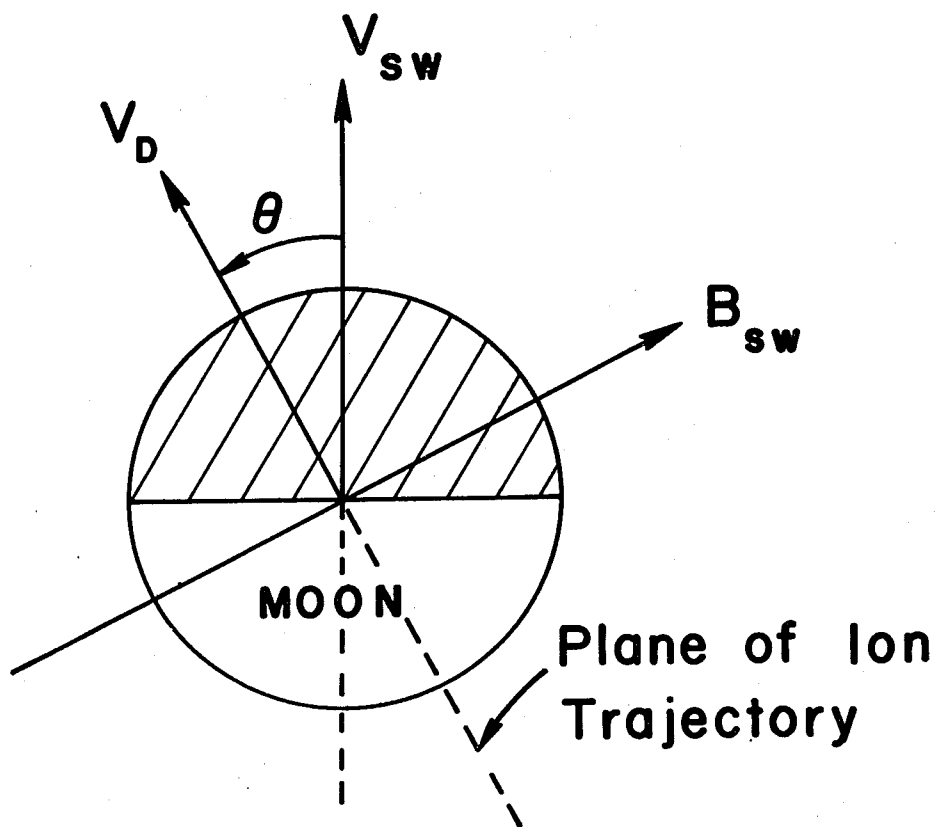
FIGURE 9

of lunar ions with the solar wind is best treated in a

frame of reference at rest with respect to the moon. As

discussed previously, in this system there is an inter-

planetary electric field given by

$$\bar{E}_{sw} = - \bar{V}_{sw} \times \bar{B}_{sw} \tag{4-13}$$

where $\bar{V}_{sw}$, $\bar{B}_{sw}$, and $\bar{E}_{sw}$ are, respectively, the solar wind

velocity, magnetic field, and electric field. In addition,

the lunar surface electric field will moderate incoming ion

energies; this surface potential could have a significant

effect for some locations on the moon. However, the surface

field is confined to the lunar plasma sheath, with a thick-

ness of tens of meters when the moon is in the solar wind,

and we shall see that most of the ions are formed outside

of this sheath.

Ions Formed Inside the Plasma Sheath

We will make the simplifying assumptions that the ion

is injected upstream into the solar wind from the lunar sur-

face, and in a direction opposite to $\bar{V}_D$, so that it is

initially going in the -x direction with a velocity v_o as

shown in Figure 10. In the simplifying case where $\bar{B}_{sw}$ is

Figure 10: Illustrative sketch of the orbit of an

ion formed inside the plasma sheath at

the lunar surface and injected upstream

into the solar wind where it is acceler-

ated. The thickness of the plasma sheath

is exaggerated.
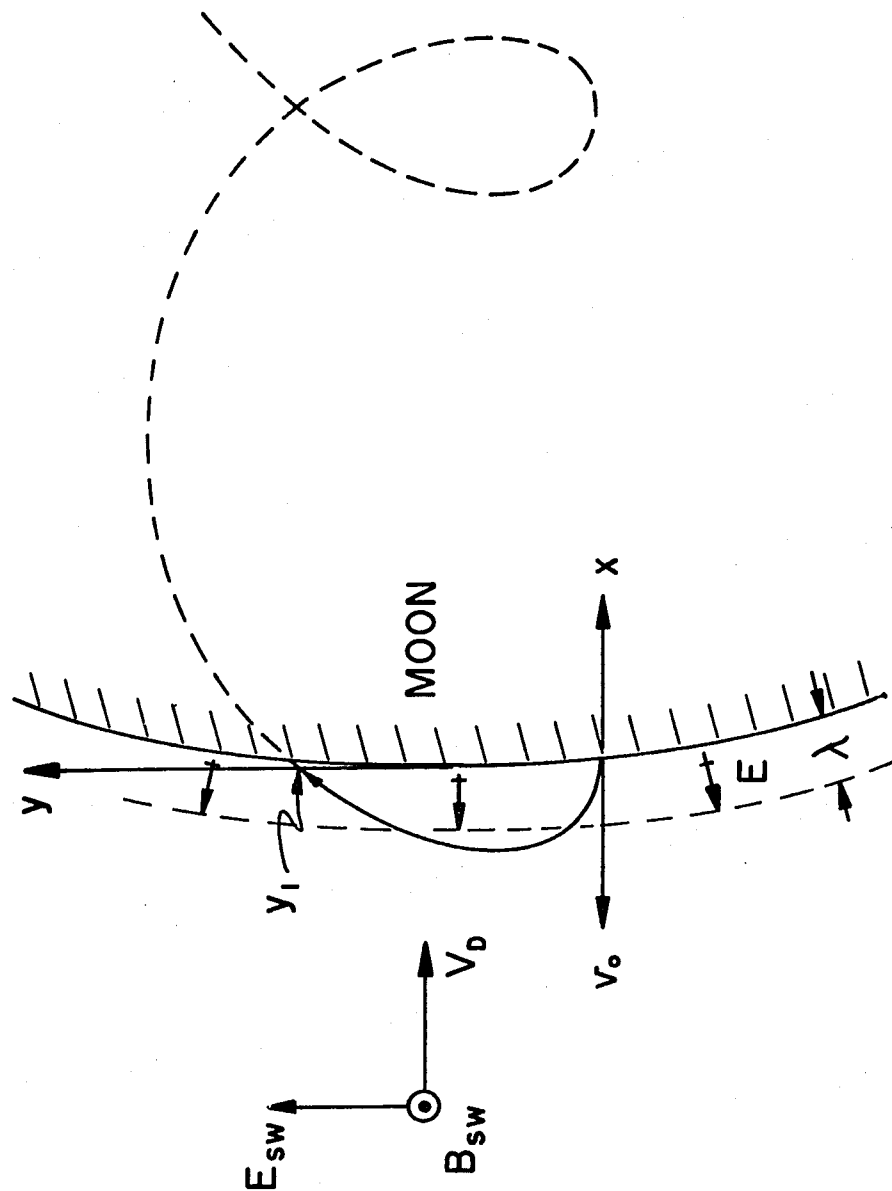
FIGURE 10

perpendicular to $\bar{V}_{sw}$, then the ion would be assumed to be ejected in the anti-solar wind direction .) As we shall soon see, most ions are formed outside of the sheath; thus we will not develop this injected ion case in detail. The orbit of a particle initially injected upstream is a pro-late cycloid. The coordinates of the particle as a function of time are

$$x = \frac{-(V_D + v_o)}{\omega_c} \sin \omega_c t + V_{sw} t \qquad (4\text{-}14)$$

and

$$y = \frac{(V_D + v_o)}{\omega_c} (1 - \cos \omega_c t) \qquad (4\text{-}15)$$

where ω_c is the angular gyro frequency and the gyro radius appropriate to the above initial conditions is given by $a_c = (V_D + v_o)/\omega_c$. The ion re-crosses the $x = 0$ plane at $t = t_1$ where

$$\frac{(V_D + v_o)}{\omega_c} \sin (\omega_c t_1) + \frac{V_D}{\omega_c} (\omega_c t_1) = 0 \qquad (4\text{-}16)$$

The y- displacement, y_1, at $t = t_1$ is determined from equations (4-15) and 4-16).

Ions Formed Outside the Plasma Sheet

Most of the lunar ionosphere is formed outside of the plasma sheath since the neutral atmosphere scale height is much larger than the thickness of the plasma sheath. The scale height for a neutral species is approximately given by

$$h = \frac{kT}{mg} \tag{4-17}$$

where k is the Boltzmann constant, T and m are the species temperature and mass, and g is the lunar gravitational constant. Typical scale heights are of the order of 25 to 150 kilometers and are large compared to estimated Debye lengths (about 10 meters in the solar wind) at the lunar surface, as shown in Chapter III.

An ion formed outside the sheath starts its orbit essentially at rest and is accelerated in the y- direction by the interplanetary electric field. If we let $x = y = 0$ be at the point where the ion is formed, then its position as a function of time is an ordinary cycloid and is given by

$$x = \frac{-V_D}{\omega_c} \sin \omega_c t + V_{sw} t \tag{4-18}$$

and

$$y = \frac{V_D}{\omega_c} \ (1 - \cos \ \omega_c t) \qquad (4\text{-}19)$$

The electrostatic force exceeds the gravitational force by a factor $eE_{sw}/mg_{moon} \approx 5 \times 10^3$, thus gravity becomes a negligible perturbation. The initial motion of an ion is along $\bar{E}_{sw}$ and, as the ion gains energy, the magnetic force curves the ion in the direction of the solar wind flow with a resulting cycloidal orbit. The height of the cycloid is $2 \ a_c$, where $a_c = V_D/\omega_c$ is the correct cyclotron radius to use in the lunar rest frame. For Ar^{40} in a magnetic field of $B_{sw} = 10$ gamma, a_c is 17,820 km, or about ten lunar radii. Thus, for heavy ions like argon, the cycloidal dimensions are much greater than the lunar radius; the ion's trajectory from formation to impact is the initial part of a cycloid, and the motion is nearly parallel to $\bar{E}_{sw}$. Consequently, most of the flux of lunar ions to the surface is in a direction perpendicular to the solar wind flow. In general, ions formed in the lower sunlit atmosphere are driven up (with respect to $\bar{E}_{sw}$) into the moon while ions formed at the equator and in the upper hemisphere escape. Depending

upon the direction of $\bar{B}_{sw}$, the interplanetary electric field
is generally upward or downward out of the solar ecliptic
plane; and, when the direction of $\bar{B}_{sw}$ reverses several times
during each solar rotation, the direction of $\bar{E}_{sw}$ and the ion
flux also reverse. While the ion flux is generally in the
sunlit portion of the upper or lower hemisphere, this distri-
bution will be smeared some due to fluctuations of $\bar{B}_{sw}$ out
of the ecliptic plane.

B.   Trajectories Intersecting the Moon

The energy of the ion at impact is just the energy
gain along the interplanetary electric field

$$\mathscr{E} = eE_{sw}\, y_i \qquad\qquad (4\text{-}20)$$

where e is the ion charge (we assume single ionization) and
y_i is the y-coordinate at impact. The coordinates and other
parameters of impact are given by the simultaneous solution
of the equations for the cycloidal orbit and the circular
cross section of the moon. For an ion originating a distance
h from the surface and in the moon-midnight plane, the ion
impacts the moon at a y-coordinate determined from

$$\left[a'_c \arccos \left(1 - \frac{y}{a'_c} \right) \mp a'_c \sqrt{1 - \left(1 - \frac{y}{a'_c} \right)^2} - R \cos \lambda_1 \right]^2$$

$$+ \left[y + R \sin \lambda_1 \right]^2 = R^2_m \qquad (4\text{-}21)$$

where R_m is the lunar radius, $R = R_m + h$, $a'_c = V_D/\omega_c$ and

the minus sign in front of the radical is chosen for the

first half of the cycloidal orbit.

As shown in Figure 11, an ion formed at some height,

say one scale height, above the surface and at an "electric"

latitude λ_1 impacts at λ_2 with an impact angle a and an

energy $\mathscr{E}$. (The latitude is chosen with respect to the

direction to $\bar{E}_{sw}$; thus if $\bar{E}_{sw}$ reverses direction, the $\lambda =$

$+ 90°$ and $- 90°$ poles also exchange positions with respect

to the fixed selenographic coordinates.) There is a

critical starting latitude for which an ion just grazes the

surface, and ions formed at latitudes nearer the equator,

and in the upper hemisphere, escape. The sketch of Figure

11 illustrates, with some exaggeration, the trajectories of

three ions of quite different mass. Actually, hydrogen is

not gravitationally bound, scale height does not have a

meaning in the usual sense, and most hydrogen ions are

Figure 11:   Sketch of orbits of ions formed outside

the plasma sheath and at a distance h

from the surface.   (Actually krypton

and oxygen have different scale heights

and hydrogen is not bound.)   The sketch

illustrates that ions heavier than hydro-

gen will strike primarily the hemisphere

into which they are driven by the inter-

planetary electric field; when the

polarities of $\bar{B}_{sw}$ and $\bar{E}_{sw}$ reverse, the

other hemisphere is struck.   The trajec-

tories are shown in a plane passing through

the center of the moon and containing

the drift velocity $\bar{V}_{D}$ as well as $\bar{E}_{sw}$.
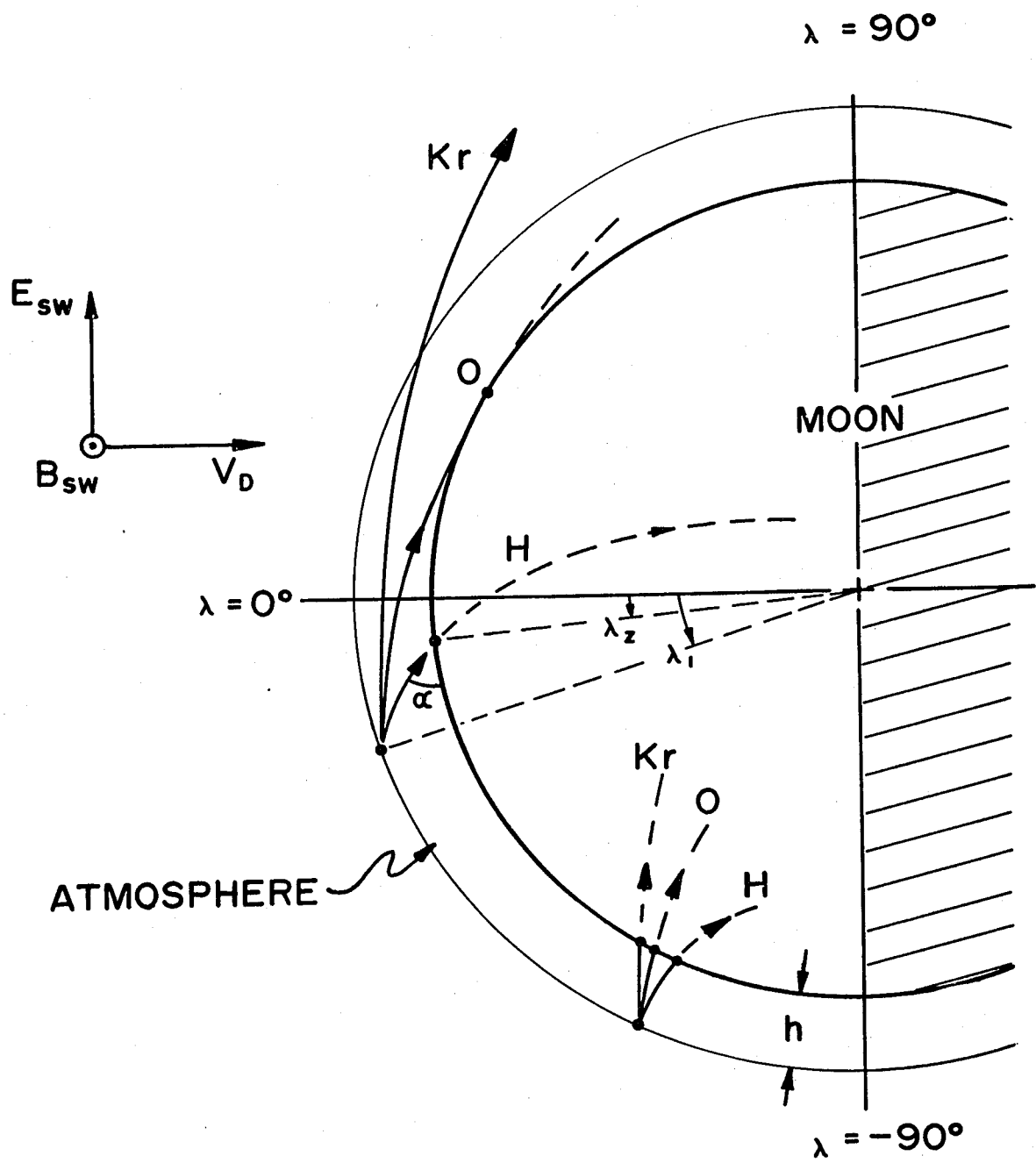
FIGURE II

formed at much greater heights than for bound species.

C. Energies of Impacting Ions

Tables 6a and 6b show the impact angle, latitude, and
energy for ions formed at altitude h and latitude λ_1.
The average interplanetary magnetic field varies considerably
about 6 γ (gamma) and is oriented at about 45 degrees to
the flow direction. The characteristic features of the
trajectory can be obtained calculating the trajectory in a
plane containing $\bar{V}_D$ and perpendicular to $\bar{B}_{sw}$, the orbit
parameters are calculated numerically for both $B_{sw} = 5 \gamma$
and 10 γ (which give $E_{sw} = 2$ volts km^{-1} and 4 volts km^{-1}
respectively) where 5 γ is probably closer to the actual
average conditions. For simplicity, the values taken for
V_D in these calculations are approximately equal to experi-
mental values for the mean solar wind speed. Examination
of the impact coordinates shows relatively small differences
for the two cases; however the impact energies for the 10 γ
case are about twice those for the 5 γ case since the
energies depend on E_{sw} as shown in equation (4-20). Physi-
cally we can see that since only the initial part of the
cycloid is involved, the ion trajectory is primarily along

TABLE 6a: Orbit parameters for ions starting at rest one scale height from the lunar surface. Solar wind parameters are V_D = 400 km/sec and B_{sw} = 5 gamma; calculations are for the lunar noon-midnight meridian plane.

λ_1 (deg)	λ_2 (deg)	a (deg)	$\mathscr{E}$ gain (eV)
	Neon - 20 (h = 100 km)		
-90	-90.1	93.3	200
-60	-58.3	61.6	228
-30	-24.5	28.9	397
-14.9	0	6.8	951
-13.7	8.2	0	1363
	Argon - 40 (h = 50 km)		
-90	-90.0	91.6	100
-60	-59.1	60.8	115
-30	-27.2	29.4	199
-11.1	0	4.2	687
-10.4	4.7	0	935
	Krypton - 84 (h = 23.8 km)		
-90	-90.0	90.8	48
-60	-59.6	60.4	55
-30	-28.7	29.7	95
- 8.0	0	2.4	487
- 7.6	2.6	0	627

TABLE 6b: Orbit parameters for ions starting at rest one scale height from the lunar surface. Solar wind conditions are V_D = 400 km/sec and B_{SW} = 10 gamma; calculations are for the noon-midnight meridian plane.

λ_1 (deg)	λ_2 (deg)	a (deg)	$\mathscr{E}$ gain (eV)
Neon - 20 (h = 100 km)			
-90	-90.2	94.6	400
-60	-58.3	63.1	451
-30	-24.8	30.9	763
-13.7	0	9.3	1747
-11.3	11.7	0	2857
Argon - 40 (h = 50 km)			
-90	-90.0	92.3	200
-60	-59.1	61.5	228
-30	-27.3	30.4	392
-10.3	0	5.6	1286
- 9.1	6.8	0	1960
Krypton - 84 (h = 23.8 km)			
-90	-90.0	91.1	96
-60	-59.6	60.7	110
-30	-28.7	30.2	189
- 7.5	0	3.4	912
- 6.9	3.7	0	1289

$\bar{E}_{sw}$ and thus variations in the magnitude of $\bar{B}_{sw}$ do not greatly alter the impact coordinates; however, variations in the magnitude of $\bar{B}_{sw}$ do proportionally change the magnitude of $\bar{E}_{sw}$ and thus the value of $\mathcal{E}$. The impact energies are higher near the equator than at the poles so atmospheric ions should be more easily trapped near the equator. The impact energy is also approximately inversely proportional to the mass of the ion. Figure 12 shows a plot of some initial and impact latitudes for Ar^{40} in a 10 gamma field.

D.   Trajectories to the Dark Side

An extremely interesting consequence of the trajectories is that some ions formed in the sunlit atmosphere can execute trajectories which carry them into the dark side. We show two examples here: ions formed near the surface which impact past the terminator, and the case of hydrogen which can travel well into the dark side.

Table 7 (B = 10 gamma) shows the impact parameters for oxygen (h = 131 km) and for comparison, hydrogen ions formed at the same height. The oxygen barely impacts on the dark side when λ_1 is -90°. On the other hand, hydrogen impacts

Figure 12: Plot of the impact energy as a

function of impact latitude for

argon-40 ions starting at one and

two scale heights above the lunar

surface.
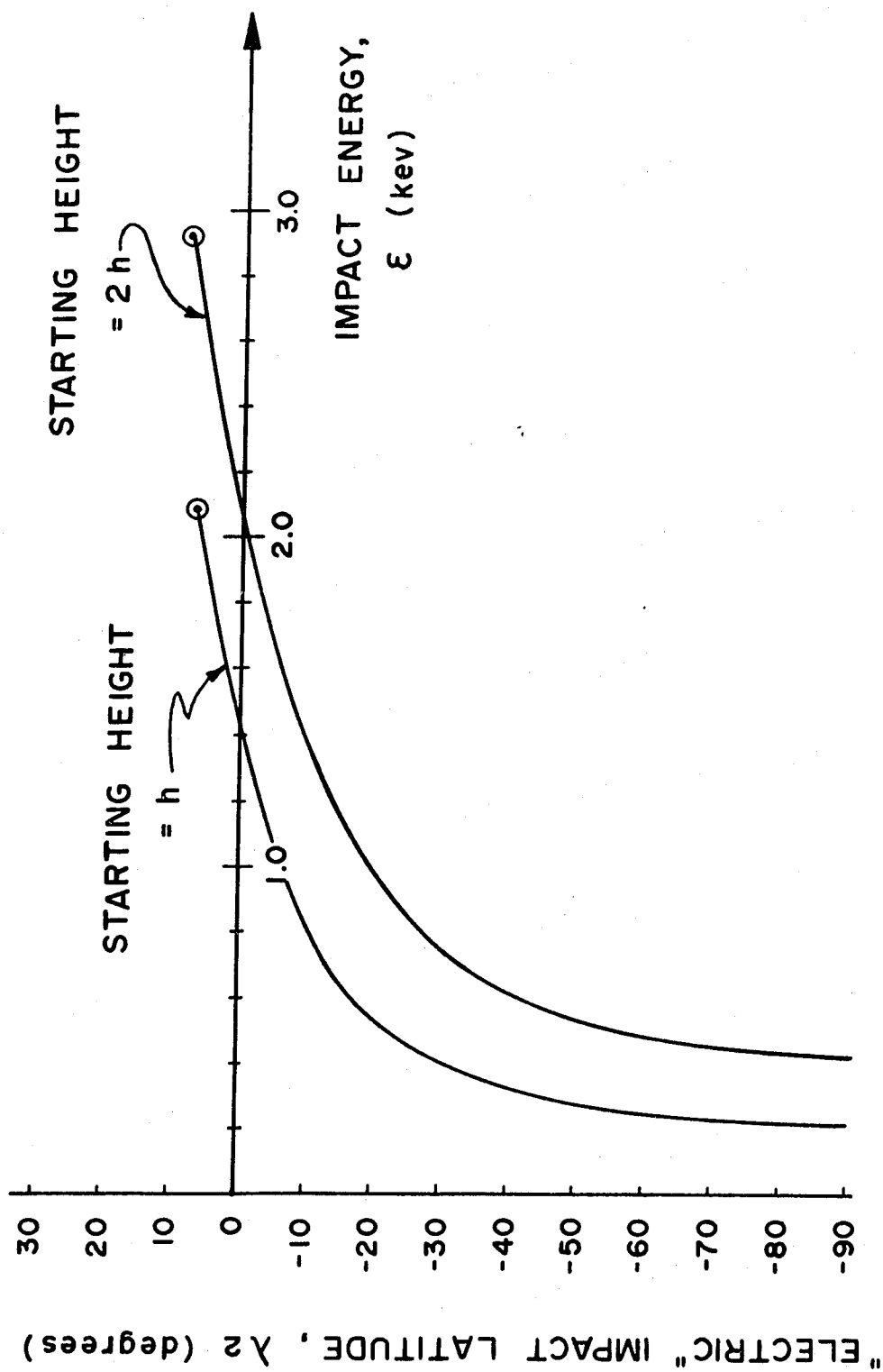
FIGURE 12

TABLE 7:   Some Representative Orbit Parameters and Energy
Gains for Ions Starting at Rest One Scale Height
from the Lunar Surface.   (Hydrogen is Not Bound
so h = 131 km Is Chosen for Comparison to Oxygen.)

λ_1 (deg)	λ_2 (deg)	a (deg)	y (km)	$\mathscr{E}$ gain (ev)
		Hydrogen (Choose h = 131 km)		
-90	-91.1	114	131	570
-60	-58.8	81	132	570
-30	-25.9	52	176	760
0	11.6	27	350	1510
30	112.0	8	678	2920
36.5	140.2	37	0	0
		Oxygen (h = 131 km)		
-90	-90.3	96	131	570
-60	-57.8	64	147	630
-30	-23.3	31	248	1070
-12.4	14.0	0	823	3540

on the dark side from both positive and negative starting latitudes. Figure 13 shows the starting and impact latitudes for oxygen and hydrogen (starting at a height of 131 km) as a function of the impact angle a .

For comparison, Figure 14 shows the trajectory (B = 5 gamma) of hydrogen ions formed at a height of one lunar radius. Since the hydrogen is gravitationally escaping, there will be a significant number of ions formed at these high altitudes. The drawing, to scale, is in the plane containing $\bar{V}_D$ (the noon-midnight meridian when $\bar{B}_{sw}$ is perpendicular to $\bar{V}_{sw}$). The midnight meridan corresponds to a time seven days past sunset. If the trajectories for the case $\bar{B}_{sw}$ perpendiculat to $\bar{V}_{sw}$, are drawn on a plane which intersects the dark side equator only three days past sunset, then it is possible for these hydrogen ions to reach the dark side equator. Of course the actual trajectory plane depends on the instantaneous orientation of $\bar{B}_{sw}$.

E. Predicted Correlations with the Interplanetary

Magnetic Field

In the geometry of the trajectories discussed so far, the plane of the trajectory is determined by the direction

Figure 13: Plot of the initial and final latitudes

for an ion trajectory versus the angle,

a, with which that trajectory impacts

the moon (See Figure 2). The calcula-

tions are for ions formed 131 km (the

scale height of oxygen) from the lunar

surface. For example, a hydrogen ion

formed at $+10^{\circ}$ latitude will strike the

surface at $+28^{\circ}$ latitude with an impact

angle of 20°.

Figure 14: Trajectories, to scale, of hydrogen ions

starting about one lunar radius above

the lunar surface. Ions starting along

a part of the double lines will all im-

pact at the same point on the surface.
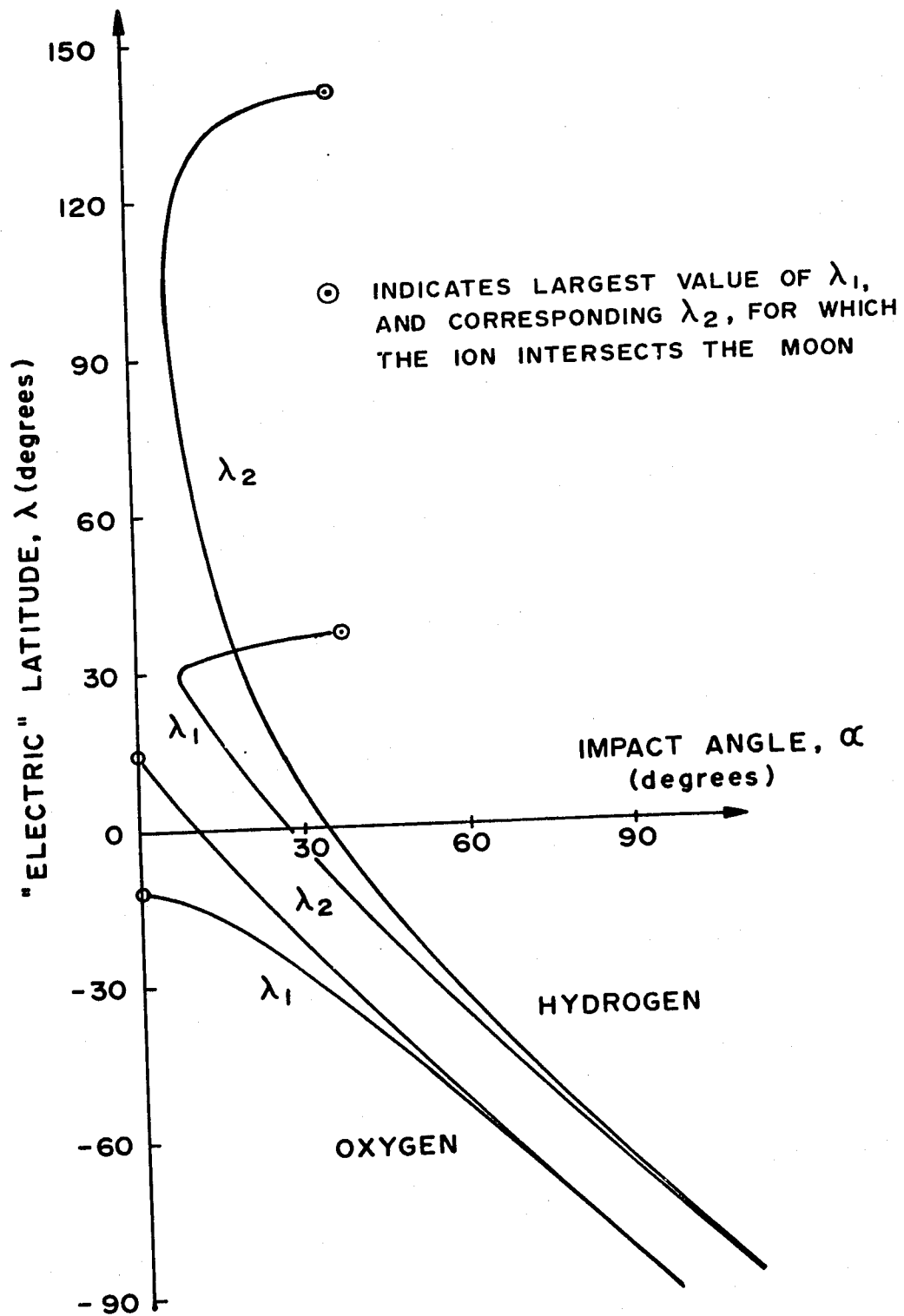
FIGURE 13
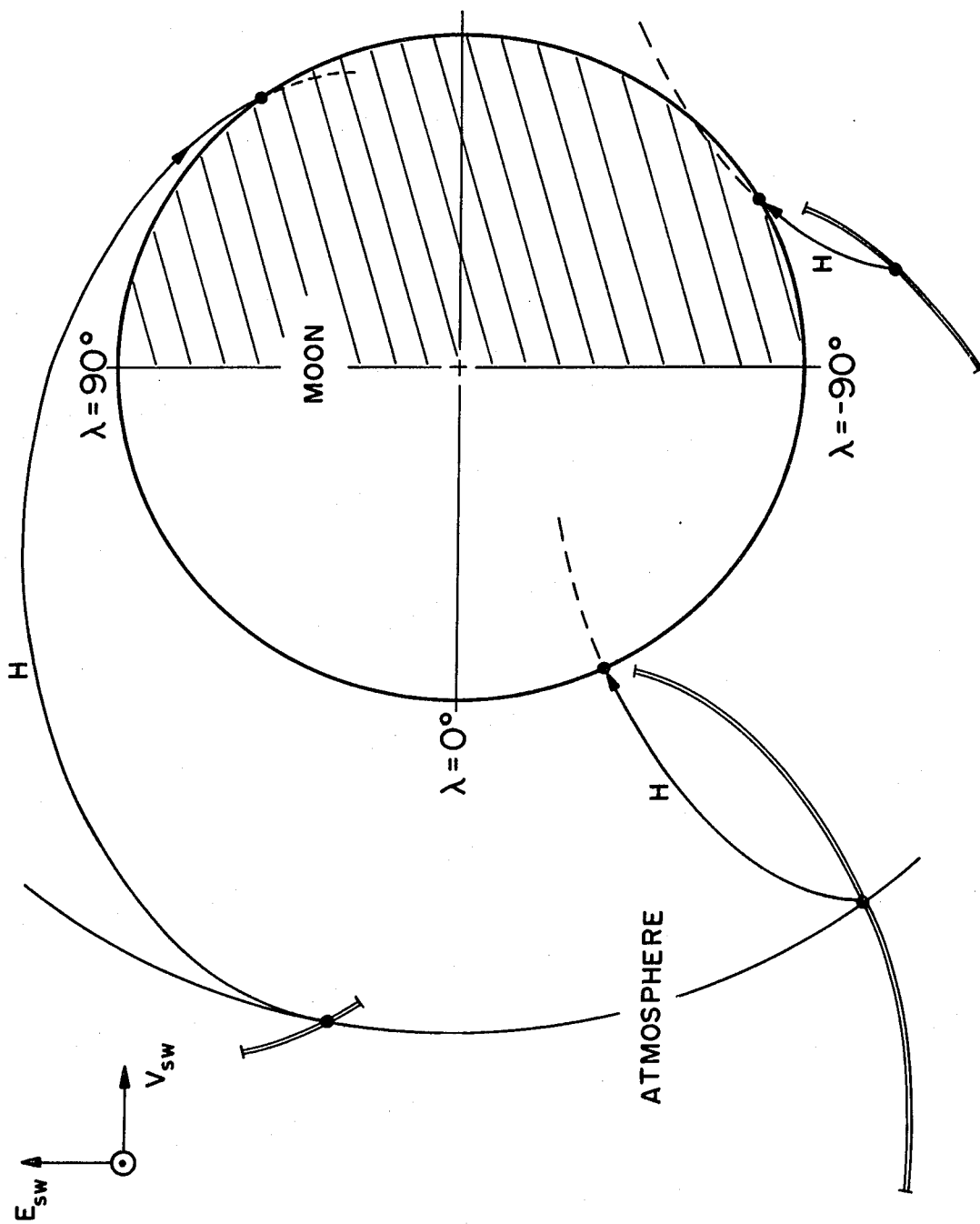
FIGURE 14

of $\bar{E}_{sw}$ which in turn is orthogonal to $\bar{B}_{sw}$. While $\bar{B}_{sw}$ lies

on the average in the vicinity of the plane of the ecliptic,

it actually fluctuates widely in time and may even be at

right angles to the ecliptic. In this latter case, the

electric field lies in the ecliptic as does the plane of the

ion trajectory. Thus although the ion flux is generally in

the sunlit portion of the upper or lower hemisphere, this

distribution is smeared considerably owing to fluctuations

of $\bar{B}_{sw}$. Figure 15 contains data of Burlaga and Ness (1968)

showing the distribution of magnetic field directions in

the plane of, and perpendicular to, the ecliptic; also

shown is an example of one magnetic field and corresponding

electric field orientation projected on the moon as seen

looking along the solar wind flow direction.

Clearly the considerable fluctuations of $\bar{B}_{sw}$ out of

the ecliptic plane will rotate the planes of lunar

trajectories. While the interplanetary electric field may

be the principal energy source of the ions, the lunar sur-

face electric and magnetic fields could play important

roles in changing an ion's direction and modifying its

energy as it approaches the surface. The Suprathermal Ion

Detector (Freeman et al., 1971) is orientated so that it

Figure 15: Directional histograms of interplane-

tary magnetic fields parallel and

perpendicular to the ecliptic as mea-

sured by Pioneers 6 and 7 (Burlaga and

Ness, 1968). Also shown is an example

of a particular orientation of $\bar{B}_{sw}$, and

corresponding $\ddot{E}_{sw}$, projected onto the

moon.

Figure 16: Deflection of incoming atmospheric ions

by a uniform lunar surface magnetic

field.

NORMAL TO
ECLIPTIC PLANE

$\theta = +90°$

TO
SUN

NEGATIVE   POSITIVE

ECLIPTIC PLANE

ISOTROPIC

NEG
41%

$\bar{B}$

$\phi = 90°$ $\phi = 270°$ $\theta = 0°$

POS
49%

UNIFORM

$\theta = -90°$

$\phi = 180°$

REPRESENTATIVE INTERPLANETARY MAGNETIC FIELD DIRECTIONS
(Burlaga and Ness, 1968)

$\bar{E}$ N

Selenographic
Equator

$\bar{B}$

MOON

"Electric"
Equator

S

"ELECTRIC" COORDINATES – PROJECTED ON MOON
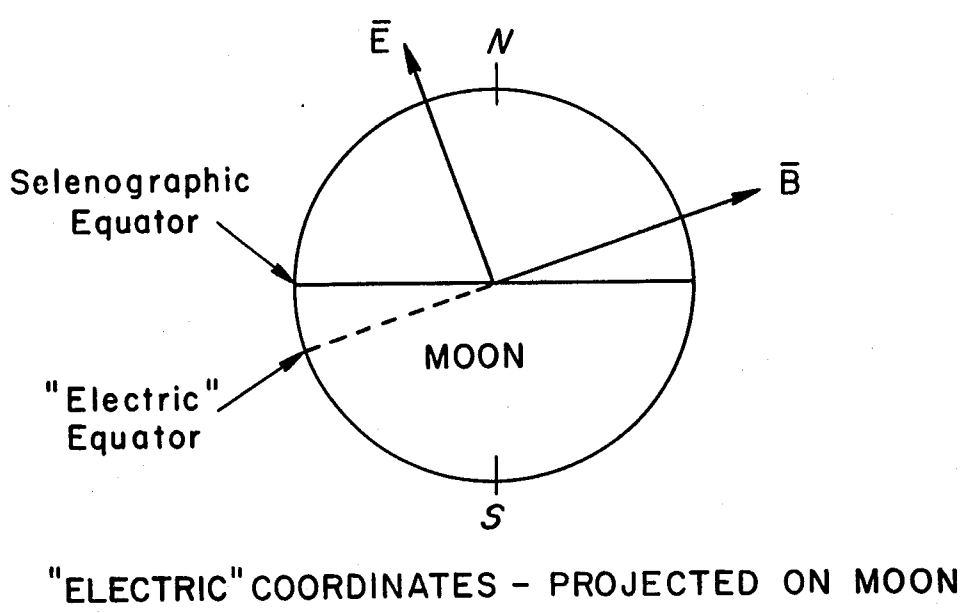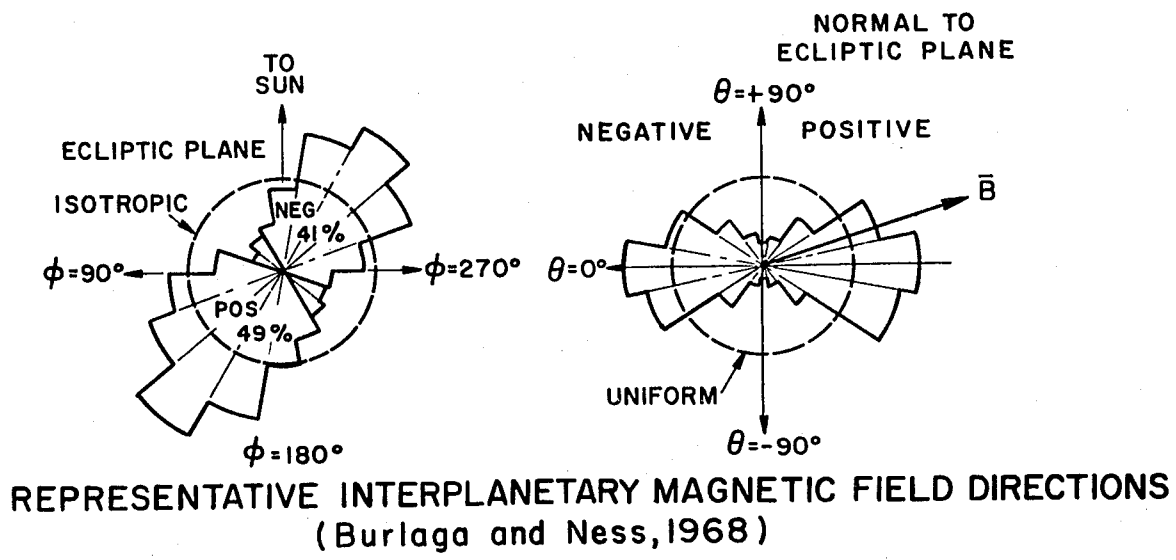
FIGURE 15

ION DEVIATION BY SURFACE MAGNETIC FIELD

	ε =	10 ev	50 ev	100 ev
B = 40γ,	ℓ = 1 km	1°	.5°	.4°
	ℓ = 10 km	11°	5°	4°
B = 100γ,	ℓ = 1 km	3°	1°	.9°
	ℓ = 10 km	30°	13°	9°

FIGURE   16

looks in the ecliptic plane and sees sporadic "clouds" of ions arriving at the lunar surface. The fluctuations in the direction of $\bar{E}_{sw}$, may combine with the surface fields to allow the detection of these bunches of ions. The measured energies of the ions, of tens to hundreds of electron volts, are reasonable for $\bar{E} \times \bar{B}$ acceleration. The Solar Wind Spectrometer (Snyder et al., 1971) looks both vertical and horizontal to the local surface and the majority of the ion flux detected after the Apollo 12 S-IVB impact event was directed horizontal to the local surface and from north to northeast. That is, the trajectories lie in a plane generally perpendicular to the ecliptic plane and which is qualitatively in agreement with the predictions of Manka and Michel (1970) for the case when $\bar{B}_{sw}$ is generally in the ecliptic plane.

F.   Effects of Surface Electric and Magnetic Fields

The lunar surface electric field has been discussed in detail in Chapter III. From the results presented there, the general situation is that surface potentials will not have extremely large effects over most of the sunlit hemisphere, though at the terminator and into the dark side, the

expected negative potentials could change the ion energy
and also deviate the ion's trajectory somewhat. Further
into the dark side the possibly large negative potentials
could have significant effects. For example, hydrogen orbit-
ing over the pole and returning to the bottom of its cycloid
(and thus low energy) as it approaches the equator could be
strongly deflected and accelerated toward the lunar surface,
possibly even coming in normal to the surface and thus
being detectable by the SIDE experiments.

The surface magnetic field was also discussed in detail
in Chapter III. For future use in this thesis, Figure 16
shows some representative deflections of incoming ions of
energies 10, 50 and 100 eV. These will be discussed in con-
nection with the specific ion events to be studied.

V.

ATMOSPHERE TRAPPING IN THE LUNAR SURFACE

Return of the first lunar samples from the moon gave some indication that gases other than those from the solar wind are trapped in the lunar surface. The analysis of lunar samples continues to exhibit unexpected compositions in some gaseous elements. One of the most pronounced anomalies is the excess of surface correlated Ar^{40}, compared to solar wind implanted Ar^{36}, which was discussed by several researchers, including Heymann et al. (1970) who proposed a lunar source for the Ar^{40}, being produced by K^{40} decay in the moon. In a paper showing that the lunar atmosphere is the likely source of the surface Ar^{40}, Manka and Michel (1970c) suggested that the atmosphere would also be the source of other unexpected surface elements, or unexpected concentrations of elements, including solar wind elements which have been cycled through the atmosphere and reimplanted in a manner characteristic of atmospheric ions. However, the atmospheric contribution to the elements is not as obvious as in the case of Ar^{40}; the nonradiogenic noble gas isotopes are not as readily attributable to lunar

origin as is Ar^{40} and the gases directly implanted from
the solar wind tend to mask those cycled through the atmos-
phere. In addition, gases other than the noble gases can
react chemically when they impact the surface, and are then
difficult to distinguish from trace elements in the sample
minerals.

The lunar atmosphere, moon, and solar wind form a dyn-
amically interacting system and while the lunar atmosphere
is not dense, it can affect critical isotope ratios in the
surface. We discuss here the trapping of atmosphere in the
surface: first the trapping of Ar^{40} in the surface, and
then the more subtle effects on trapped solar wind isotopic
ratios due to cycling through the atmosphere.

A.   The Trapping Function for Ions

For an ion whose trajectory causes it to impact the
moon, whether the ion is firmly implanted in the surface
or is quickly released will depend on both the impact
energy and the trapping probability of $\eta_t(\mathscr{E})$ for the lunar
material. Studies at Berne on ion implantation in aluminum
foils with their associated oxide layer must presently be
assumed to be similar to the characteristics for silicate

grains. The Ar^{40} problem was the first for which trapping
from the lunar atmosphere was calculated and much of the
discussion in this chapter will be for argon. However,
later in the chapter the calculations are extended to other
elements.

The impact latitude and energy for Ar^{40} as a function
of initial latitude is given in Table 6. About two thirds
of the ions are formed less than one scale height above the
surface and their impact energies are correspondingly lower.
The higher impact energies, of the order of one keV, occur
near the "electric" equator which is usually in the vicinity
of the lunar equator.

From the calculations shown, it can be seen that most
of the ions formed in the lower electric hemisphere, about
40% of the total formed, will impact the moon. However,
whether an ion is firmly implanted in a lunar grain or is
quickly released will depend on the impact energy. Bühler
et al. (1966) found that for argon impacting an aluminum
foil, the trapping probability, $\eta_t(\mathcal{E})$, rises linearly to
0.6 at an impact energy, $\mathcal{E}$, of 1 keV and levels off to 1
at 3 keV. We can represent their data as

$$\eta_t(\mathscr{E}) = \begin{cases} 0.6\,\mathscr{E} & \cdot \quad 0 < \mathscr{E} < 1 \text{ keV} \\ 1 - 1.8\,\exp(-1.5\mathscr{E}) & \cdot \quad 1 < \mathscr{E} < 3 \text{ keV} \\ 1 & \cdot \quad \mathscr{E} > 3 \text{ keV} \end{cases} \tag{5-1}$$

where $\mathscr{E}$ is in keV. Figure 17 shows the trapping data of Bühler which is fit with a smooth curve which is well described by equation (5-1) (Manka and Michel, 1970c). In a more recent work, Manka and Michel (1971) represented this data with an equally good fit using the single function

$$\eta_t(\mathscr{E}) = \tanh(0.75\,\mathscr{E}). \tag{5-2}$$

From the energies calculated in Table 6, we can see that it is this initial part of the trapping curve, up to a few keV, that will determine the implantation efficiency of the lunar ionosphere.

More detailed trapping data for helium, neon, and argon was obtained by Meister (1969) and is shown in Figure 18 where the data for the three elements are each fit with tanh functions. The data was fit on a Hewlett-Packard Calculator Plotter and best fits were

Helium: $\eta_t(\mathscr{E}) = 0.90\,\tanh(1.45\,\mathscr{E})$

Neon: $\eta_t(\mathscr{E}) = 0.97\,\tanh(0.7\,\mathscr{E})$

Figure 17:   Trapping probability for argon ions

bombarding aluminum foil as a function

of bombarding energy (from the measure-

ments of Bühler et al., 1966).   The

curve fit to the data is copied from

Bühler's graph, however the appearance

of a hyperbolic tangent fit is similar.

Figure 18:   Trapping data for He, Ne, and Ar from

Meister (1969).   His data has been re-

plotted and fit with tanh functions.

ARGON

(BÜHLER et al., 1966)

ENERGY, ε (kev)

TRAPPING PROBABILITY, η_t (ε)

FIGURE 17

TRAPPING PROBABILITY $\eta_t(\varepsilon)$

ENERGY, ε (kev)

+ HELIUM
△ NEON
□ ARGON

(MEISTER, 1969)
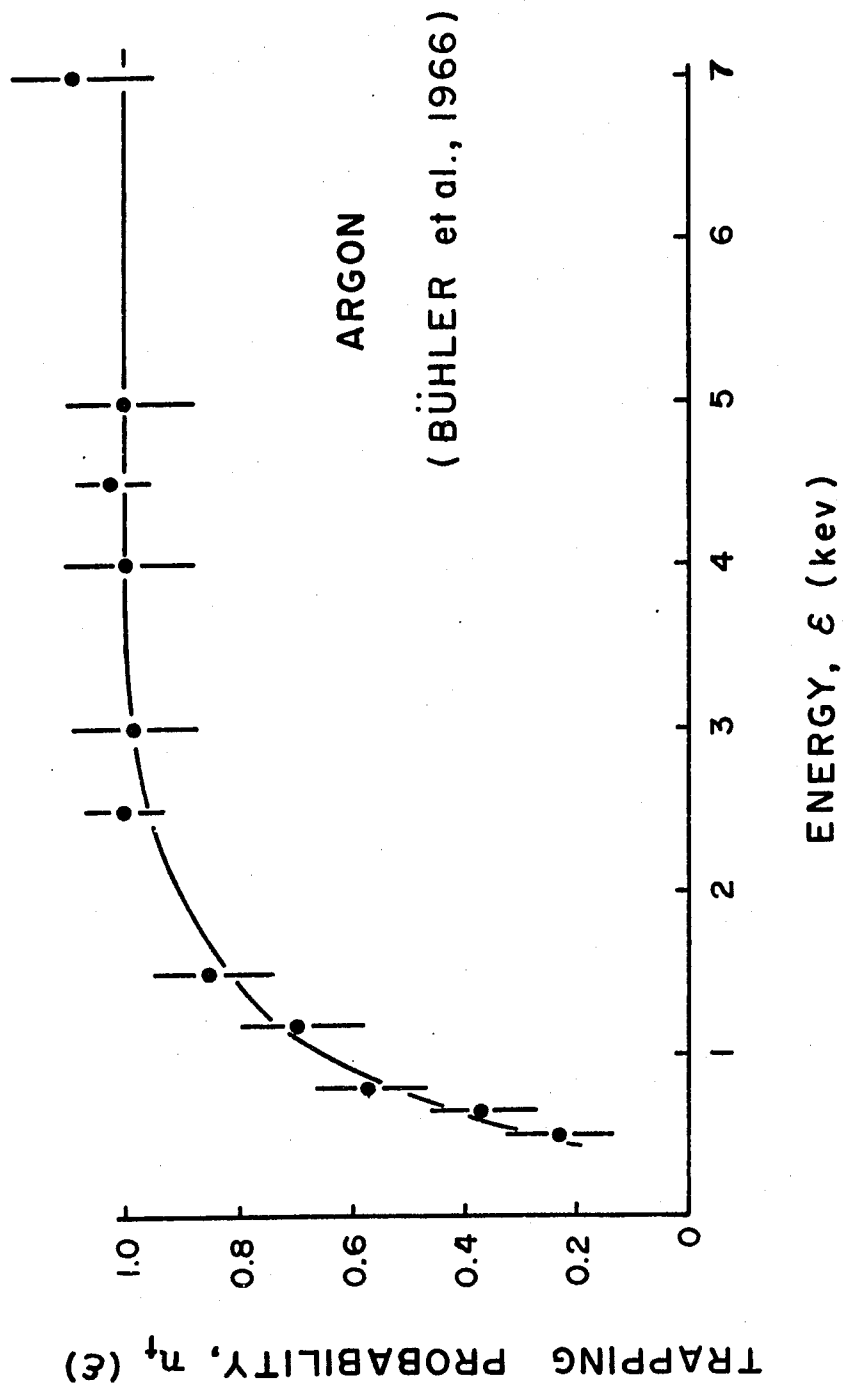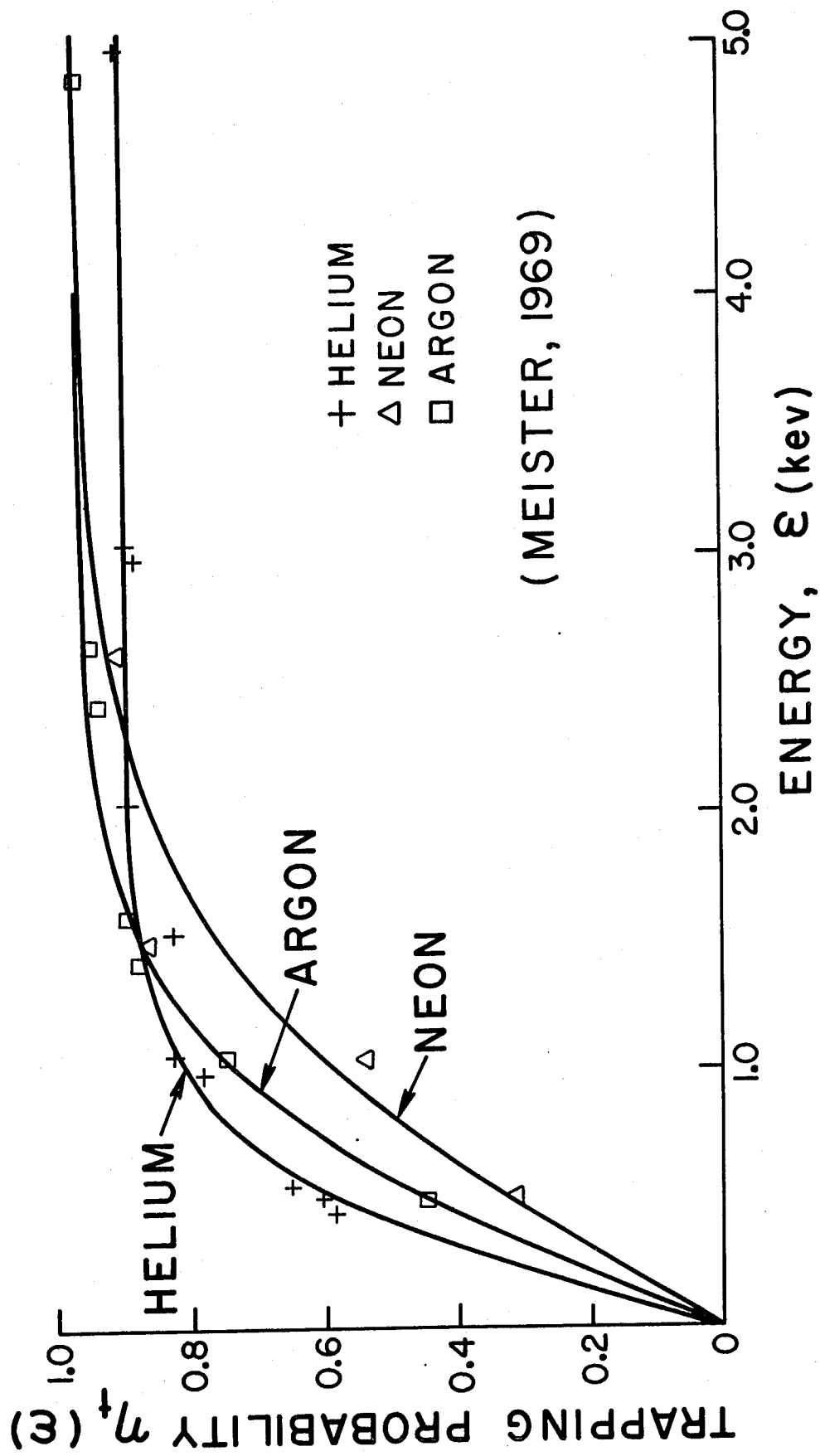
FIGURE 18

Argon: $\eta_t(\mathscr{E}) = 0.97 \tanh (\mathscr{E})$

It should be noted however, that there are uncertainties in the measurements at low energy so that the actual trapping is not known as accurately as these functions would imply.

An important feature of the trapping curve is whether there is a finite, and perhaps not very small, cut-off energy at which the trapping probability goes to zero. Physically this is expected and the data of Kornelsen (1964) for the trapping of noble gas ions in tungsten could indicate such a cut-off as could the detailed measurements of Meister (1969), for the trapping of noble gases in aluminum, who has considered a function containing a cut-off energy to fit the data:

$$\eta_t(\mathscr{E}) = 1 - \frac{\mathscr{E}_o}{\mathscr{E}} , \quad \mathscr{E} > 0 \qquad (5-3)$$

where he would estimate that $\mathscr{E}_o$ is of the order of 150 to 250 eV. Since trapping data is not well defined at such energies, it is hard to say if such a cut-off exists. A cut-off energy can also be incorporated in the tanh fit.

B. **Trapping of Lunar Atmosphere Ar^{40} in the Lunar Surface**

Analysis of the lunar samples from Apollo 11 indicates

anomalous compositions for several elements. In particular,
the isotope Ar^{40} is overabundant compared to Ar^{36} in the
fine grain samples, the ratio being much greater than that
expected in the solar wind composition (D. D. Clayton, per-
sonal communication) and several times greater than could
be accounted for by in-situ decay of K^{40} (Marti et al.,
1970; Funkhauser et al., 1970). Heymann et al. (1970) have
shown that the Ar^{40} is surface correlated and have suggested
a lunar source where the Ar^{40}, produced in the moon by
potassium decay, subsequently diffuses into the lunar atmos-
phere and is then driven back into the surface by collisions
with the solar wind ions; this relationship between the Ar^{40}
data and the lunar atmosphere has been discussed in more
detail by Heymann and Yaniv (1970).

We show here that the source of Ar^{40}, and perhaps
other surface correlated elements, is very likely the lunar
atmosphere; the atmospheric argon is ionized and swept into
the moon by solar wind fields. In addition, we show that
the energy of the lunar ion will be sufficient for implanta-
tion and that the process is reasonably efficient.

The source of Ar^{40} in the lunar atmosphere would be
the decay of potassium in the moon to Ar^{40}, which either

diffuses steadily into the lunar atmosphere or which has

been released by various geological events (volcanism,

surface venting, etc.). Once out of the moon, the neutral

argon is gravitationally bound and forms part of the equili-

brium atmosphere whose density decreases approximately

exponentially with a scale height given by $h = kT/mg$, where

k is the Boltzmann constant, T and m are the species tem-

perature and mass, and g is the lunar gravitational constant.

The Ar^{40} scale height is about 50 km on the sunlit hemis-

phere, and about one-third of the argon is at heights

greater than h. Figure 19 shows a sketch of the trajectories

of Ar^{40} ions formed in the atmosphere. The lunar atmosphere

has been reviewed by Bernstein et al. (1963), who discuss

Ar^{40} in the lunar atmosphere due to decay of K^{40} in the

moon, and by Michel (1964), who calculates atmospheric life-

times against ionization of $\sim 10^7$ sec (0.3 yr.) as compared

to 10^8 years for gravitational escape.

The total number of Ar^{40} atoms which will be trapped

can be found by integrating over that volume of the lunar

atmosphere whose ions impact the lunar surface. In the

integral, the variation in atmospheric density with height,

and the dependence of impact energy on the height and

Figure 19: Sketch of the orbits of Ar^{40} ions formed

a height h above the surface. An ion

formed at λ_1 impacts at λ_2 with an angle

α . The "electric" latitude is chosen

with respect to the direction of the

interplanetary electric field.
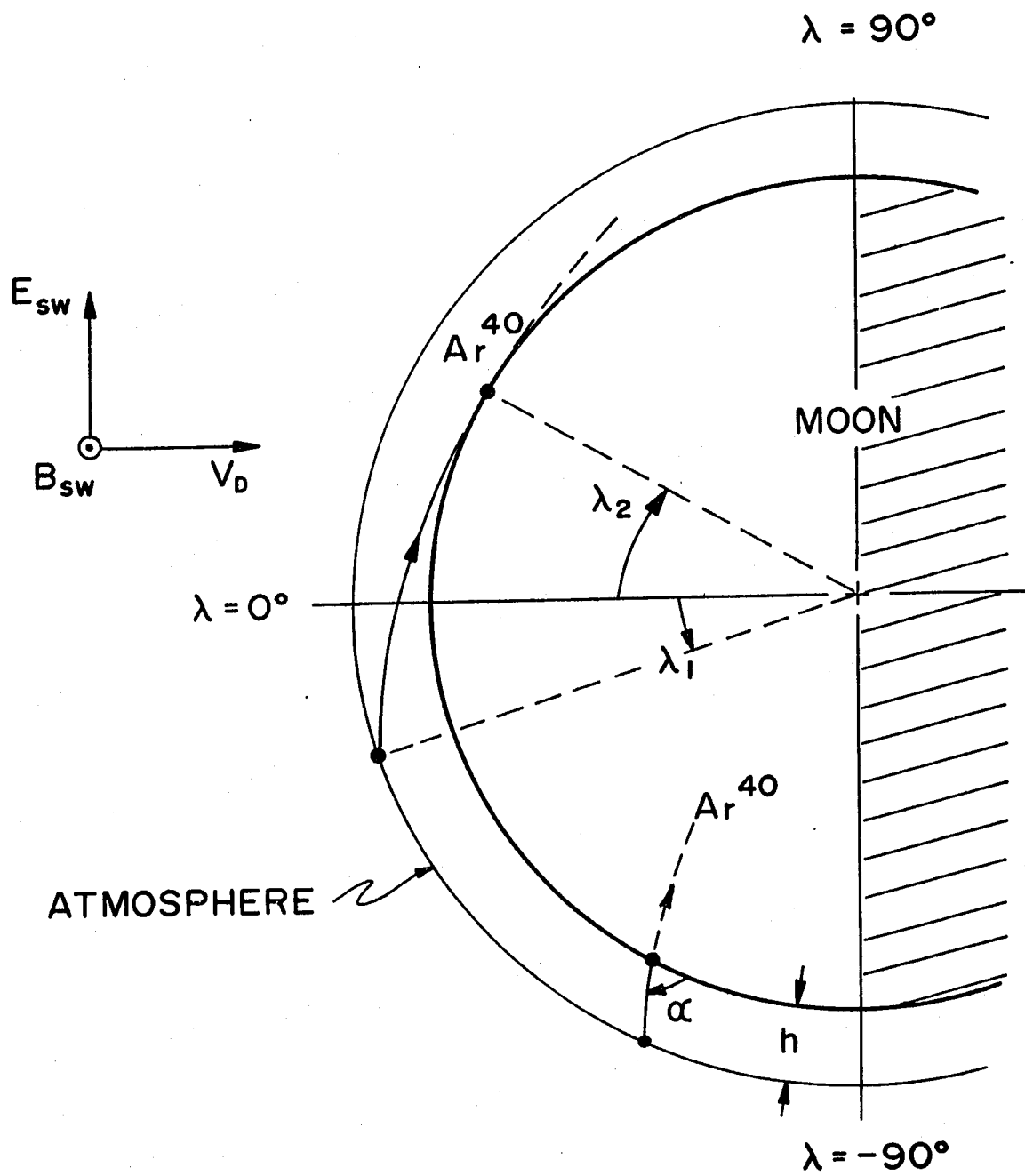
FIGURE 19

latitude at which the ion is formed, are weighted by the trapping coefficient given in (5-1) above.

Trapping Integral:

To estimate the fraction of Ar^{40} in the lunar atmosphere which actually becomes trapped in the lunar surface, we integrate over all portions of the sunlit lunar atmosphere from which ion trajectories impact the lunar surface. We assume that the ions travel straight "up" along $\bar{E}_{sw}$ so that if λ is the latitude, θ is the co-latitude (polar angle), and r is the radial height above the lunar surface, the ion moves a distance y vertically along $\bar{E}_{sw}$ before impacting:

$$y \simeq \frac{r}{\sin \lambda} = \frac{r}{\cos \theta} \qquad (5\text{-}4)$$

and the energy gained is

$$\mathscr{E} = Ey \simeq \left[\frac{E}{\cos \theta} \right] r \qquad (5\text{-}5)$$

where $\mathscr{E}$ has units of kev when E is in $kv \cdot km^{-1}$.

For an atmosphere with an exponential density distribution with height, the number of ions formed is proportional to the number of neutrals and is given by

$$dn_i(r) = n_{io} \, e^{\frac{-r}{h}} \, dr \qquad (5\text{-}6)$$

or as a function of energy and polar angle

$$dn_i(\mathscr{E}) = n_{io} \, e^{-\left[\frac{\cos\theta}{hE}\right]\mathscr{E}} \, \left[\frac{\cos\theta}{E}\right] d\mathscr{E} \qquad (5\text{-}7)$$

so that the differential number trapped is

$$dn_{it}(\mathscr{E},\theta) = n_t(\mathscr{E}) \, dn_i(\mathscr{E},\theta) \qquad (5\text{-}8)$$

and the total number trapped is

$$N_{it} = \int_\phi \int_\theta \int_{\mathscr{E}} dn_{it}(\mathscr{E},\theta) \, R_m^2 \, \sin\theta \, d\theta \, d\phi \qquad (5\text{-}9)$$

The limits on ϕ are $0 \le \phi \le \pi$, and the limits on θ are $0 \le \theta \le \theta_c$ where θ_c is the critical angle above which ions do not impact the moon but are lost. For θ_c we use the angle for which ions starting one scale height above the surface are lost so that for Ar^{40}, $\theta_c = 76^{\circ}$. Three sets of limits are required for the energy since we are using the three-part trapping function in equation (5-1). Thus the number trapped becomes

$$N_{it} = \pi \, n_{io} \, R_m^2 \left[\int_0^{\theta_c} \int_0^{\prime} 0.6 \, \mathscr{E} \, e^{-\left(\frac{\cos\theta}{hE}\right)\mathscr{E}} \left(\frac{\cos\theta}{E}\right) d\mathscr{E} \sin\theta \, d\theta \right.$$

$$+ \int_0^{\theta_c} \int_1^{\mathscr{E}} (1 - 1.8e^{-1.5\mathscr{E}})\ e^{-(\frac{\cos\theta}{hE})\mathscr{E}} (\frac{\cos\theta}{E})\ \sin\theta\ d\theta\ d\mathscr{E}$$

$$+ \int_0^{\theta_c} \int_{\mathscr{E}}^{\infty} e^{-(\frac{\cos\theta}{hE})\mathscr{E}} (\frac{\cos\theta}{E})\ \sin\theta\ d\theta\ d\mathscr{E} \Bigg]$$

$$= \pi\, n_{io} R_m^2\, h\ (\ 0.172\ ).$$

(5-10)

With the approximations used here, the total number of ions formed in the sunlit atmosphere is

$$N_i = 2\,\pi\, R_m^2 (n_{io} h) \tag{5-11}$$

so that

$$\frac{N_{it}}{N_i} = \frac{0.172}{2} = 0.086 \tag{5-12}$$

or the fraction trapped is about 8.6%.

It should be noted that this number is approximate since there are a number of approximations and assumptions about physical parameters which are involved. For example, possible saturation effects are not included in the calculation. It should again be noted that the impact energies and resulting trapping coefficient are calculated for $B_{sw} = 10$ gamma. If 5 gamma were used instead (which may be closer to the average value), then the impact energies would be about half of those tabulated, and a smaller fraction of the ions would

be trapped.

From Table 6 we see that Ar^{40} impact energies (~ 1 kev) are less than the solar wind Ar^{36} energy (~ 36 kev), so we would expect that the Ar^{40} is not initially implanted as deeply. This may be the reason that step-wise heating of lunar samples show larger Ar^{40}/Ar^{36} ratios at low temperatures (Pepin et al., 1970; D. D. Bogard, personal communication). If most of this Ar^{40} is from the lunar atmosphere and not contamination from the sample processing, then it implies that the Ar^{40} flux from the lunar atmosphere exceeds the Ar^{36} flux from the solar wind.

A brief summary of the Ar^{40} and Ar^{36} data, and the widely-varying conclusions drawn by different authors, is appropriate. As already mentioned, the Ar^{40} is surface-corrolated in lunar grains, implying an external source; also it is doubtful that there is sufficient K^{40} in the grains for in-situ decay to provide the observed Ar^{40}. There is some variation in the Ar^{40}/Ar^{36} ratio from samples at a given Apollo site, and the average ratio varies from site to site. The average ratios are: 1.3 for the oldest site, Apollo 14 (3.9 b.y.), 1.1 for Apollo 11 (3.7 b.y.), and 0.35 for Apollo 12 (3.3 b.y.) (Heymann et al., 1972).

The gas release pattern during stepwise heating of samples has been studied by Hohenberg et al. (1970) and Pepin et al. (1970). Typically it was found that the peak gas release for both Ar^{40} and Ar^{36} occurs at about 800° C, though at lower temperatures the amount of Ar^{40} generally exceeds the amount of Ar^{36}; the Ar^{40}/Ar^{36} ratio is typically about 15 at 300° C and drops to about unity at 800°C. The gas release pattern as a function of depth was studied, by Marti and Lugmair (1971), in the double core 12025-12028. They found that the solar wind gases He^4, Ne^{20}, Ar^{36}, and Kr^{86} all had a correlated concentration with depth; however, Ar^{40} was not correlated with the other gases.

Recently Baur et al. (1972) have studied the temperature release patterns of Ar^{40} and Ar^{36}, with results similar to these quoted above, and they conclude that because of this release pattern that the Ar^{40} is not implanted from the lunar atmosphere as proposed by Manka and Michel (1970c). Their principal objection to atmospheric implantation is that both Ar^{40} and Ar^{36} have peak releases at the same temperature, but presumably were implanted at very different energies. They propose as alternative explanations either a solar Ar^{40}/Ar^{36} ratio around unity, or a surface

correlated K^{40}. However, this argument is weak since stellar abundance calculations, which now give consistant results, predict the solar abundance of Ar^{40} to be several orders of magnitude lower that that of Ar^{36} and likewise the solar K^{40} abundance is predicted to be very low. Also, since the depth to which solar wind gases are found, 0.2 to 1.0 microns (Eberhardt et al., 19701 Kristen et al. 1971), were greater than the expected implantation depth, it is possible that significant diffusion has taken place in the grain and that the differences in the original dis- tribution have been removed. Finally, a solar source for Ar^{40} is unlikely since Ar^{40} does not correlate with solar wind gases in the core sample. Perhaps more significant is the trend toward lower Ar^{40}/Ar^{36} ratios found at younger sites. Such a trend could be at least partially explained by the decay of lunar K^{40} (halflife of 1.3 b.y.) so that the amount of parent material, and thus atmospheric Ar^{40} is constantly decreasing. The measurement of two samples (Heymann et al., 1972) with no trapped Ar^{40} is not, in our opinion, sufficient evidence to indicate the absence of Ar^{40} in the present lunar atmosphere, since the samples are also low in solar wind content and thus may have been

shielded from implantation. However, the question is raised that the present concentration of Ar^{40} on the atmosphere may be reduced compared to 3 to 4 b.y. ago.

The concentration of gases in the early lunar atmosphere was no doubt influenced by the lunar thermal history. However, it should also be noted that if the lunar atmosphere were to become only a few orders of magnitude denser than it is now, then a shock would be formed in the solar wind and our acceleration mechanism would no longer be operative in that portion of the atmosphere not penetrated by solar wind (e.g. Cloutier et al., 1969).

In principle, the Ar^{40}/Ar^{36} ratio should vary with the orientation of an object's surface; Ar^{36} should be more common in surfaces facing the solar wind while Ar^{40} should be more common in surfaces facing normal to the ecliptic plane. However, the Ar^{40} distribution will be smeared some by fluctuation in $\bar{B}_{sw}$ (which rotates $\bar{E}_{sw}$), movement of the object, dust transport, etc.

Careful analysis of the Ar^{40}/Ar^{36} ratio may clarify whether the Ar^{40} was deposited in large quantities in the past or continuously to the present. It is possible that both the Ar^{40} and Ar^{36} fluxes could be used to estimate the

length of time a rock fragment has been on the surface and
the orientations it has had. Possibly the analysis of re-
turned segments of Surveyor or LM will determine the present
rate of Ar^{40} deposition and will show the expected variation
with orientation in the Ar^{40}/Ar^{36} ratio.

C. <u>Fractionation of Solar Wind Elements in the Lunar</u>
<u>Atmosphere</u>

As mentioned earlier, it is likely that noble gases
implanted by the solar wind are also being cycled through
the lunar atmosphere, with the possibility that some isotope
ratios are being altered by gases from the lunar interior.
There is also the possibility of some mass fractionation in
the solar wind isotopes which are retrapped from the atmos-
phere. A sketch of the gas release pattern from lunar
samples is shown in Figure 20. The initial isotope ratios
observed in stepwise heating of samples typically shows an
enhancement in the lighter isotope compared with the ratio
observed at higher temperatures (<u>Pepin et al.</u>, 1970);
<u>Hohenberg et al.</u>, 1970). <u>Nyquist and Pepin</u> (1971) indicated
at the Apollo 12 Conference that later data shows the same
enhancement found for Apollo 11 samples. One possible ex-

Figure 20:   Sketch of the trapped gas release during

the stepwise heating of lunar samples.
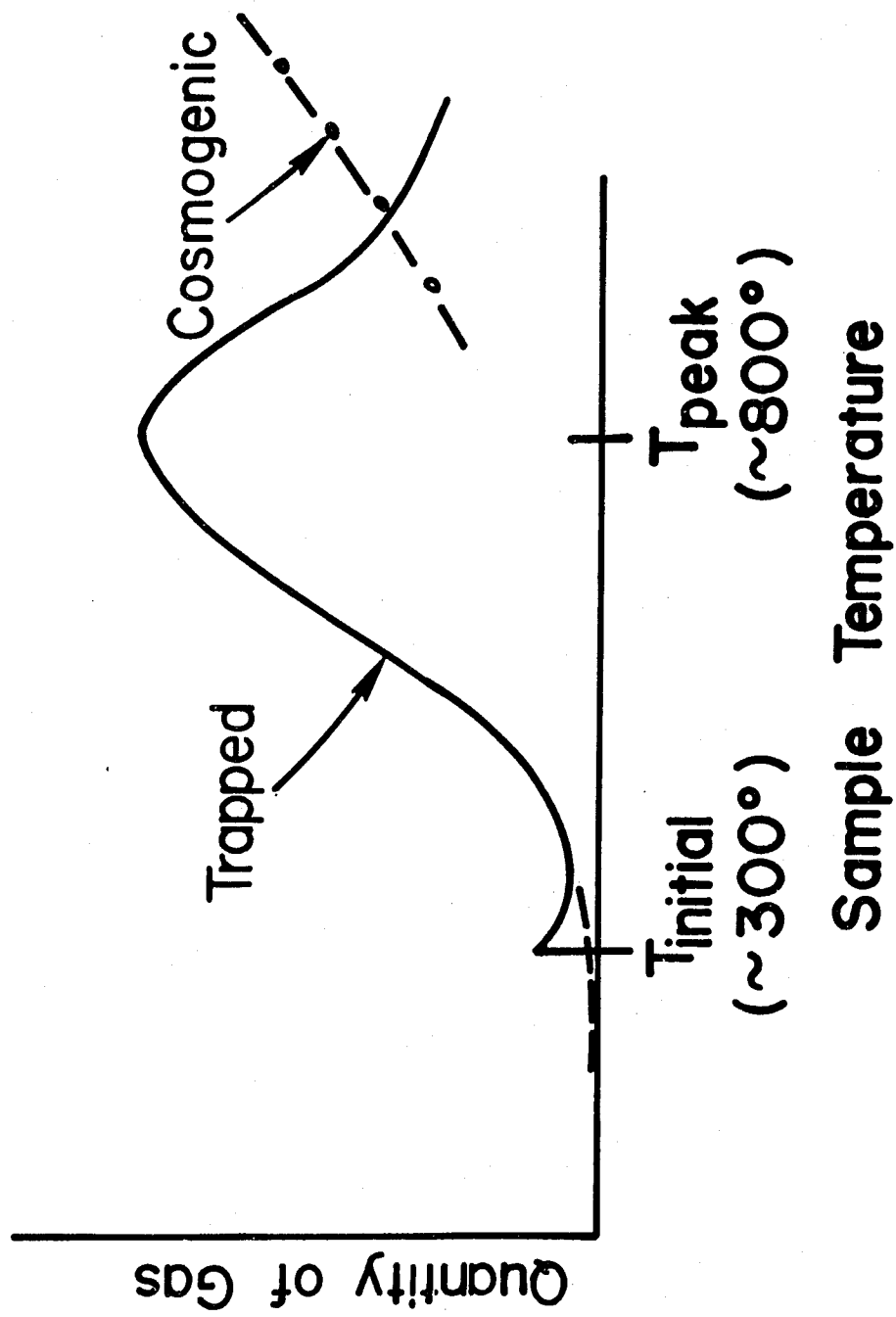
FIGURE 20

planation is an atmospheric effect (J. H. Reynolds, personal communication); we would also expect the possibility of mass fractionation on the basis of atmospheric trapping. The possible mass effect can be qualitatively seen from the model: two isotopes of a given element should have nearly identical trapping efficiencies but the lighter isotope has a slightly greater scale height and thus the ion travels further in the interplanetary electric field, impacts with greater energy, and is trapped with slightly greater efficiency. However, to calculate this increased trapping efficiency, the trapping probability must be integrated over the incident ion energy spectrum for each isotope

$$N_t = \int_0^\infty \eta_t(\mathscr{E}) \, n(\mathscr{E}) \, d\mathscr{E} \qquad (5-13)$$

where $n(\mathscr{E})$ is determined from the exponentially decreasing number density in the atmosphere and the resulting trajectory along the interplanetary electric field into the moon.

The results are presented in Table 8. The experimental lunar fine values are the enhancement of the given isotopic ratio measured at initial release temperatures over the

TABLE 8: Enhancement of the isotopic ratios, for gases released at the initial temperature compared to the peak release temperature, measured from lunar samples in a stepwise heating process. The experimental enhancement is compared to the inverse mass ratio and to the enhancement predicted by atmospheric trapping theory (Krypton data from Pepin et al. (1970); argon and neon data from Hohenberg et al. (1970)).

RATIO ENHANCEMENT AT LOW TEMPERATURE:

Ratio	Lunar Fines	m_2/m_1	Atmospheric Trapping
Kr^{83}/Kr^{84}	1.015	1.012	1.012
Kr^{83}/Kr^{86}	1.036	1.036	1.034
Kr^{84}/Kr^{86}	1.02	1.024	1.022
Ar^{36}/Ar^{38}	1.053	1.056	1.050
Ne^{20}/Ne^{22}	1.099	1.100	1.086

Example:

$$\text{Ratio Enhancement} = \frac{(Kr^{83}/Kr^{84}) \text{ initial temp}}{Kr^{83}/Kr^{84}) \text{ peak temp}} = 1.015$$

ratio measured at peak release temperatures. The values

for krypton were read from the straight line shown in the

data of Pepin et al. (1970). The values for argon and neon

were taken from the table of Hohenberg et al. (1970); the

ratio at initial release was calculated from the data for

the two lowest temperatures by taking an average weighted

by the quantity of gas released at each temperature.

Similarly the high temperature ratio was calculated from a

weighted average of the ratio for the two temperatures

giving peak gas release of the trapped component. The

enhancement expected from atmospheric mass fractionization

was calculated by numerically integrating the trapping

function of equation (5-2) over an approximate energy spect-

rum for the ions. As mentioned previously, the trapping

function probably has a finite cut-off energy which will

affect the above integration; however the ratio of the

integrals should not be greatly changed. An approximation

in the calculation is the use of the same trapping function

for Ne, Ar, and Kr. Also, only the first ionization go-

around is calculated; of the ions formed in the sunlit

atmosphere, about 60% escape the moon without impacting and

of the remaining 40% which hit the moon, part are trapped

and the remainder are released into the atmosphere where they can be reaccelerated, etc., thus possibly adding an additional contribution to the fractionation. Finally we assume that the isotopic ratio of the solar wind gases initially released into the atmosphere is just the ratio observed at peak gas release temperatures. It was pointed out by Hohenberg et al. (1970) that the enhancement is proportional to the inverse mass ratio of the isotopes, which is included for comparison.

Inspection of the data of Hohenberg et al. (1970) for the amount of gas in the initial release compared to total gas content of the element shows a decrease with increasing element mass which is consistent with the idea of the initial release gas coming from solar wind which had diffused out of the surface and been weakly reimplanted. However the same trend would also appear if the whole effect was just a preferential diffusion of light isotopes out when the sample is heated in the laboratory, though it is not clear that the isotopic ratios would then vary linearly with the inverse mass. A question arises because of the tightly bound Ar^{40} which is presumed to be atmospheric and yet has the same peak release temperatures as does Ar^{36}.

Another complicated phenomenon involves the amount of He^3 in the initial releases which could be somewhat large for atmospheric trapping since helium in the lunar atmosphere is not entirely gravitationally bound.

However the obvious feature of the results in Table 8 is the close agreement with experimental observations. It is clear that solar wind gases will be leaving the lunar surface and once in the atmosphere they can be retrapped and the trapping mechanism can cause some mass fractionation. The question is one of amount - can atmospheric trapping provide the amounts of gas observed for the various elements, and does the trapping effect dominate over the many complicated surface effects.

VI.

COMPARISON OF THE MODEL WITH CORRELATED

ION AND MAGNETIC DATA

A. Predicted Interplanetary Magnetic Field Direction

We discussed In Chapter IV the fluctuations of the

interplanetary magnetic field, $\bar{B}_{sw}$, out of the ecliptic

plane; the corresponding orientation of the interplanetary

electric field $\bar{E}_{sw}$ was also discussed, since $\bar{E}_{sw}$ is per-

pendicular to $\bar{B}_{sw}$ and since ideally $\bar{E}_{sw}$ should be near the

ecliptic in order to drive ions into one of the SIDE ex-

periments. The prediction of our model is that the best

condition for detecting ions from the lunar atmosphere is

when $\bar{B}_{sw}$ points strongly out of the ecliptic.

Referring to the calculations for ion trajectories

summarized in Table 6, we see that even intermediate mass

ions are not deviated much by the time they reach the lunar

surface. Thus, unless surface magnetic or electric fields

are quite strong, then there could be a good correlation

between fluxes seen in ion detectors and the orientation of

$\bar{B}_{sw}$. A sketch of the required orientation of $\bar{B}_{sw}$ is shown

in Figure 21. The view is looking toward the sunlit face of

Figure 21: Sketch of the desired angle of $\bar{B}_{sw}$

out of the ecliptic for ions to

enter SIDE.
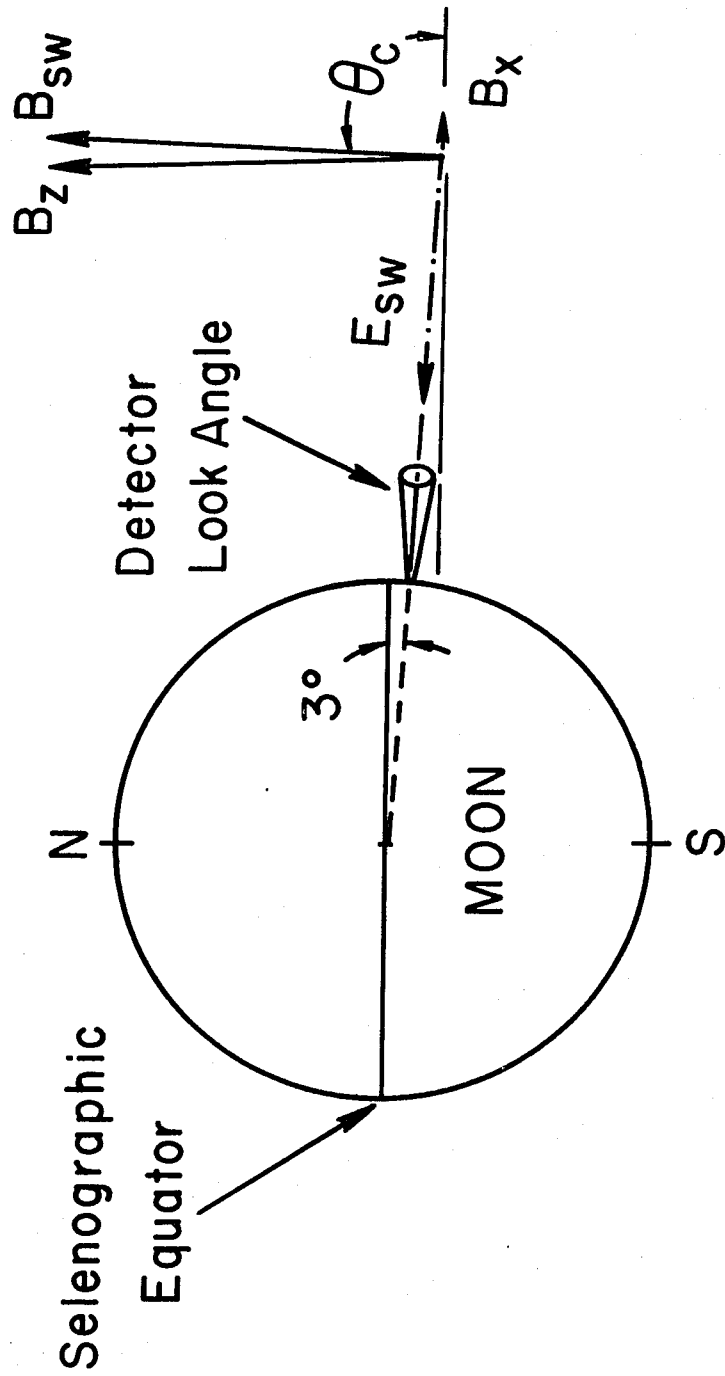
INTERPLANETARY ELECTRIC FIELD ANTIPARALLEL
TO DETECTOR LOOK ANGLE

FIGURE 21

the moon with the SIDE looking out into the ecliptic from the sunset terminator. The magnetic field is at an angle θ, almost 90°, out of the ecliptic. θ_c is the critical angle for ions to enter the detector, for $\bar{B}_{sw}$, θ_c is about 90° and for $\bar{E}_{sw}$ is about zero.

As mentioned earlier, the SIDEs look in the ecliptic and at about 15° longitude from radically outward. Since $\bar{E}_{sw}$ is also perpendicular to $\bar{V}_{sw}$, ions are likely to be seen near sunrise or sunset, provided that $\bar{B}_{sw}$ is sufficiently up or down out of the ecliptic as required. Thus we also look at the Detector-Sun (DS) angle in the ecliptic. The ideal geometry for detection is when

$$\text{DS angle} + 3^O \text{ SW aberration} = 90^O \tag{6-1}$$

The 3° solar wind aberration is only an estimate, as $\bar{V}_{sw}$ also fluctuates in direction. though not by a great amount (Axford, 1968).

B. **Characteristics of Ion and Magnetometer Data**

Specific Events Considered

As discussed above, certain ion events, such as sunrise/sunset or special impact events, may show evidence

of the acceleration that we predict. Also, the accelera-
tion model may explain the characteristics of the ion event
and its origin. Shown in Table 9 is a list of ion events
detected by SIDE, some of which we have correlated with
magnetometer data.

TABLE 9: List of SIDE Ion Events

Special Events

(1) LM Impact (Apollo 12) - (First Lunar Day)
     At 2217 z Nov. 20, 1969

(2) S-IVB Impact (Apollo 13)
     At 0109 z on April 15, 1970

(3) S-IVB Impact (Apollo 14)
     At 0740:55 z Feb. 4, 1971

(4) LM Impact (Apollo 14)
     At 0045 z Feb. 17, 1971

(5) Eclipse of Feb. 10, 1971
     At 0600 - 1200 z, Feb. 10, 1971 (Day 41, 1971)

Other Ion Events

(6) Continuous Spectra - After sunrise at ALSEP 1
     At 2027 to 2050 z Nov. 19, 1969

(7) Sunset at ALSEP 1
     At 0700 to 1100 z Dec. 4, 1969 (Day 338, 1969)

(8) Before Sunrise at ALSEP 1
     At 1830 - 1930 z Dec. 14, 1969 (Day 349, 1969)

(9) Before Sunset at ALSEP 1
    At 1100 - 1300 z, Jan. 2, 1970 (250 eV spectra)
    (Day 2, 1970)
    At 1930 - 2030 z, Jan. 2, 1970 (250 eV spectra,
    2000 eV spectra)

(10) One Day Before Sunrise (50 - 100 eV spectra)
     At 2000 - 2300 z, Jan. 16, 1970 (Day 16, 1970)

(11) Two Days Before Sunrise (250 - 750 eV spectra)
     At 0515 - 0730 April 13, 1970 (Day 103, 1970)

(12) After Sunset - (7 mo. after deployment)
     At 1600 - 1800 z, June 28, 1970 (Day 179, 1970)

(13) After Sunset - (8 mo. after deployment)
     At 0200 - 0500 z, July 28, 1970 (Day 209, 1970)

(14) High Fluxes in Tail
     At 1400 - 1600 z, March 11, 1971 (Day 70, 1971)

Summary of Events

In Table 10 we summarize the properties of interest

for those events in Table 9 for which magnetometer data has

kindly been provided by the Ames Lunar Surface and Explorer

35 Magnetometer experimenters. The Ion Features are espe-

cially important as some of the events listed are probably

not ions from the lunar atmosphere, at least they are not

what we might call an "ionosphere event" caused by ioniza-

tion along a column of atmosphere above the surface and

accelerated directly into the instrument.

The conclusion to be reached from Table 10 is that

TABLE 10: Ion-Magnetic Field Correlation (Apollo 12 SIDE)

Event	DS Angle	Ion Spectrum Features	Angle B_{sw} Out of Ecliptic	Correlation
6	$-90°$	24 hours after SR Immediately after deploy high counts, broad spectrum	$-65°$	Fair, $\bar{E}$ toward SIDE
7	$87°$	15 hours after SS Broad, low energy ionosphere spectrum	$+85°$	Good, $\bar{E}$ directly into SIDE
9	$84°$	13 hours after SS Only 250 eV ions	$+50°$	Poor
10	$-105°$	8 hours before SR Broad, low energy ionosphere spectrum	$-90°$	Good, $\bar{E}$ into SIDE
11	$-133°$	2-1/2 days before SR Only 750-1000 eV ions	$0°$	Bad
13	$80°$	3 hours after SS Only 250 eV ions	$+40°$	Poor

some ion events do indeed correlate with $\bar{B}_{sw}$ as predicted

by Manka and Michel (1970a, 1971a). In particular, those

events for which correlation is expected are the ones that

do correlate best. We discuss the energy spectrum of a low

energy "ionosphere" type event in Section D and see why

this spectrum is expected. The events which do not corre-

late well tend to have a sharp, higher energy spectrum.

They are possibly magnetosheath or bow shock ions (e.g.

Freeman, 1972) or could have been strongly affected by

surface electric and magnetic fields.

C.   Ion-Magnetic Correlation for Ionosphere Events

We look in detail at the two events discussed above

which appear to be well-correlated ionospheric events; in

particular we look at Event 7. Figure 22 shows the ion

count matrix for Event 7. Five ion bursts labeled A, B,

C, D, and E are readily seen and greatly exceed the back-

ground between the bursts. Figure 23 shows a portion of

the ion differential and integral flux data for the last

half of burst A (see Chapter 3 for a description of the

format).

In order to look for correlation, the integral ion

Figures 22a, 22b: Ion counts for Event 7 showing
the sharply defined ion bursts.

Figure 23: Sample SIDE differential and integral
flux data for burst A in Event 7.

Figures 24a, 24b: Plot of the integral ion flux
data for Event 7 along with the time-
correlated interplanetary magnetic field.
The dashed line in the B_x plot corresponds
to critical angles of $\bar{B}_{sw}$ and $\bar{E}_{sw}$ for ions
to enter the detector.

CHANNEL ENERGY

3500	3250	3000	2750	2500	2250	2000	1750	1500	1250	1000	750	500	250	100	70	50	30	20	10eV
338 7 24 8180																			
0	0	0	0	0	0	0	0	0	0	0	1	0	1	0	0	0	0	0	1
0	0	0	0	0	4	0	0	0	0	0	1	6	3	0	2	0	0	0	0
0	0	0	0	0	0	1	0	0	0	0	0	26	33	0	0	0	0	1	0
2	0	0	0	0	0	0	0	0	1	0	1	39	36	0	0	0	1	0	0
0	1	1	0	0	0	0	0	0	0	0	0	31	45	12	2	0	0	4	0
0	0	0	1	0	0	1	0	0	0	0	0	30	57	38	0	1	0	0	0
338 7 26 42737																			
0	0	0	0	0	1	2	0	3	0	0	0	12	30	0	0	0	0	0	0
0	0	0	0	0	0	2	0	0	0	0	0	16	83	5	0	0	0	0	0
0	0	0	0	0	0	0	0	0	0	1	0	13	87	0	0	0	0	1	0
0	1	0	0	0	0	0	0	0	0	0	0	26	88	0	2	0	0	0	2
0	0	1	0	0	0	0	1	0	0	0	0	1	18	0	0	4	0	0	0
0	0	0	0	1	1	0	3	0	0	0	0	0	0	0	16	1	0	0	0
338 7 29 17296																			
0	0	0	0	0	0	0	0	0	0	2	0	0	1	1	0	0	0	0	0
0	0	0	0	0	0	1	0	0	0	0	0	1	0	0	0	0	0	0	0
0	0	0	0	0	0	0	0	0	0	0	0	0	0	0	0	0	0	0	0
0	0	0	0	1	0	1	0	0	0	0	0	1	0	0	2	0	0	0	0
0	0	0	0	0	0	0	0	0	1	0	0	0	0	0	0	1	5	0	0
1	0	1	0	0	0	0	0	1	0	1	0	0	0	0	0	0	0	0	0
338 7 31 51856																			
0	0	1	0	0	0	0	0	0	0	0	0	0	2	0	0	0	1	0	0
1	1	0	0	0	0	0	0	0	0	0	0	0	0	0	0	0	0	0	0
0	0	0	0	0	0	1	1	2	0	0	0	0	0	0	0	0	0	0	0
0	0	0	0	0	0	0	0	0	0	0	0	0	0	0	0	0	0	0	0
0	0	0	0	0	1	0	0	0	1	0	0	0	0	0	1	0	0	0	0
0	1	0	1	0	0	1	0	0	0	0	0	0	0	0	0	0	0	0	0
338 7 34 26422																			
1	1	0	0	0	0	0	0	0	0	0	0	0	0	0	0	0	1	0	0
0	0	2	0	0	2	0	0	0	0	0	0	0	0	0	0	0	0	1	0
0	0	0	0	0	0	0	0	0	0	0	0	0	10	0	0	0	0	0	0
0	0	0	0	0	2	0	0	0	0	0	0	11	13	41	41	0	0	0	0
0	0	0	0	1	0	0	0	0	0	0	0	0	1	0	1	0	1	0	0
0	0	1	0	0	0	1	2	0	0	2	3	0	0	0	0	1	2	0	0
338 7 37 978																			
0	0	0	0	0	0	0	0	0	0	1	0	0	0	0	0	0	0	0	1
0	0	0	1	1	0	0	0	0	5	0	0	0	0	1	5	4	2	1	0
0	0	0	0	0	0	0	0	0	0	4	0	0	0	0	0	0	0	0	1
0	0	0	0	0	0	0	0	0	0	0	0	1	2	0	0	0	0	0	0
0	0	1	0	0	0	0	0	0	0	0	0	0	0	0	0	1	1	0	1
1	0	0	0	0	0	0	0	0	0	0	0	1	0	0	0	0	0	0	0
338 7 39 35538																			
1	0	0	0	0	0	0	0	0	0	0	0	0	0	0	0	0	0	0	1
0	0	0	0	0	0	1	0	0	0	0	0	0	3	0	0	0	1	0	0
0	0	0	0	0	0	0	0	0	2	0	1	0	1	0	0	0	0	0	0
0	0	0	0	0	1	0	0	1	0	0	1	1	1	0	0	0	0	0	0
0	0	0	0	0	0	0	0	1	0	0	0	0	0	0	0	0	0	0	0
0	0	0	0	1	3	2	0	0	0	0	0	1	0	0	1	0	0	0	0
338 7 42 10107																			
0	6	0	0	0	0	0	1	1	0	0	0	1	1	0	0	0	0	0	0
0	0	0	0	0	0	0	0	0	0	0	0	0	0	1	0	0	0	0	0
0	2	1	0	0	0	0	0	0	1	0	0	6	46	0	0	0	0	0	1
1	0	0	1	0	0	0	0	0	0	1	2	9	34	0	0	0	0	0	0
1	0	0	0	1	0	0	0	1	1	0	3	0	0	1	0	2	0	0	0
0	0	0	1	0	0	0	0	0	0	4	0	0	0	0	0	0	0	0	0
338 7 44 44667																			
0	0	1	1	0	1	4	0	1	0	0	0	0	2	0	0	0	0	0	0
0	0	0	0	0	1	0	3	0	0	0	0	0	0	0	0	1	0	0	0
0	0	1	0	0	0	0	0	0	1	1	0	2	0	0	0	0	0	0	0
0	0	0	0	0	0	0	0	0	0	0	0	0	0	0	0	0	1	0	0
1	0	0	1	0	0	3	0	0	0	1	0	0	0	0	0	0	1	0	0
2	0	0	0	0	0	3	0	0	0	1	0	0	8	0	0	1	0	0	0

FIGURE 22 a

```
339  7 47 19222
     0   0   0   0    0   1   2   3   0   4   0    0  15   0   0   0   1   0   2   0
     0   1   0   0    0   0   0   1   1   1   1    4   5  17   0   0   0   0   0   0
     0   0   0   0    0   0   0   0   0   1   0  C  3  27  43   0 143   2   0   0   0
     0   0   0   0    0   4   0   0   0   1   1    4  14  16 121 127  25   2   0   0
     0   0   0   0    0   0   1   0   2   1   0    2   7   8  28   0   0   0   0   0
     0   0   0   0    0   0   0   0   0   0   0    2   2   0   0   1   0   0   0   0
339  7 49 55788
     0   0   0   1    2   0   0   0   2   0   0    0   0   0   0   0   0   0   0   0
     0   0   0   0    0   1   0   0   0   0    0   0   0  27   0   0   3   0   0   0
     0   0   0   0    0   0   0   0   0   0  D  2  11  15  32   0   0   0   0   0
     0   0   0   0    0   0   0   0   0   0    0   4   9  98   3   0   0   0   0
     0   4   0   0    0   0   0   0   1   0    0   0   0   0   1   0   1   0   0
     1   0   0   0    0   0   0   2   0   0    0   0   0   0   1   0   1   0   0
338  7 52 28339
     0   0   0   0    0   2   0   0   0   1   0    0   0   1   0   0   0   0   0   0
     0   0   1   0    0   0   0   0   0   0   0    0   0   0   0   0   0   0   0   0
     0   0   0   0    2   0   0   1   0   0   0    0   0   0   0   0   0   0   0   0
     0   0   0   0    0   1   0   0   0   0   0    0   1   2   0   0   1   1   0   0
     0   0   0   0    0   0   0   0   0   0   0    0   0   0   0   0   2   0   0   4
     0   0   0   1    0   0   0   0   0   0   0    0   2   0   0   0   0   0   1   0
339  7 55 2900
     0   0   0   0    0   0   0   0   0   0   0    0   0   0   0   0   2   0   0
     0   0   0   1    0   0   0   0   3   0   0    0   0   0   0   4   2   0   0
     0   0   0   0    5   0   0   1   1   0   0    0   1   0   0   1   0   0   0   0
     0   0   0   1    0   0   0   0   0   1   0    0   0   0   0   0   0   0   1
     0   0   0   0    0   1   0   0   0   0   0    0   0   0   0   0   1   0   0
     0   0   0   0    0   0   0   0   1   1   0    0   0   0   0   1   0   1   0   0
339  7 57 57469
     0   0   0   0    0   0   0   0   0   0   2    1   0   1   0   0   0   0   0   0
     0   0   0   0    1   2   0   0   0   0   0    0   0   0  34   5   0   0   1   1
     0   2   0   0    0   0   0   0   0   1   0    1   0   2   0   0   0   0   0
     0   0   0   0    0   0   0   0   0   1   0    0   0   0   0  20   0   0   0
     0   0   0   1    0   0   0   0   0   2   0    0   0   0   2   0   0   0   0   1
338  8  0 12021
     0   0   0   1    0   0   0   0   0   0   0    0   0   0  10   0   0   0   1
     0   1   0   0    0   4   0   2   0   0   0    2   0   0   1   0   0   0   0   0
     0   0   0   0    0   0   0   0   0   0   0    0   0   0   1   0   0   0   0   8
     0   0   1   0    0   0   0   0   0   0   0    1   0   0   0   0   0   0   0   0
     0   0   0   0    2   1   0   0   0   0   1    0   0   5   0   0   2   0   0   0
338  8  2 46590
     0   0   0   0    0   2   0   0   1   0   1    0   0   0   0   0   0   0   0
     0   0   0   2    0   0   0   1   0   0   0    3   0   0   0   2   0   0   1   4
     0   1   1   0    0   0   0   0   0   1    0   1   0   0   0   0   0   0   0
     0   0   0   2    3   0   0   1   0   0   0    0   0   0   0   0   0   0   0
     1   0   0   0    0   0   0   0   3   0   2    0   3   0   0   0   7   0   0   0
     0   1   0   0    0   1   0   0   0   0   0    0   3   0   0   1   4   1   0   0
338  8  5 21150
     0   0   0   0    0   0   0   1   0   0   0    0   0   0   0   1   0   0   0
     0   0   0   0    1   0   0   0   0   0   0    0   0   1   0   0   0   0   0
     0   0   0   0    0   0   0   0   1   0   0    0   0   0   0   0   0   0   1   0
     1   0   1   0    0   0   0   1   0   0   0  E1 1 155   0   0   0   0   1   0
     0   0   0   0    0   0   0   0   0   0   0    0  16   0   1   0   0   0   0
     0   0   0   0    0   0   0   0   0   0   0    0   0   2   0   0   1   1   0   0
339  8  7 55710
     2   1   0   0    0   0   0   0   0   0   0  E2 1 103   0   0   0   0   0   1   0
     0   0   0   0    0   1   0   0   0   0   1    0   0   0   0   0   0   0   0
     0   0   0   0    0   0   0   1   0   1   0    0   5   0   5   0   0   0   0
     0   0   2   0    0   0   0   0   0   0   0  E3 2  15   1   1   0   0   0   2
     0   0   0   0    0   0   0   1   0   0   1    0   0   1   0   0   0   0   0
338  8 10 30271
     0   0   0   0    1   0   0   0   0   0   0    1   1   0   0   0   0   0   0   1
     0   0   0   0    0   0   0   1   0   0   0    0   0   0   0   0   0   0   0   1
```

FIGURE 22 b

```
E  V  E  N  T      7
TYPE IN START TIME, END TIME AS
D AY H RMN DAY HRMN
338 0725 338 0733
NOW AT STARTING TIME 338   7 25
OUT OF TOLERANCE OR PARITY ERROR AT 338   7 25 33909 SFM = 70


TIME IS 338  7 26
DIFFERENTIALS
        0.          0.        0.        0.        0.         39.        88.
        0.        177.        0.        0.        0.       2124.     18619.
        0.          0.        0.        0.        0.          0.
     INTEGRAL FLUX=           2751272. IONS/[SEC SQ CM STER]


DIFFERENTIALS
        0.          0.        0.        0.        0.          0.        88.
        0.          0.        0.        0.        0.       2832.     29361.
     4425.          0.        0.        0.        0.          0.
     INTEGRAL FLUX=           7004425. IONS/[SEC SQ CM STER]


DIFFERENTIALS
        0.          0.        0.        0.        0.          0.         0.
        0.          0.        0.       88.        0.       2301.     30796.
        0.          0.        0.        0.     4425.          0.
     INTEGRAL FLUX=           6800885. IONS/[SEC SQ CM STER]


DIFFERENTIALS
        0.         27.        0.        0.        0.          0.         0.
        0.          0.        0.        0.        0.       4602.     31150.
        0.       2528.        0.        0.        0.      17699.
     INTEGRAL FLUX=           7539045. IONS/[SEC SQ CM STER]


DIFFERENTIALS
        0.          0.       29.        0.        0.          0.         0.
       51.          0.        0.        0.        0.        177.      6372.
        0.          0.     7280.        0.        0.          0.
     INTEGRAL FLUX=           1480194. IONS/[SEC SQ CM STER]


DIFFERENTIALS
        0.          0.        0.        0.       35.         39.         0.
      152.          0.        0.        0.        0.          0.         0.
        0.      20228.     1770.        0.        0.          0.
     INTEGRAL FLUX=            597696. IONS/[SEC SQ CM STER]


D ISCONTINUOUS D ATA AT 338   7 31  3556                  SFM= 87


TIME IS 338  7 29
D IFFERENTIALS
        0.          0.        0.        0.        0.          0.         0.
        0.          0.        0.      177.        0.          0.       354.
      885.          0.        0.        0.        0.          0.
     INTEGRAL FLUX=            194690. IONS/[SEC SQ CM STER]


D IFFERENTIALS
        0.          0.        0.        0.        0.          0.        44.
        0.          0.        0.        0.        0.        177.         0.
```

FIGURE 23
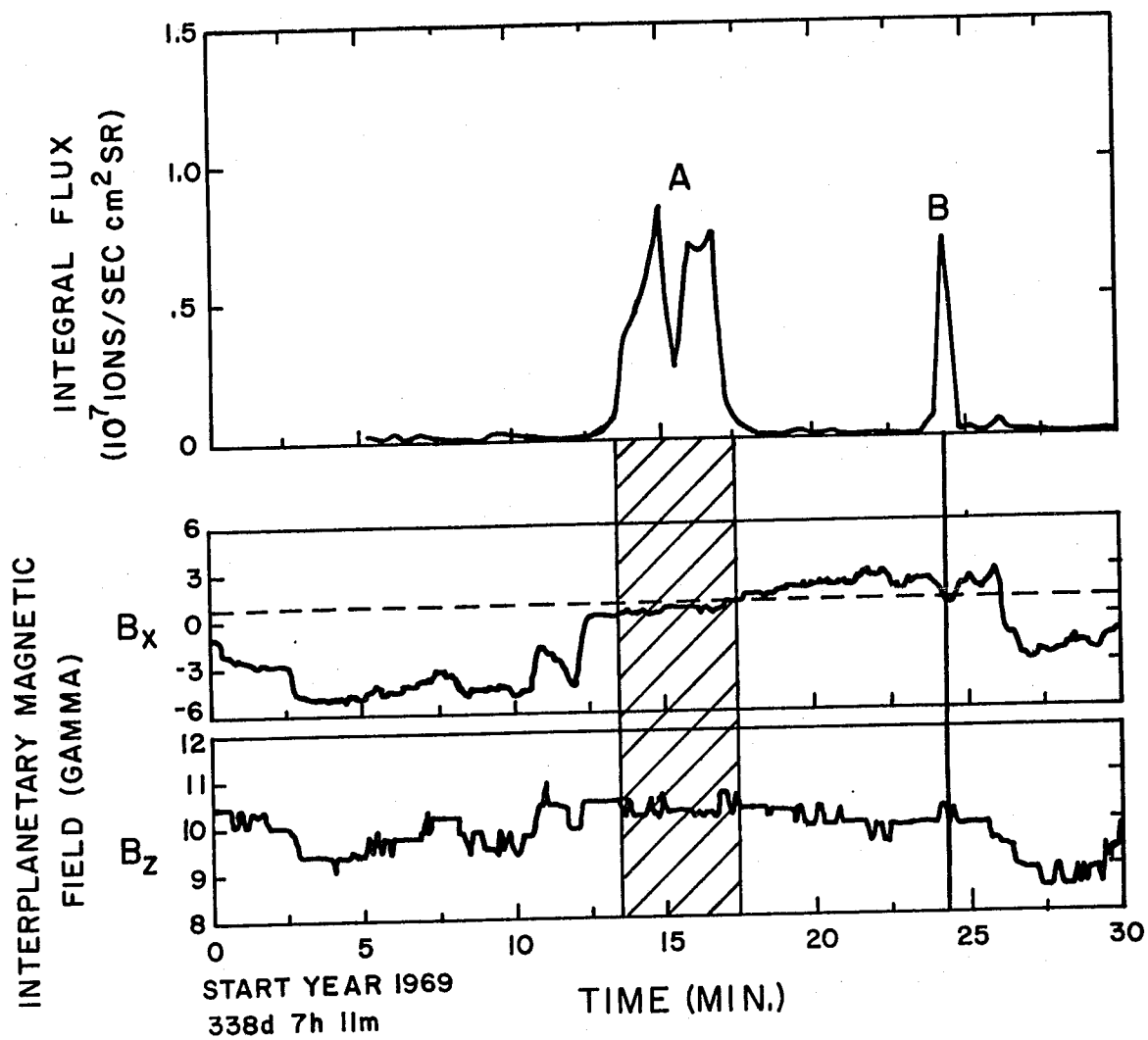
FIGURE 24 a
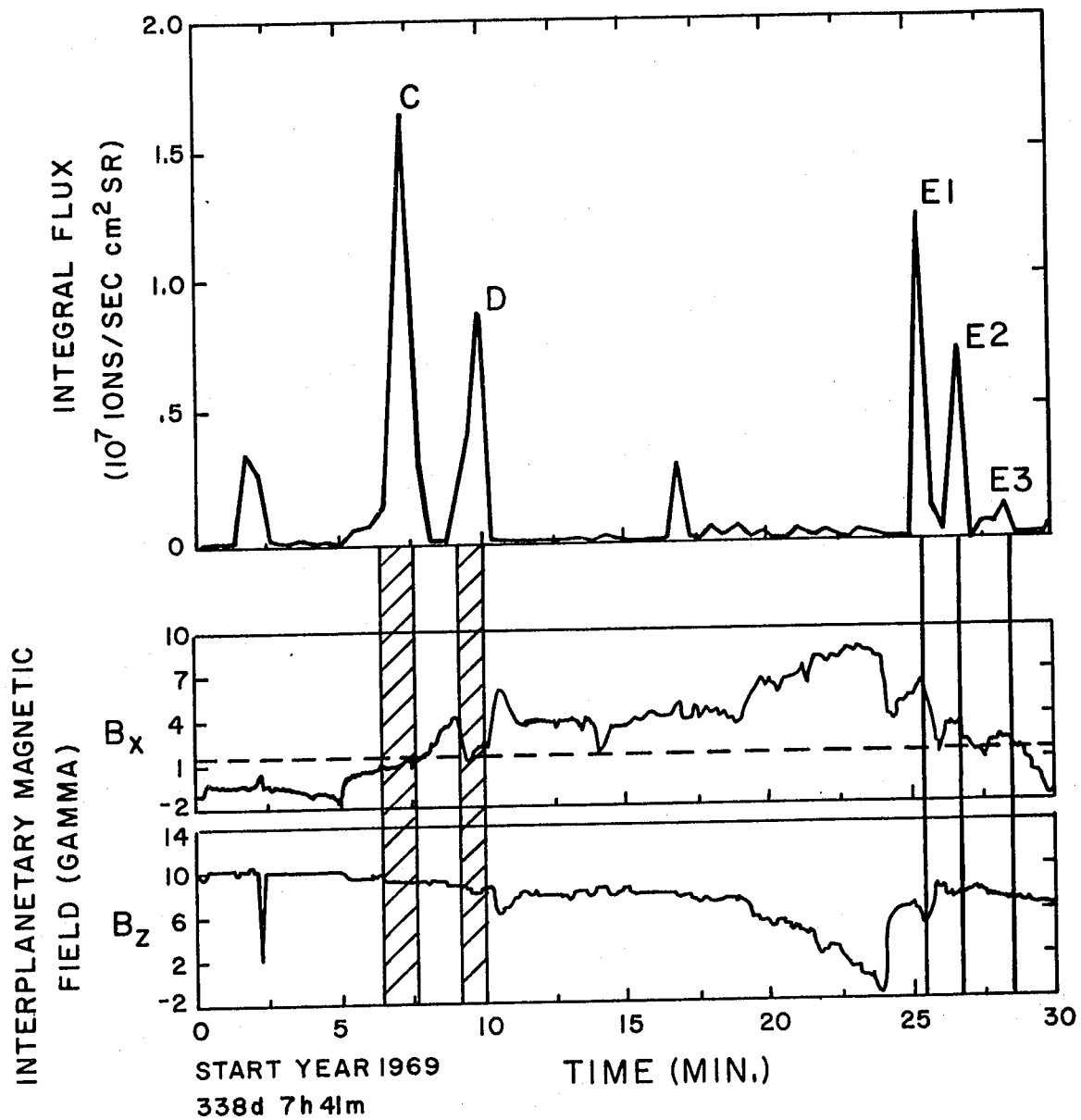
FIGURE 24b

flux from the Apollo 12 SIDE is compared in time with the
interplanetary magnetic field in LSM coordinates. Using
a standard program developed by the SIDE project (Tom
Rich, personal communication), the integral flux data, such
as shown in Figure 23, is plotted in Figure 24. As we will
show here, a reasonable conclusion for this event is that
the flux is quite uni-directional, and can be expressed as
such by using equation (2-5). Plotted below the ion data
are the x and z components of the interplanetary magnetic
field. The coordinates were discussed in Chapter II and the
predicted magnetic field components for ions to enter the
SIDE are shown in Figure 21. We see from Figure 21 that a
small B_x and a large, positive B_z will give $\bar{B}$ almost at
right angles to the ecliptic and of the proper polarity so
that $\bar{E}_{sw}$ is driving ions toward the detector rather than
oppositly away. Thus when the SIDE is near local sunset,
a large, positive B_z is required while near local sunrise,
a large, negative B_z is required. When the times during
which ions are detected are projected on the magnetic field,
for example the shaded area under burst A in Figure 24a,
then a rather striking correlation is found. In particular,
is is seen that there is a critical value of B_x, of about

one gamma, for which ions are detected. This critical

value also appears for bursts B, C, and D. The value of

B_z is not as critical; it remains about 10 gamma throughout

the event and since the critical angle for $\bar{B}$ is given by

Figure 21

$$\tan \theta_c(B) = \frac{B_z}{B_x} \tag{6-2}$$

and B_z is large, then θ_c is most sensitive to B_x.

The peaks E1, E2, and E3 are not completely understood

as they seem to be shifted in time from the critical values.

Some properties of these bursts should be noted. The count

data in Figure 22b shows that E1 and E2 occur in single

channels, i.e. only at energies of 100 and 250 eV respectively

and are measured during the 1.13 seconds that the channel

accepts ions. Two possibilities present themselves. One

is that there was a rapid fluctuation of the field to the

critical angle; however, an examination of the high resolu-

tion printer output from the LSM for this time does not

show such fluctuations (P. Dyal and C. W. Parkin, personal

communication). Another possibility is that the orbit of

the Explorer 35 satellite introduced a time shift due to

the separation of the satellite position and the SIDE site
on the moon. The orbit of Explorer 35 at this time is
given in Figure 3 and the satellite was about 4 R_M upstream;
however the effect of this time delay is to increase slightly
the discrepency in timing. Thus, at this point we do not
have a good understanding of these "spike" counts and per-
haps other effects such as surface fields are important.

However the four main bursts during this event do show
remarkable correlation. We have estimated the allowed var-
iation in θ_c for $\bar{E}_{sw}$ for these four bursts as shown in
Table 11. If the Apollo 12 SIDE is assumed to be perfectly
leveled and looking radially out of the moon (but 15° from
local vertical in longitude), then the fluxes are seen when
the electric field has a critical angle of 4.5^O to 7.5^O;
i.e., $\bar{E}_{sw}$ is pointed almost straight into the detector!
Furthermore, the deviation about this critical angle is
typical a few degrees, which is consistant with the SIDE
look angle of $\sim 3^O$.

Excellent correlation, such as observed in Event 7 is
also found in Event 10. In this unusual event, $\bar{B}_{sw}$ stays
nearly at right angles to the ecliptic plane for a period
of several hours and the SIDE shows strong flux counts as

BURST	A	B	C	D	E1	E2	E3
Deviation of θ_c from SIDE Look Angle	4.5°	4.5°	6.5°	7.5°	33°	17°	13°
Fluctuation in θ_c	+2° -4°	±1°	±2°	+1° -10°			

$\bar{B}_{sw}$ passes through the critical angle. A thirty minute segment of this data is shown in Figure 25.

D. Energy Spectrum of the Lunar Ionosphere

In the case when the ions are being accelerated straight in radially toward the lunar surface, as in Events 7 and 10, then the distribution of ion energies is given by equation (5-7) with $\cos \theta = 1$:

$$dn_i(\mathcal{E}) = \frac{n_{io}}{E} \ e^{\frac{-\mathcal{E}}{Eh}} \ d\mathcal{E} \tag{6-3}$$

or, within the energy channel of width $\Delta \mathcal{E}$,

$$\Delta n_i (\mathcal{E}) \simeq \frac{n_{io}}{E} \ e^{\frac{-\mathcal{E}}{Eh}} \ \Delta \mathcal{E} \tag{6-4}$$

where n_{io} is the number density at the surface. But for the SIDE, the band width is approximately proportional to the energy of the energy channel

$$\Delta \mathcal{E} \simeq 0.1 \ \mathcal{E} \tag{6-5}$$

(Actually, recent work on the calibration indicates that this relationship is only approximate, with some possible variation for some of the energy channels; R. A. Lindeman, personal communication). Thus the energy spectrum becomes

Figure 25: Plot of the integral ion flux data

for Event 10 along with the time-

correlated interplanetary magnetic

field
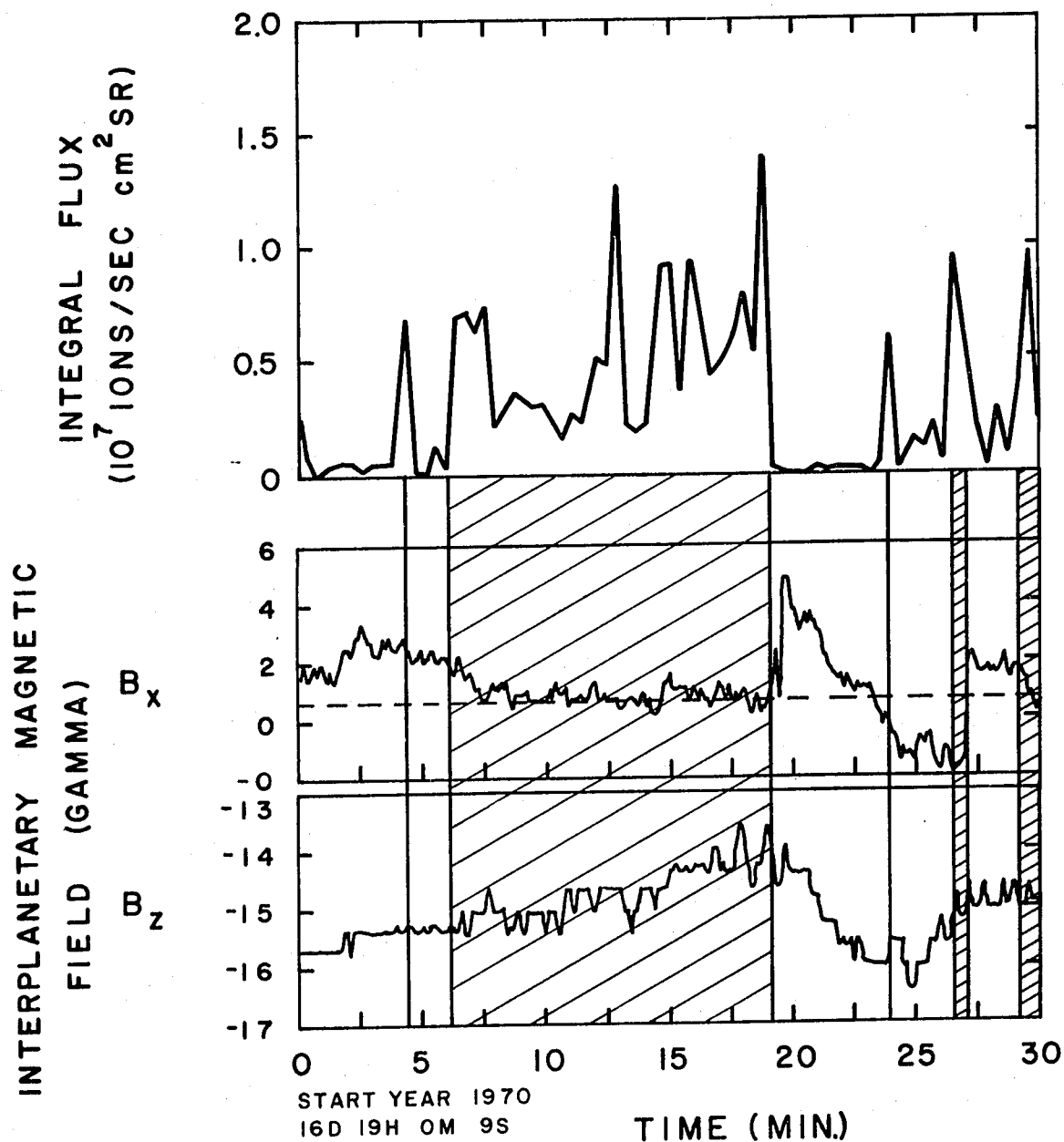
FIGURE 25

$$\Delta n_i (\mathcal{E}) = \frac{n_{io}}{E} \; 0.1 \, \mathcal{E} \, e^{\frac{-\mathcal{E}}{Eh}} \tag{6-6}$$

which is proportional to the number of counts per energy channel and is the product of $\mathcal{E}$ times the negative exponential of $\mathcal{E}$.

The insert in the upper right hand corner of Figure 26 shows each of these separate functions as dashed lines and the product, giving the energy distribution, as a peaked solid line. We see that

$$\Delta n_i (\mathcal{E}) \rightarrow 0 \quad as \quad \begin{cases} \mathcal{E} \rightarrow 0 \\ \mathcal{E} \rightarrow \infty \end{cases} \tag{6-7}$$

We can now evaluate the energy at which the peak in the distribution curve occurs by differentiating the function and equating the derivative to zero

$$\frac{d \; \Delta n_i (\mathcal{E})}{d\mathcal{E}} = \frac{0.1 \, n_{io}}{E} \left[e^{\frac{-\mathcal{E}}{Eh}} - \frac{\mathcal{E}}{Eh} \, e^{\frac{-\mathcal{E}}{Eh}} \right]$$

$$= \frac{0.1 \, n_{io}}{E} \; e^{\frac{-\mathcal{E}}{Eh}} \left[1 - \frac{\mathcal{E}}{Eh} \right]$$

$$= 0 \tag{6-8}$$

which implies

$$\mathcal{E} = Eh \qquad\qquad (6\text{-}9)$$

Thus we see that the ion count spectrum is peaked at an energy equal to the interplanetary electric field times the scale height. If the ion energy is measured, and we can calculate $\bar{E}_{sw}$ from $\bar{V}_{sw}$ and $\bar{B}_{sw}$, then the scale height can be estimated and also the species mass.

With the spectrum given by equation (6-6) we have a quantitative feeling for the spectrum of these ions which are from the lunar atmosphere and accelerated by our mechanism. Plotted in Figure 26 are the theoretical spectrum (solid line) and the spectrum for Event 7 (dotted line). We see that the measured spectrum generally follows the predicted curve, but is somewhat narrower, particularly at higher energies. In general however, the spectrum appears to be a good "ionosphere" fit. The high energy decrease could easily be due to the narrow acceptance cone of the SIDE; as shown in Table 6, ions of different energies have slightly different directions at impact. Also, since this event was observed only a few weeks after deployment, some gas may still be evolving from the surface and thus

Figure 26: Plot of the predicted and observed

ion count spectrum for Event 7 seen

by the Apollo 12 SIDE. The energy

is normalized to the energy for which

the peak number of counts occurs

(250 eV for this event).

ION COUNT SPECTRUM
(1969 day 338 hr 7)
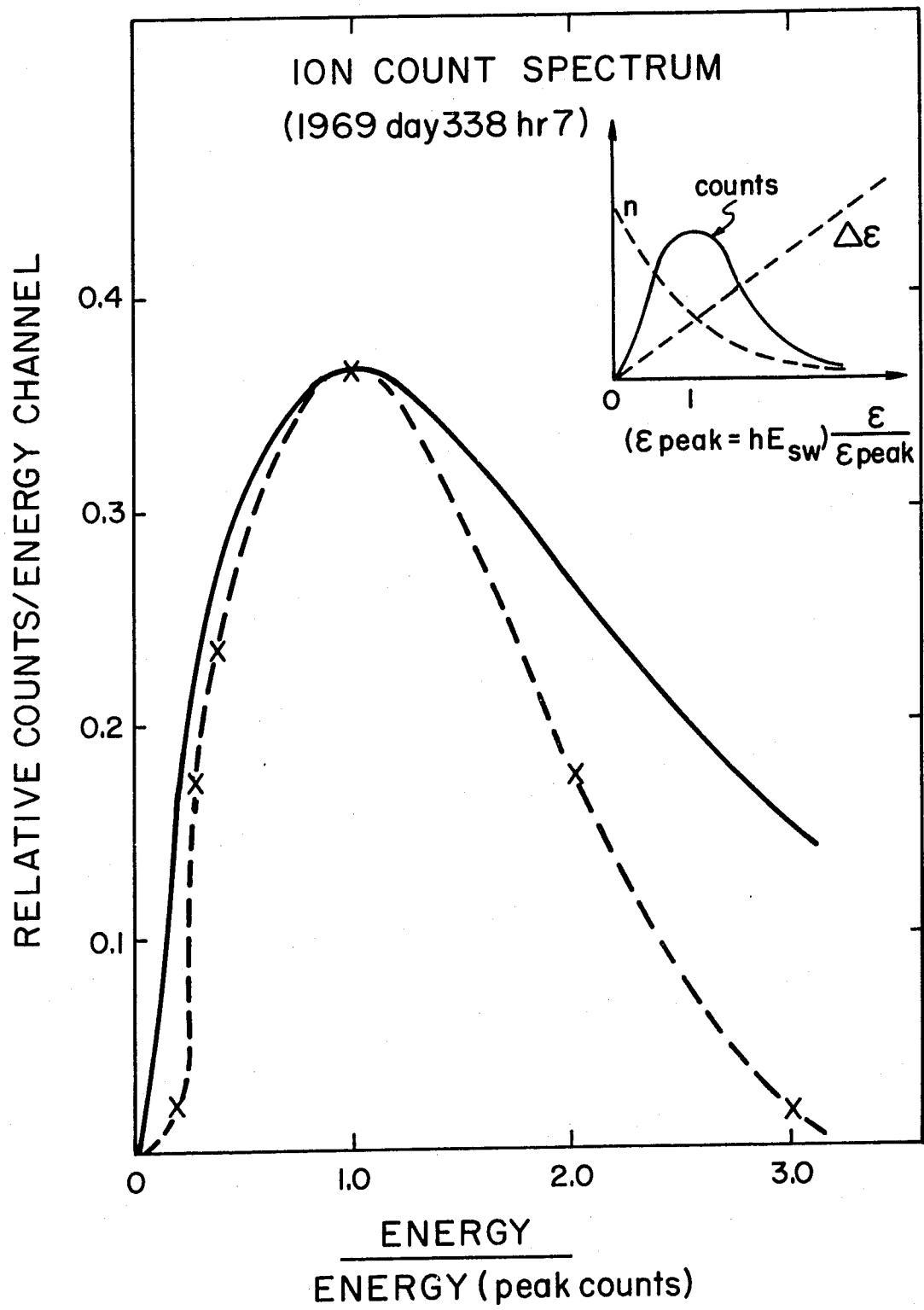
FIGURE 26

weight the density distribution nearer to the surface.

Finally we should note that use of an exponential atmosphere

is an assumption, though apparently a fairly good one;

kinetic calculations of the lunar atmosphere have been made

by Hall (1968) and Yeh and Chang (1972) who obtain density

variations similar to the exponential distribution.

Another form of the same event is shown in Figure 27

where the log of the differential ion flux is plotted for

each energy channel; this plot shows the complete real-time

ion flux in each of the ten lowest energy channels. The

duration of the major bursts A, B, C, and D are indicated.

Because the log of the flux is plotted, it is somewhat

difficult to tell at first glance where the major fluxes are

being recorded.

E.   The "Water Vapor" Event

On March 7, 1971, the Apollo 14 SIDE detected an intense,

prolonged series of ion bursts and the Mass Analyzer (MA)

showed the ions to be primarily in the number 5 mass channel

(18.0 to 23.3 amu/charge) with some counts in adjacent

channels (Freeman et al., 1972a; Freeman et al., 1972b).

Ions were detected in both the TID and the MA from about

Figure 27:   Log of differential flux in each of

the lowest ion energy channels.   The

plot shows the complete, real-time

flux for this thirty five minute seg-

ment of Event 7.
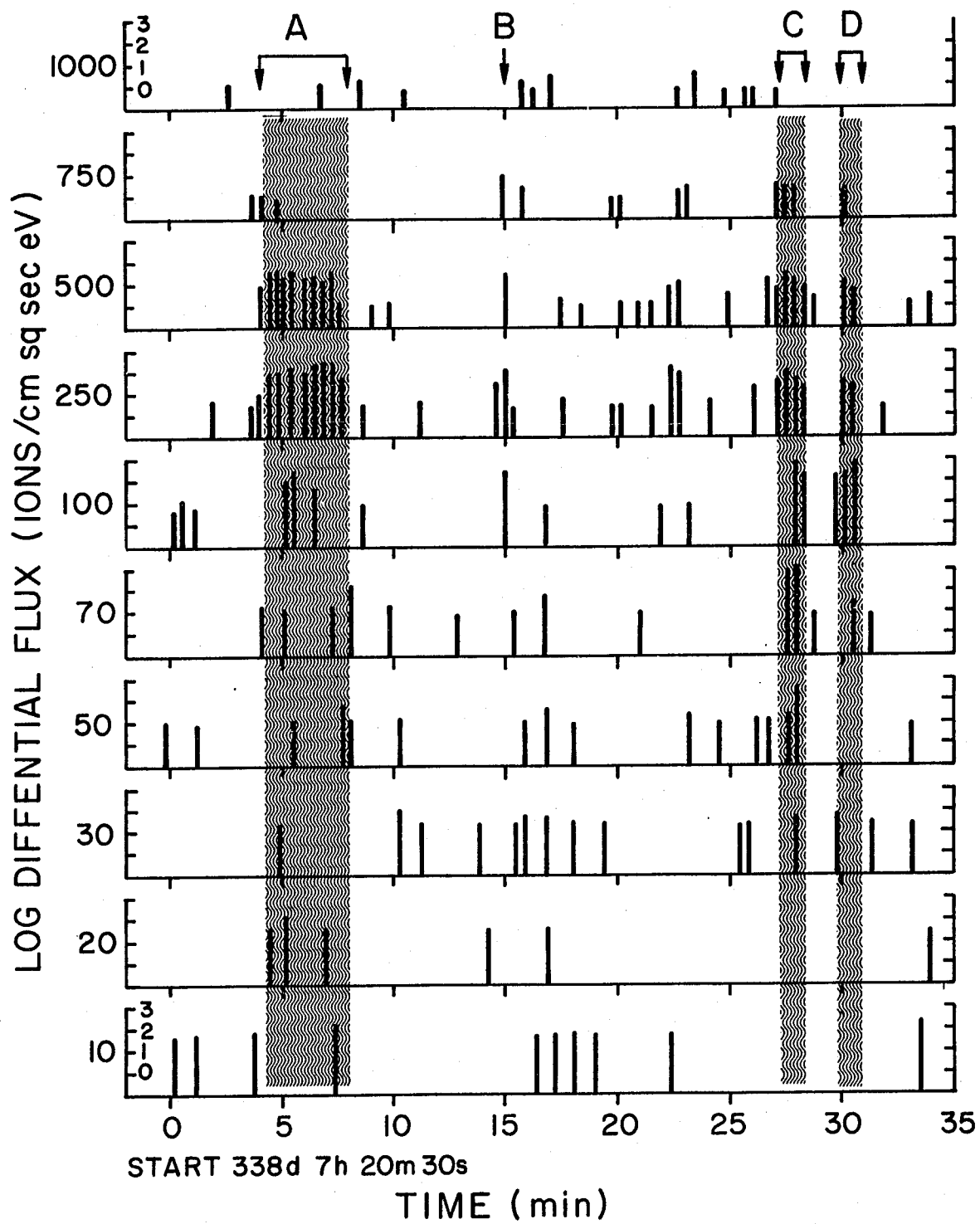
FIGURE 27

0400 to 0900, 1700 to 2000 hours, and an especially big

burst at 1205 in the 48.6 eV channel of the MA.

We will take a brief, qualitative look at the event

from the standpoint of our model and the available related

data.

Solar Wind:

Preliminary data for the solar wind speed was obtained

from the SWS experimenters (C. Snyder, personal communica-

tion) and the approximate conditions are, for Day 66, 1971:

0600 Hours:	$V_{sw} = 340$ km sec^{-1}
1130 to 1230 Hours:	$V_{sw} = 305$ decreasing
	to 280 km sec^{-1}
1200 Hours:	$V_{sw} \simeq 295$ km sec^{-1}
1800 Hours:	$V_{sw} = 275$ km sec^{-1}

Interplanetary Magnetic Field:

Preliminary data for $\bar{B}_{sw}$ was obtained from the Ames

Explorer 35 Magnetometer experimenters (D. S. Colburn, per-

sonal communication). The data is just in the process of

being transformed from satellite coordinates to geo-rela-

ted coordinates so that the components quoted below are

only approximate. One of the coordinate systems used is

solar ecliptic where x is toward the sun z is north out of

the ecliptic, and y completes the right hand coordinate
system so that y points radially outward in the ecliptic at
the sunset terminator. Thus the ratio of B_z/B_y defines the
angle out of the ecliptic just as B_z/B_x did in LSM coordi-
nates.

0600 Hours: $B_y \approx 4$ gamma, $B_z \approx 4$ gamma

$\Rightarrow \theta \approx 45°$, $B_\perp = 5.7$ gamma

1200 Hours: $B_y \approx 3.5$ gamma, $B_z \approx 10$ gamma

$\Rightarrow \theta \approx 71°$, $B_\perp \approx 10.5$ gamma

1800 Hours: $B_y \approx 4.3$ gamma, $B_z \approx 5.8$ gamma

$\Rightarrow \theta \approx 53°$, $B_\perp \approx 7.1$ gamma

The best "observing conditions" appear to be around 1200
hours, and it is actually just shortly before 1200 hours,
at about 1150 hours, when the field becomes well out of
the ecliptic.

Ion Energies

Many of the ions are seen at 48.6 eV in the MA and at
70 and 100 eV in the TID.

Ion Height - Energy Relations

Using

$B_{sw\perp} \simeq 10.5$ gamma (Preliminary data Ames Explorer 35 Magnetometer)

$V_{sw} \simeq 295$ km sec^{-1} (Preliminary data Solar Wind Spectrometer)

then we calculate the interplanetary electric field

$$\left| E_{sw} \right| = \left| -\bar{V}_{sw} \times \bar{B}_{sw} \right| = V_{sw} B_{sw\perp}$$

$$= 3.1 \text{ volts km}^{-1} \tag{6-10}$$

If we now make the assumption that the principal energy source of the accelerated ions is the interplanetary electric field, then the energy is given by

$$\mathscr{E} = \text{height} \times E_{sw} \tag{6-11}$$

For $\mathscr{E} = 48.6$ eV, height = 16 km

For $\mathscr{E} = 70$ eV, height = 23 km

For $\mathscr{E} = 100$ eV, height = 32 km

Thus we find that these calculated heights reasonable for an atmospheric gas and below the orbit of the CSM (~ 100 km). However, this calculation must be taken with some reservation since the orientation of $\bar{B}_{sw}$ is not ideal for detecting

ions. If the surface magnetic field deflects the ions, then
it does not change the energy and the calculation is correct.
However, if the surface potential is of the order of -40
volts (Chapter III) then that energy must be subtracted from
the observed energy and the implied height of formation is
thereby lowered.

F.   Discussion of Events and Model

Some of the conclusions to be drawn from the data in
this chapter are:

1. The relatively low energy, sunrise/sunset events
    are the type predicted by Manka and Michel.

2. Properties of the events, such as their energy
    spectra, fit the predictions of the model.

3. For some very good "ionospheric" events, the ion
    flux shows very detailed correlation with the
    orientation as predicted by Manka and Michel
    (1970a).

4. Implications are that some events fit the ex-
    pected lunar ionosphere dynamics and are closely
    correlated with $\bar{B}_{sw}$ while other events do not.
    This implies that these other ion events are not

ambient lunar ionosphere, or that other effects,

such as surface electric and magnetic fields, are

playing important roles.

VII.

CALCULATION OF DENSITY OF THE

NEUTRAL LUNAR ATMOSPHERE

In this chapter, we make use of the information deve-
loped in the preceeding chapters in order to calculate the
number density of the neutral lunar atmosphere. We calcu-
late two neutral atmosphere densities: the average density
of Ar^{40} and the total neutral density at sunrise and sunset.
The Ar^{40} density is deduced from the amount of Ar^{40} found
trapped in the lunar surface and the trapping calculations
described in Chapter V; this may be the most quantitative
calculation to date for the density of Ar^{40}.

The total neutral number density of the atmosphere
is calculated from SIDE ion flux data. Using our accelera-
tion model and the predicted theoretical energy spectrum,
we determine the neutral density at the time of one sur-
rise and one sunset ion event. This calculation is quite
accurate as we assume only the model atmosphere and an
average ionization time; we thus obtain, in effect, the
second measurement that has been made of the neutral at-
mosphere, after the CCGE, and the values agree within a

factor of two with the CCGE (Johnson et al., 1972a).

A.   Argon-40 Density in the Lunar Atmosphere

From the analysis of the acceleration of atmospheric ions, some further properties of the lunar atmosphere can be deduced. The approximately equal concentrations of Ar^{40} and Ar^{36} in the lunar soil implies that the respective ion fluxes are related by the trapping efficiencies and geometries appropriate for the trapping of lunar atmosphere or solar wind ions, and allows us to estimate the density of Ar^{40} in the lunar atmosphere.

Fluxes of Solar Wind Elements

In the lunar soil samples the concentrations of Ar^{40} and Ar^{36} are very nearly equal, which implies that the incoming fluxes are proportional (but not necessarily equal). In our Science paper (Manka and Michel, 1970c), it is shown that the likely source of Ar^{40} is the lunar atmosphere (see Chapter V of this thesis) while the Ar^{36} is primarily from the incident solar wind. Starting with approximately equal concentrations in surface fine material at the lunar equator (for example see Heyman et al., 1970), the fluxes of the

two isotopes can be calculated from the expected flux of Ar^{36} in the solar wind and the calculations for trapping efficiency and trajectories of Ar^{40} ions from the lunar atmosphere.

First, we estimate the flux of Ar^{36} in the solar wind by relating it to known fluxes of helium and neon. It is difficult to obtain a true flux for an element which is not plentiful in the solar wind as the exposure time may not be sufficient to detect the element; also, the ratio of two elements may be strongly affected by diffusion in the trapping material.

The average solar wind flux of hydrogen for a model solar wind at density $n(H) = 5$ cm^{-3} and velocity $V_{sw} = 400$ km sec^{-1} (proton energy = 870 eV) is

$$\Phi(H) = 2 \times 10^8 \text{ cm}^{-2} \text{ sec}^{-1} \qquad (7-1)$$

From Robbins et al. (1970), Vela satellite measurements show average values of velocity

$$\langle V_{sw} \rangle = 399 \simeq 400 \text{ km sec}^{-1} \qquad (7-2)$$

and hydrogen density

$$\langle n(H) \rangle = 5.7 \text{ cm}^{-3} \qquad (7-3)$$

for the period 1965 to 1967, which gives an average flux of 2.3×10^8 cm^{-2} sec^{-1}.

From this hydrogen flux and the average number density ratio He/H = 0.037 given by <u>Robbins et al.</u> (1970), we calculate an average helium flux of

$$\Phi(\text{He}^4) = 8.4 \times 10^6 \text{ cm}^{-2} \text{ sec}^{-1} \tag{7-4}$$

However, <u>Geiss et al.</u> (1970a) have measured He and Ne directly with the aluminum foil Solar Wind Composition experiment on Apollo 11 and 12 (see Table 1 in Chapter II) and an average of the two measurements gives

$$\Phi(\text{He}^4) = 7.2 \times 10^6 \text{ cm}^{-2} \text{ sec}^{-1} \tag{7-5}$$

and an abundance ratio

$$\frac{\text{He}^4}{\text{Ne}^{20}} = 525 \tag{7-6}$$

The helium-4 flux is quite close to the Vela result, which supports the assumption of this He^4 to Ne^{20} ratio approximates average solar wind conditions.

With these values we can now obtain the Ar^{36} flux using the Ne^{20}/Ar^{36} ratio. Table 12 gives ratios of elements

TABLE 12: Estimated and measured elemental ratios for the solar wind as deduced from various sources of information.

Source	He^4/Ne^{20}	Ne^{20}/Ar^{36}	He^4/Ar^{36}
Cosmic (Cameron-1968)	980	11	1.1×10^4
Lunar Fines (Heyman et al.-1970)	30-110	6-8	350-700
Lunar Ilmenite (Eberhardt et al.-1970)	(230)	≥ 33	≥ 7600
SWC Foil (Geiss et al.-1970a; Apollo 11 and 12 results have been averaged)	525		

in the solar wind as determined from several sources of in-
formation (some numbers are calculated from other data
presented by the author). The effects of diffusion can be
seen, for example, in the ratio of He^4/Ne^{20} for lunar fines,
ilmenite and the Solar Wind Composition foil. If the true,
average solar wind ratio were the same in all three cases,
then it appears that the ilmenite retains He^4 better than
the fines but the He^4/Ne^{20} ratio is still below that of the
foil where the time scale and temperature conditions should
prevent significant diffusion loss of He^4. The Ne^{20}/Ar^{36}
ratio was not detected by the foil but a value as large as
33 was obtained in the ilmenites. Since the ratio of these
heavier elements will not be as strongly affected by dif-
fusion, Eberhardt et al. (1970) assumed this to be a lower
limit to the true solar wind ratio. Using the average
He^4/Ne^{20} ratio of 525 determined by Geiss et al. (1970) and
the Ne^{20}/Ar^{36} ratio for ilmenites, we calculate

$$\frac{He^4}{Ar^{36}} = \frac{He^4}{Ne^{20}} \quad x \quad \frac{Ne^{20}}{Ar^{36}} \simeq 1.7 \times 10^4 \qquad (7-7)$$

(which is close to the value given by Cameron (1968) for
cosmic abundances – see Table 12). The corresponding Ar^{36}

flux is

$$\Phi(Ar^{36}) \simeq 4.2 \times 10^2 \ cm^{-2} \ sec^{-1} \qquad (7-8)$$

Ionization Lifetime of Argon-40

We now relate the Ar^{36} flux to that of Ar^{40} ions from the atmosphere. At height r above the sunlit lunar surface, the number of ions per cm^3 is given by the neutral number density divided by the ionization time r_i.

Charge Exchange:

From _Fite et al._ (1958) we obtain a charge exchange cross section for hydrogen on argon of

$$\sigma_{ex} = 10^{-15} \ cm^2 \qquad (7-9)$$

Using an approximate solar wind hydrogen flux of 2×10^8 $cm^{-2} \ sec^{-1}$, we obtain a probability of ionization per second of

$$\Lambda_{ex} = \sum N_H \cdot \sigma_{ex} = 2 \times 10^8 \times 10^{-15} = 0.2 \times 10^{-6} \qquad (7-10)$$

The charge exchange ionization by the high energy tail of the solar wind electron spectrum could also be considered and would give a small contribution to the rate.

Photoionization:

From <u>Samson</u> (1964) we see that the photoionization
cross section for argon is nearly constant at

$$\sigma_{ph} = 3.4 \times 10^{-17} \text{ cm}^2, \quad 380 \text{ Å} < \lambda < 789 \text{ Å} \qquad (7\text{-}11)$$

in the wavelength interval 380 to 780 Å and is very small
outside of this interval. Examination of the solar spectrum
in this region shows a differential solar flux which is
fairly constant at about

$$\langle \frac{d\Phi}{d\lambda} \rangle \simeq 3 \times 10^7 \text{ cm}^2 \text{ sec}^{-1} \text{ Å}^{-1} \qquad (7\text{-}12)$$

The probability of photoionization per second is

$$\Lambda_{ph} = \frac{d\Phi}{d\lambda} \sigma_{ph} \, d\lambda$$

$$\simeq \langle \frac{d\Phi}{d\lambda} \rangle \sigma_{ph} \, \Delta\lambda \qquad (7\text{-}13)$$

$$= 0.41 \times 10^{-6} \text{ sec}^{-1}$$

where $\Delta\lambda = 780 - 380 \text{ Å} = 400 \text{ Å}.$

Thus the net lifetime against ionization is the inverse
of the total ionization probability rate:

$$r_i = \frac{1}{\Lambda_{ex} + \Lambda_{ph}} \qquad (7\text{-}14)$$

or

$$r_i = 1.6 \times 10^6 \text{ sec} \qquad (7\text{-}15)$$

which is quite close to the rough estimate made by Manka and Michel (1971).

Neutral Ar^{40} Density and Partial Pressure

The number density of neutrals as a function of radial height in the lunar atmosphere is given by

$$n(r) = n_o \, e^{\frac{-r}{h}} \qquad (7\text{-}16)$$

Since the probability of ionization per second is given by $1/r_i$, then the radial ion distribution is

$$n_i(r) = \frac{n(r)}{r_i} = \frac{n_o}{r_i} \, e^{\frac{-r}{h}} \qquad (7\text{-}17)$$

However, in the time average case, $\bar{B}_{sw}$ lies in the ecliptic and the ion trajectories are nearly straight up along $\bar{E}_{sw}$. As shown in Figure 28, ions formed a height r above the surface travel a distance y in a vertical column before

Figure 28: Sketch of the vertical column from

which ions impact at the equator;

also shown is the number density

decreasing with altitude.
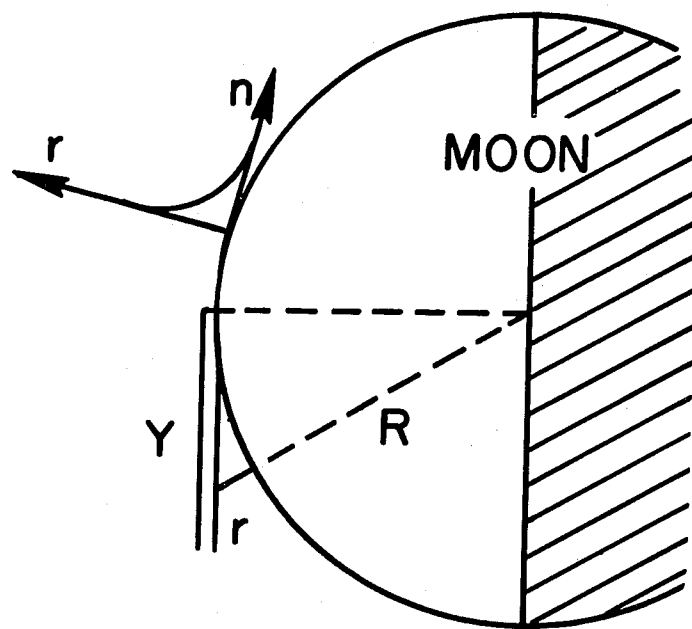
FIGURE 28

impacting the surface. If we look specifically at that column whose ions impact as the equator (where the Apollo 11, 12, and 14 samples were picked up), and if we assume straight-up trajectories (actually there is some deflection, see Table 6), then y is given by

$$y = (R + r) \sin \lambda \qquad (7\text{-}18)$$

which is well approximated by

$$y \simeq \sqrt{2\ r\ R} \qquad (7\text{-}19)$$

The integrated vertical column density is given by

$$N_i = \int_0^\infty \frac{n_o}{r_i}\ e^{\frac{-y^2}{2Rh}}\ dy \qquad (7\text{-}20)$$

but y is related to the impact energy $\mathcal{E}$ by

$$yE = \mathcal{E} \qquad (7\text{-}21)$$

so that the differential number formed per second is

$$n(\mathcal{E})d\mathcal{E} = \frac{n_o}{r_i E}\ e^{\frac{-\mathcal{E}^2}{2hRE^2}}\ d\mathcal{E} \qquad (7\text{-}22)$$

We now look at the flux of ions and the fraction trapped in the surface. In equilibrium, the flux of ions

to the surface equals the number formed per second in the
vertical column

$$\Phi = N_i = \int_0^\infty n(\mathcal{E})\ d\mathcal{E} \qquad (7\text{-}23)$$

so

$$\Phi(Ar^{40}) = \int_0^\infty \frac{n_o}{r_i E}\ e^{\frac{-\mathcal{E}^2}{2hRE^2}}\ d\mathcal{E} = \frac{n_o}{r_i}\ \sqrt{\frac{\pi\,Rh}{2}} \qquad (7\text{-}24)$$

$$= \frac{n_o h}{r_i}\ \sqrt{\frac{\pi\,R}{2h}} = \frac{n_o h}{r_i}\ 7.4 \qquad (7\text{-}25)$$

The number trapped per cm^2 second is given by (5-13)

$$N_{it} = \int \eta_t(\mathcal{E})\ n(\mathcal{E})\ d\mathcal{E} \qquad (7\text{-}26)$$

and from the numerical integration described in Chapter V,
part C, we get that for Ar^{40}, the fraction trapped is

$$t(40) = \frac{N_{it}}{N_i} \approx 0.33 \qquad (7\text{-}27)$$

i.e., that 33% of the Ar^{40} impacting at the equator is
trapped. The solar wind Ar^{36} at $\sim$36 keV is essentially

100% trapped.

$$t(36) \simeq 1.0 \qquad\qquad (7-28)$$

The lunar sample measurements give equal amounts of Ar^{40} and Ar^{36}

$$\frac{N_{it}(40)}{N_{it}(36)} \simeq 1 \qquad\qquad (7-29)$$

Further, some geometrical factor should be included since the Ar^{36} impacts normal at least at the subsolar point, to the equatorial lunar surface while the Ar^{40} always impacts at an oblique angle, and thus the one cm^2 vertical column is spread over a greater area on the surface. This effect is somewhat reduced by fluctuations in the orientation of $\bar{B}_{sw}$, but a geometrical factor of at least two is appropriate.

Thus the neutral number density of Ar^{40} in the atmosphere at the lunar surface is given by

$$n_o(Ar^{40}) = \frac{r_i}{7.4h} \; \Phi(36) \; \times \; \frac{t(36)}{t(40)} \; \times \; (\text{geom. factor})$$

$$(7-30)$$

or $\qquad\quad n_o(Ar^{40}) = 1.1 \times 10^2 \; cm^{-3}$

The corresponding partial pressure of Ar^{40} near the subsolar point can readily be calculated. Assuming $T = 400 \, ^{\circ}K$, the partial pressure of Ar^{40} is

$$P(Ar^{40}) = 0.46 \times 10^{-14} \, mm \, Hg$$

or   (7-31)

$$P(Ar^{40}) \simeq 0.5 \times 10^{-14} \, torr$$

Ar^{40} Ion Flux

We can also estimate the flux of Ar^{40} ions striking the surface. From equation (7-25), the flux along the vertical column (oblique incidence at the equator)

$$\Phi(Ar^{40}) = \frac{7.4h \, n_o}{r_i} \qquad \text{(oblique incidence)} \quad (7-32)$$

$$\Phi(Ar^{40}) = 2.3 \times 10^3 \, cm^{-2} \, sec^{-1} \qquad (7-35)$$

where the area is at right angles to the vertical column; for the lunar surface the value should be divided by the geometrical factor of at least two.

When $\bar{B}_{sw}$ rotates normal to the ecliptic plane so that ions can be driven straight in normal to the lunar equator,

then the flux is

$$\Phi = \frac{n_o h}{r_i} \qquad \text{(normal incidence)} \qquad (7\text{-}34)$$

so that

$$\Phi(Ar^{40}) = 3 \times 10^2 \text{ cm}^{-2} \text{ sec}^{-1} \qquad (7\text{-}35)$$

which is the Ar^{40} flux that should be detected by the SIDE

and is in the vicinity of the minimum detectable signal for

the instrument. However, as shown in part B of this chapter,

other species are expected to be more prevalent and thus

detectable.

Comments

It should be noted that this approach to calculating

$n_o(Ar^{40})$ is essentially an indirect measurement utilizing

lunar samples as the sensor. The approximate values ob-

tained here agree roughly with previous estimates by

Bernstein et al. (1964) and Hinton and Taeusch (1964) who

get about 10^3 to 10^4 cm^{-3}. The variation could be due to

different assumptions in the calculations, could imply that

the outgassing of Ar^{40} from the moon is lower than assumed

in the calculations, or the rate of removal of ions from the atmosphere by the acceleration mechanism described here could be more rapid than the mechanisms assumed in some calculations. It should also be noted that these results are for an average over geologic time and the present amount of Ar^{40} in the lunar atmosphere could be changed due to the decay of K^{40} and decreased outgassing, change in solar wind parameters, etc., as was discussed in Chapter V.

However, it should also be noted the density and partial pressure of Ar^{40}, as calculated here, are not unreasonable. Since the total pressure detected by the CCGE (and from our calculations using SIDE data in the next section) is 10^{-12} to 10^{-11} torr, then from the standpoint of most lunar atmosphere models, an Ar^{40} partial pressure of 10^{-14} torr is reasonable. Furthermore, the total mass of the atmosphere Ar^{40} at this pressure can be estimated to be

$$M(Ar^{40}) \approx m(Ar^{40}) \, n_o h \times 4\pi R_m^2 \qquad (7\text{-}36)$$

or

$$M(Ar^{40}) \approx 13 \text{ Kg} \qquad (7\text{-}37)$$

which is not an extremely large amount.

B.   Density of the Neutral Lunar Atmosphere Calculated

      from the Acceleration Model and Ion Detector Data

On the basis of the acceleration model developed in

Chapter IV, the detailed study of the sunrise/sunset events

7 and 10 in Chapter VI, and the atmosphere calculations in

part A of this chapter we are able to calculate the total

ionosphere flux as seen by the SIDE and the total neutral

number density of the sunrise/sunset lunar atmosphere. The

only assumptions involved are an exponential atmosphere

and an average ionization lifetime. Both of these are

reasonably accurate so that by using the acceleration model,

and ion detector data for selected events, then the second

reported direct measurement of lunar atmosphere density is

thereby made (the first being by the CCGE, Johnson et al.,

1972a,b).

For events 7 and 10, $\bar{B}_{sw}$ is approximately perpendicu-

lar to the ecliptic while $\bar{E}_{sw}$ lies nearly in the ecliptic

so that ions are driven straight in radially and the approp-

riate flux - density relation is from equation (7-34)

$$\Phi = \frac{N}{r_i} = \frac{n_o h}{r_i} \qquad\qquad (7\text{-}38)$$

The total ionization time for a number of species, such as argon and water is

$$r_i = 2 \times 10^6 \text{ sec} \qquad (7\text{-}39)$$

and from some estimates made by <u>Bernstein et al.</u>, (1963) we get for neon

$$r_i = (Ne) - 6 \times 10^6 \text{ sec} \qquad (7\text{-}40)$$

We shall calculate the density using the average time r_i and also specifically for neon.

To calculate the scale height, we assume an average mass 20 (neon) and the appropriate temperatures

Sunrise: $T \approx 100\ ^{\circ}K$, $h = 25$ km

Sunset : $T \approx 225\ ^{\circ}K$, $h = 56$ km

Sunrise

The sunrise ion event, 10, showed "isotropic" flux peaks of 1.8×10^7 ions cm^{-2} sec^{-1} $ster^{-1}$ which, as shown earlier, should be converted to directional flux by equation (2-5)

$$\Phi = Flux_{isotropic} \times 0.0086 \text{ ster.}$$

$$\qquad (7\text{-}41)$$

$$= 1.54 \times 10^5 \text{ ions } cm^{-2} \text{ sec}^{-1}$$

Thus, using the average ionization lifetime of $\tau_i = 2 \times 10^6$ sec we calculate

$$n_o = \frac{\Phi \, \tau_i}{h} = 1.2 \times 10^5 \; cm^{-3} \qquad (7\text{-}42)$$

and specifically for the neon lifetime

$$n_o = 3.7 \times 10^5 \; cm^{-3} \qquad (7\text{-}43)$$

both of which agree very well with the sunrise density of $2 \times 10^5 \; cm^{-3}$ from the CCGE reported by Johnson et al. (1972a) at the Third Lunar Science Conference.

The sunrise pressure, using the density given by equation (7-42) is

$$\begin{aligned} P &= 1.5 \times 10^{-15} \; atm \\ &= 1.2 \times 10^{-12} \; torr \end{aligned} \qquad (7\text{-}44)$$

Additional insight can be gained, and a check on an assumption made, by looking at the scale height for this event predicted by the acceleration model. From the Ames magnetometer data for this event shown in Figure 25, the

component of $\bar{B}_{sw}$ perpendicular to $\bar{V}_{sw}$ is

$$B_{\perp} \simeq 15 \text{ gamma}$$

and from preliminary SWS data (C. Snyder, personal communication

$$V_{sw} \simeq 310 \text{ km sec}^{-1}$$

so that

$$E_{sw} = 4.5 \text{ volts km}^{-1} \tag{7-45}$$

and since the peak in the count spectrum occurs at 100 eV and

$$\mathcal{E} = h \, E \tag{7-46}$$

then we calculate

$$h \simeq 22 \text{ km} \tag{7-47}$$

which agrees very well with the 25 km calculated in this section.

Sunset

The sunset event, 7, also shows peak "isotropic" fluxes of 1.7×10^7 ions cm^{-2} sec^{-1} $ster^{-1}$ which converts to the directional flux

$$\Phi = 1.5 \times 10^5 \text{ ions } cm^{-2} \text{ } sec^{-1} \tag{7-48}$$

and using the average lifetime $\tau_i = 2 \times 10^6$ sec, we get

$$n_o = 5.2 \times 10^4 \text{ } cm^{-3} \tag{7-49}$$

and specifically for the neon lifetime,

$$n_o = 1.5 \times 10^5 \text{ } cm^{-3} \tag{7-50}$$

both of which again agree well with the CCGE sunset density of about 2×10^5 cm^{-3} reported by Johnson et al. (1972a).

The density in equation (7-49), while only one third of that in equation (7-42), again gives the pressure

$$P_{ss} = 1.5 \times 10^{-15} \text{ atm}$$
$$= 1.2 \times 10^{-12} \text{ torr} \tag{7-51}$$

due to the different temperature. Thus it appears that the temperature and density may vary so as to keep the pressure fairly constant.

It should also be noted that using the Event 7 magnetometer data and preliminary SWS data (C. Snyder, personal communication) that

$$B_\perp \approx 10 \text{ gamma}$$

$$V_{sw} \approx 330 \text{ km sec}^{-1}$$

so that

$$E_{sw} = 3.3 \text{ volts km}^{-1} \qquad (7-52)$$

and since the energy of peak flux in Figure 24 occurs at 250 eV, then the scale height is expected to be

$$h \approx 83 \text{ km} \qquad (7-53)$$

which agrees fairly well with the calculated value of 56 km. Furthermore, if the calculated lunar surface terminator potential of -40 volts is subtracted from the ion energy, then the expected scale height is 64 km which agrees very well with the calculated value. Also, the measured scale height is likely to exceed one calculated from the local surface temperature since there is a flux of hotter, high

altitude neutrals from the sunlit to the dark side (Yeh and

Chang, 1972).

Thus, using the acceleration and atmosphere models, we

have a useful technique for converting selected ion flux

measurements into measurements of the neutral lunar atmos-

phere density and pressure, and apparently with reasonable

accuracy.

VIII.

SUMMARY AND CONCLUSIONS

A.   Results Contained in the Thesis

The lunar atmosphere is a relatively simple exospheric

planetary atmosphere and is closely related to its iono-

sphere. In this thesis we have developed a model for the

dynamics of the lunar ionosphere based on an acceleration

model for the interaction of ions with electric and magnetic

fields in the solar wind and at the lunar surface; in some

of the calculations an exponential atmosphere is assumed.

The expected characteristics of the dynamics of the iono-

sphere have been predicted, ion and magnetic data in support

of these predictions have been shown, and interpretations

of other ion events have been made. We have also related

this ionospheric model to the atmospheric composition,

neutral density and trapping in the lunar surface.

In particular we have found:

1.   Ion fluxes from the ambient lunar atmosphere should be

    strongly correlated with $\bar{B}_{sw}$, be at right angles to

    $\bar{V}_{sw}$, and be relatively energetic (tens to thousands of

    electron volts) compared to the terrestrial ionosphere.

Thus the previous assumption of an ionosphere with 400 $^{\circ}$K temperature is greatly in error.

2.   When the moon is in the solar wind, the lunar surface potential is likely to be a few volts positive over much of the sunlit face and about 40 volts negative at the terminator. Potentials on the dark side may significantly affect the ion dynamics there.

3.   Atmospheric ions formed over about half of the sunlit face of the moon are lost due to the acceleration by electric and magnetic fields in the solar wind. This is the dominant loss mechanism and occurs in the atmosphere over a significant portion of the sunar surface and not only at the terminator.

4.   The assumed relationship between neutral and ionized species, which had been used to deduce the atmospheric density from radio frequency refraction experiments, is not correct. The reason is that ionized atmosphere is immediately accelerated into the surface or away from the moon.

5.   As predicted, detailed correlations between the direction of measured ion fluxes and the orientation of $\bar{B}_{sw}$ have been found for two sunrise/sunset events.

Other events which do not show the same behavior are discussed. Basically, these uncorrelated events differ in other ways as well, such as different energy spectra, and some of these ions may arise from sources other than the ambient lunar atmosphere.

6. Ions accelerated from the lunar atmosphere can be trapped in the lunar surface. In particular we have found that the lunar atmosphere can account for the anomalous Ar^{40} in surface samples with about 8.5% of the lunar atmosphere Ar^{40} being trapped in the surface. It was also found that release of accreted solar wind into the atmosphere and subsequent retrapping via the acceleration mechanism can cause a mass-dependent isotopic fractionation of these solar wind elements, which is approximately inversely proportional to the isotope mass.

7. On the basis of these trapping calculations, and lunar sample data, the density of neutral Ar^{40} in the lunar atmosphere is estimated to be about 1×10^2 cm^{-3}.

8. It is also likely that the observation of ions from lunar impact or venting events can partly or wholly explained by the acceleration mechanism. The sporadic

detection of these events may be related to fluctua-

tions in $\bar{B}_{sw}$, just as it sometimes is for ions from the

ambient lunar atmosphere. The questions about this

interpretation if impact events, raised by Freeman et

al. (1971a,b) are not necessarily conclusive since the

formation of a neutral cloud downstream from the ion

detector does not restrict the ability of ions to enter

the detector. Also the fact that ions quickly pick

up a component of motion in the direction of solar wind

flow is not a determining factor since the only rele-

vant portion of the trajectories is the initial portion

where the velocities are approximately perpendicular

to solar wind flow (i.e., the ions do not really quickly

pick up a component of motion in the solar wind direction,

at least not compared to the short time it takes them

to reach the lunar surface). Neither is the high ion

flux, observed for some events, contradictory to the

model.

9. When the ions associated with the "water event" are in-

terpreted in light of the acceleration model, and if

$\bar{E}_{sw}$ is assumed to be the only energy source for the

ions, then the ions are found to originate at heights

of 16 to 32 km, and well below the CSM orbit (~ 100 km).
The latter point is significant since debris left be-
hind by the CSM has been indicated as a possible source
for the "water events".

10. The predicted energy spectrum of lunar ions detected
at the lunar surface is calculated and shown to compare
well with the measured spectrum of a clearly defined
"ionospheric" ion event detected by the SIDE. Further-
more, from this spectrum the scale height of the
associated atmosphere is calculated.

11. Finally, using the acceleration model and assuming an
exponential atmosphere, and using ion fluxes measured
by the SIDE, the total number density of the neutral
lunar atmosphere at sunrise and sunset is calculated to
be about 2×10^5 cm^{-3}, in excellent agreement with the
CCGE pressure measurement. This conversion of ion
data into neutral pressure by use of the acceleration
model thus gives the second direct measurement of the
lunar atmosphere density. The pressure corresponding
to the quoted density is about 1×10^{-12} torr.

B.   <u>Limitations and Future Work</u>

The limitations of this work can be summarized in two

areas; in some cases physical parameters need to be better

known, and in other cases we do not completely understand

all of the data in hand.   Examples of parameters which need

to be better known are: the mass of the atmospheric species

being detected (though neon is likely for the sunrise/sunset

events), the height distribution in the atmosphere (the ex-

ponential atmosphere is a good approximation for our purposes,

however, the kinetic solution at the terminator shows fluxes

of high altitude atoms from the sunlit to dark sides of the

moon), and because of some uncertainty in which species are

being detected, there is some uncertainty in the effective

ionization lifetime.   However, these errors are relatively

small, introducing uncertainties of perhaps a factor of two,

so that the resulting calculations of properties such as

neutral density may have errors that are not much greater

than those inherent in the SIDE and CCGE experiments.

Good examples of data which are not yet understood are

those ion events having only monoenergetic spectra, and which

are detected when $\bar{E}_{sw}$ is not directly into the SIDE.

Future work might include looking more carefully at

these unusual ion events and relating them to surface fields,
or the presence of the earth's bow shock. Another fruitful
area of research will be to further study properties of the
lunar atmosphere such as source and loss rates, using the
acceleration model developed here, and to make a more de-
tailed estimate of the composition of the lunar atmosphere.
Also, the study of the effect of the lunar atmosphere, on
the abundances of solar gases trapped in the lunar surface,
has really just begun.

As a consequence of our studies of the lunar atmosphere
and the acceleration of lunar ions, we have suggested an ex-
periment designed to detect a few significant atmospheric
species. The concept (F. C. Michel, personal communication)
is to trap accelerated ions from the lunar atmosphere, in
the same way that solar wind ions are trapped in an aluminum
foil by the Solar Wind Composition experiment (Geiss et al.,
1970b). Since the average direction of the atmospheric ion
velocity is either up or down at right angles to the ecliptic
plane, then the atmosphere detection foil should be placed
parallel to the plane of the ecliptic. In this orientation,
the atmosphere foil will have minimum accretion of solar
wind; however, it is desirable to shield the foil from the

solar wind. One possible way to deploy such an atmospheric foil would be as a second foil, in the shaded region behind a solar wind foil (J. Geiss, personal communication). The analysis of the returned atmosphere foil would be directed toward the detection of the most likely atmospheric noble gases. Our calculations indicate, using the results of Chapter VII, that there is likely to be a measurable amount of Ne^{20} trapped in the foil, and possibly a measurable amount of Ar^{40} or Ne^{22} if special techniques are used. It may be noted that the moon may occult part of the ionospheric flux to the foil, depending on the orientation of $\bar{B}_{sw}$ during the exposure period. However, the reasonably high probability of success and the relatively simple nature of the measurement argue strongly for the experiment to be included on Apollo 17. The measurement of just one atmospheric component would be of great value in continuing the calculations of this thesis, would assist scientists who are interpreting lunar sample gases, and would significantly extend our knowledge of the lunar atmosphere.

APPENDIX

PLASMA EQUATIONS FOR POTENTIAL CALCILATION

This appendix summarizes the probe equations for currents to a surface. The equations and approximations are the appropriate ones for calculating the potential of a body the size of the moon in the type of plasma environments encountered in the lunar orbit. The physical interpretation of the equations and the results obtained from them are discussed in Chapter III.

The equations for a body in a stationary thermal plasma follow the work of Whipple (1964) and Fahleson (1967) but with added terms for secondary electron emission.

The equations for a body in a flowing as well as thermal plasma are based on the plasma equation developed by Whipple (1959). The flow and thermal contributions to the current are interrelated but the equations reduce to the static plasma equations when the flow velocity goes to zero and to the pure flow equations when the thermal velocity goes to zero. When the potential is positive, the Repelled Species is the plasma ion and the Attracted Species is the plasma electron.

In the equations, ϕ is the local potential of the moon with respect to the adjacent plasma potential, and I_e, I_i, I_p and I_s are the local currents <u>to</u> the lunar surface from the plasma electrons and ions and from the surface photo- and secondary currents respectively. In the stationary plasma equations, k is the Boltzmann constant, m_e and m_i are the electron and ion masses, Te and Ti are the electron and ion temperatures, t is the plasma sheath thickness and a is the radius of the moon, λ is the Debye length, ϵ is the effective photo emissivity of the surface, n is the external plasma electron (or ion) density, e is the magnitude of the electron charge, T_p and T_s are the photo- and secondary electron temperatures, and δ_e and δ_i are the secondary electron coefficients for primary electrons and ions respectively.

In the equations for a flowing plasma, V is the flow velocity, v_{mi} and v_{me} are the mean ion and electron thermal velocities, θ is the angle from the subsolar point, and the functions U and X are defined in the equations as functions of the other variables.

POTENTIAL DETERMINED BY BALANCE OF CURRENT DENSITY

$$I_e + I_i + I_p + I_s = 0$$

A. FOR STATIONARY PLASMA, POSITIVE POTENTIAL ($\phi > 0$):

REPELLED: $\quad I_i = ne\sqrt{\frac{kT_i}{2\pi m_i}}\ \exp\left(\frac{-e\phi}{kT_i}\right)$

ATTRACTED: $\quad I_e = -ne\sqrt{\frac{kT_e}{2\pi m_e}}\ \frac{a^2}{r^2}\left[1 - \frac{a^2-r^2}{a^2}\ \exp\left(\frac{-r^2}{a^2-r^2}\ \frac{e\phi}{kT_e}\right)\right]$

$$\cong -ne\sqrt{\frac{kT_e}{2\pi m_e}}\left[1 + \frac{2t}{r}\right],\quad \text{THIN SHEATH}$$

$$\cong -ne\sqrt{\frac{kT_e}{2\pi m_e}},\quad \text{VERY THIN SHEATH}$$

WHERE $a = r + t$, $\ t = \lambda\, 0.83\left(\frac{r}{\lambda}\right)^{1/3}\left(\frac{e\phi}{kT_e}\right)^{1/2}$, $\quad \lambda = 6.9\times10^{-2}\sqrt{\frac{T}{n}}$ meters

EMITTED: $I_p = i_p(\epsilon) \cos\theta \exp\left(\dfrac{-e\phi}{kT_p}\right)$

$I_s = (I_e \delta_e + I_i \delta_i) \exp\left(\dfrac{-e\phi}{kT_s}\right)$

B. FOR STATIONARY PLASMA, NEGATIVE POTENTIAL, ($\phi < 0$):

REPELLED: $I_e = -ne\sqrt{\dfrac{kT_e}{2\pi m_e}}\ \exp\left(\dfrac{e\phi}{kT_e}\right)$

ATTRACTED: $I_i \cong ne\sqrt{\dfrac{kT_i}{2\pi m_i}} = \dfrac{nev_{ti}}{4} = \dfrac{nev_{mi}}{2\sqrt{\pi}}$

EMITTED: $I_p = i_p \cos\theta$

$I_s = I_e \delta_e + I_i \delta_i$

C. FOR FLOWING PLASMA, POSITIVE POTENTIAL ($\phi > 0$)

REPELLED: $I_i = \dfrac{ne\,V\cos}{2}\left[1 + \mathrm{erf}(X) + \dfrac{v_{mi}}{V\cos\theta\,\sqrt{\pi}}\;e^{-X^2}\right]$

$\qquad = \dfrac{ne\,v_{mi}}{2\sqrt{\pi}}\cdot\left[e^{-X^2} + \dfrac{V\cos\theta\,\sqrt{\pi}}{v_{mi}}\left(1 + \mathrm{erf}(X)\right)\right]$

$\qquad \sim ne\,V\cos\theta$

WHERE $\quad X = \dfrac{V\cos\theta}{v_m} - \sqrt{\dfrac{e\phi}{kT}} = U - \sqrt{\dfrac{e\phi}{kT}}$

ATTRACTED: $\quad I_e = \dfrac{ne\,v_{me}}{2\sqrt{\pi}}\left[e^{-U_e^{\,2}} + \sqrt{\pi}\;U_e\left(1 + \mathrm{erf}\,(U_e)\right)\right]$

$\qquad\qquad \cong \dfrac{ne\,v_{me}}{2\sqrt{\pi}}\left[1 + \sqrt{\pi}\;U_e\right]$

EMITTED: $\quad I_p = i_p\,\cos\theta\,\exp\left(\dfrac{-e\,\phi}{kT_p}\right),\quad I_s = I_e\,\delta_e\,\exp\left(\dfrac{-e\,\phi}{kT_s}\right)$

D. FOR FLOWING PLASMA, NEGATIVE POTENTIAL ($\phi < 0$)

REPELLED: $\quad I_e = \dfrac{-nev_{me}}{2\sqrt{\pi}}\left[e^{-X^2} + \dfrac{V\cos\theta}{v_{me}}\sqrt{\pi}\left(1+\text{erf}(X)\right)\right]$

$$\sim \dfrac{-nev_{me}}{2\sqrt{\pi}}\, e^{\frac{-e|\phi|}{kT_e}}$$

WHERE: $\quad X_e = \dfrac{V\cos\theta}{v_{me}} - \sqrt{\dfrac{e|\phi|}{kT}} = U_e - \sqrt{\dfrac{e|\phi|}{kT}}$

ATTRACTED: $\quad I_i = \dfrac{neV\cos\theta}{2}\left[1 + \text{erf}(U) + \dfrac{1}{U}\dfrac{1}{\sqrt{\pi}}e^{-U^2}\right]$

$$\sim neV\cos\theta$$

EMITTED: $\quad I_p = i_p\cos \quad , \quad I_s = I_e\,\delta_e$

ACKNOWLEDGEMENTS

computer analysis. I am grateful to friends at NASA, Drs.

Jerry Modisette, Stan Freden, and Dallas Evans, for sup-

port of my graduate program.

It is a pleasure to thank my advisor, Professor Michel,

for his guidance and example; his suggestions have been

a great help during the course of this work.

Finally, I thank my parents, who have encouraged me

in this effort.

BIBLIOGRAPHY

Anderson, H.R. and R.H. Manka, Electric fields at the lunar
    surface - sources and methods of measurement, paper pre-
    sented at the NASA Ames Conference on Electromagnetic
    Exploration of the Moon, Moffett Field, California,
    June 1968.

Anderson, H.R. and R.H. Manka, Electric fields at the lunar
    surface, sources and methods of measurement, in Electro-
    magnetic Exploration of the Moon, Ed. by W.I. Linlor,
    p117, Mono, Baltimore, 1970.

Axford, W.I., Observations of the interplanetary plasma, Space
    Sci. Rev., 8, 331, 1968.

Bame, S.J., J.R. Asbridge, H.E. Felthauser, E.W. Hones, and
    I.B. Strong, Characteristics of the plasma sheet in the
    earth's magnetotail, J. Geophys. Res., 72, 113, 1967.

Bame, S.J., Plasma sheet and adjacent regions, in Earth's
    Particles and Fields, edited by Billy M. McCormac, p.373,
    Rinehold, New York, 1968.

Baur, H., U. Frick, H. Funk, L. Schultz, and P. Signer, On
    the question of retrapped 40-Ar in lunar fines, (abstract),
    in Lunar Science III, Ed. by C. Watkins, Abstracts of the
    Third Lunar Science Conference, p.47, Lunar Science Institute
    Contribution No.88, 1972.

Bernstein, W., R.W. Fredricks, J.L. Vogl, and W.A. Fowler,
    The lunar atmosphere and the solar wind, Icarus, 2, 233,
    1963.

Bühler, F., J. Geiss, J. Meister, P. Eberhardt, J.C. Huneke,
    and P. Signer, Trapping probability of the solar wind in
    solids: part I. trapping probability of low energy He,
    Ne, and Ar ions, Earth and Planet. Sci. Letters, 1, 249,
    1966.

Burlaga, L.F. and N.F. Ness, Macro-and micro-structure of the
    interplanetary magnetic field, Can, J. Phys. 46, S962,
    1968.

Cloutier, P.A., M.B. McElroy, and F.C. Michel, Modification
    of the Martian ionosphere by the solar wind, J. Geophys.
    Res., 74, 6215, 1969.

Colburn, D.S., R.G. Currie, J.D. Mihalov, and C.P. Sonett, Diamagnetic cavity discovered behind moon, Science, 158, 1040, 1967.

Colburn, D.S., J.D. Mihalov, and C.P. Sonett, Magnetic observations of the lunar cavity, J. Geophys. Res., 76, 2940, 1971.

Dessler, A.J., Solar wind and interplanetary magnetic field, Rev. Geophys., 51, 1, 1967.

Dollfus, A., Polarization of light scattered by solid bodies and natural clouds, Annales d'Astrophysique, 19, 83, 1956.

Dyal, P. and C.W. Parkin, Electrical conductivity and temperature of the lunar interior from magnetic transient-response measurements, J. Geophys Res., 76, 5947, 1971a.

Dyal, P., C.W. Parkin, and P. Cassen, Surface magnetometer experiments: Internal lunar properties and lunar field interactions with the solar plasma, To be published in the Proceedings of the Third Lunar Science Conference, Houston, January 10-13, 1972.

Dyal, P., C.W. Parkin and C.P. Sonett, Lunar surface magnetometer experiment, In Apollo 12 Preliminary Science Report, NASA SP-235, 55, 1970a.

Dyal, P., C.W. Parkin and C.P. Sonett, Apollo 12 magnetometer: Measurement of a steady magnetic field on the surface of the moon, Science, 196, 762, 1970b.

Dyal, P., C.W. Parkin, C.P. Sonett, R.L. Dubois, and G. Simmons, Lunar portable magnetometer experiment, In Apollo 14 Preliminary Science Report, NASA SP-272, 227, 1971b.

Eberhardt, P., J. Geiss, H. Graf, N. Grögler, U. Krähenbühl, H. Schwaller, J. Schwarzmüller, and A. Stettler, Trapped solar wind noble gases, exposure age and K/Ar-age in Apollo 11 lunar fine material, Proc. Apollo 11 Lunar Sci. Conf., Geochim. Cosmochim. Acta Suppl. 1, Vol 2, 1037, 1970.

Elsmore, B., Radio observations of the lunar atmosphere, Phil. Mag., Ser. B, 2, 1040, 1957.

Fahleson, U., Theory of electric field measurements conducted in the magnetosphere with electric probes, Space Sci. Rev., 7, 238, 1967.

Fite, W.L., R.T. Brackmann and W.R. Snow, Charge exchange in proton-hydrogen atom collisions, Phys. Rev., 112, 1161, 1958.

Freeman, J.W. Jr., Energetic ion bursts on the nightside of the moon, J. Geophys. Res., 77, 239, 1972.

Freeman, J.W. Jr., M.A. Fenner, H.K. Hills, K.A. Linderman, R. Medrano, and J. Meister, Suprathermal Ions near the moon, Presented at XVth General Assembly of the International Union of Geophysics and Geodesy Moscow, August 1971a.

Freeman, J.W., H.K. Hills and M.A. Fenner, Some results from the Apollo 12 suprathermal ion detector, Proc. Second Lunar Sci, Conf., Geochim, Cosmochim, Acta, Suppl. 2, Vol. 3, 2093, MIT Press, 1971b.

Freeman, J.W., Jr., H.K. Hills and R.R. Vondrak, Water Vapor, whence comest thou? (abstract), Lunar Science III, Ed. by C. Watkins Abstracts of the Third Lunar Science Conference, p. 283, Lunar Science Institute Contribution No. 88, 1972a.

Freeman, J.W. Jr., H.K. Hills, and R.R. Vondrak, Water Vapor, whence comest thou? Submitted to the Proceedings of the Third Lunar Science Conference, Houston, January 10-13, 1972b.

Funkhouser, J.G., O.A. Schaeffer, D.D. Bogard, and J. Zahringer, Gas analysis of the lunar surface, Science, 167, 561, 1970.

Geiss, J., P. Eberhardt, F. Bühler and J. Meister, Apollo 11 and Apollo 12 solar wind composition experiments: Fluxes of He and Ne isotopes, J. Geophys. Res., 75, 5972, 1970a.

Geiss, J., P. Eberhardt, P. Signer, F. Bühler, and J. Meister, The solar-wind composition experiment, In Apollo 12 Preliminary Science Report, NASA Sp-235, 99, 1970b.

Grobman, W.D. and J.L. Blank, Electrostatic potential distribution of the sunlit lunar surface, J. Geophys. Res., 74, 3943, 1969.

Hall, F.G., The dynamic structure of the lunar atmosphere, M.S. Thesis, University of Houston, Houston, Texas, 1968.

Hazard, C., M. B. Mackey, and A.J. Shimmins, Investigation of the radio source 3C 273 by the method of lunar occultations Nature, 198, 1037, 1963.

Heymann, D., A. Yaniv, J.A.S. Adams, and G.E. Fryer, Inert gases in lunar samples, Science, 167, 555, 1970.

Heymann, D. and A. Yaniv, Ar^{40} anomally in lunar samples from Apollo 11, Proc. Second Lunar Sci. Conf., Geochim. Cosmochim. Acta, Suppl. 1, Vol. 2, 1261, Pergamon, 1970.

Heymann, D., A. Yaniv, and J. Walton, Inert gases in Apollo 14 fines and the case of Parentless Ar^{40} (abstract), in Lunar Science III, Ed. by C. Watkins, Abstracts of the Third Lunar Science Conference, 376, Lunar Science institute Contribution No. 88, 1972.

Hinteregger, H.E., K.R. Damon, and L.A. Hall, Analysis of photoelectrons from solar extreme ultraviolet, J. Geophys. Res., 64, 961, 1959.

Hinton, F.L. and D.R. Taeusch, Variation of the lunar atmosphere with the strength of the solar wind, J. Geophys. Res., 69, 1341, 1964.

Johnson, F.S., Lunar atmosphere, Rev. Geophys. Space Phy., 9, 813, 1971.

Johnson, F.S., D.E. Evans, and J.M. Carroll, Cold-cathode gauge experiment (lunar atmosphere detector), In Apollo 14 Preliminary Science Report, NASA SP-272, 185, 1971.

Johnson, F.S., D.E. Evans, and J. Carroll, Lunar atmosphere, presented at the Third Lunar Science Conference, January 10-13 Houston, 1972a.

Johnson, F.S., D.E. Evans, and J. Carroll, Lunar atmosphere (abstract), in Lunar Science III, Ed. by C. Watkins, Lunar Science Institute Contribution No. 88, p.436, 1972b.

Kirsten, T., F. Steinbrunn, and J. zähringer, Location and variation of trapped rare gases in Apollo 12 lunar samples, Proc. Second Lunar Sci. Conf., Geochim. Cosmochim. Acta, Suppl. 2, Vol. 2, 1651, MIT Press, 1971.

Kornelesen, E.V., The ionic extrapment and thermal desorption of inert gases in tungsten for kinetic energies of 40 ev to 5 kev., Can. J. Phys., 42, 364, 1964.

Langmuir, I. and H. M. Mott-Smith, The theory of collectors in gaseous discharges, Phys. Rev., 28, 727, 1926.

Lazarus, A. J., G. L. Siscoe, and N. F. Ness, Plasma and

magnetic field observations during the magnetosphere passage of Pioneer 7, *J. Geophys. Res.*, 73, 2399, 1968.

Lindeman, R.A., Recurring ion events at the lunar surface, M.A. Thesis, Rice University, Houston, Texas, 1971.

Manka, R.H. and H.R. Anderson, The lunar surface electric field (abstract), *Trans. Am. Geophys. Union*, 49, 227, 1968.

Manka, R.H. and H.R. Anderson, Lunar surface plasma environment and electric potential, *Trans. Am Geophys. Union*, 50, 217, 1969.

Manka, R.H. and F.C. Michel, Energy and Flux of ions at the lunar surface (abstract), *Trans. Am. Geophys. Union*, 51, 408, 1970a.

Manka, R.H. and F.C. Michel, Lunar atmosphere as a source of Ar^{40} and other lunar surface elements (abstract), *Trans. Am. Geophys. Union*, 51, 344, 1970b.

Manka, R.H. and F.C. Michel, Lunar atmosphere as a source of argon-40 and other lunar surface elements. *Science*, 169, 278, 1970c.

Manka, R.H. and F.C. Michel, Lunar atmosphere as a source of lunar surface elements, *Proc. Second Lunar Science Conf. Geochim. Cosmochim. Acta*, *Suppl. 2*, *Vol. 2*, 1717 MIT Press, 1971.

Manka, R.H., F.C. Michel, J.W. Freeman, Jr., P. Dyal, C.W. Parkin, D.S. Colburn, and C.P. Sonett, Evidence for acceleration of lunar ions, (abstract), in *Lunar Science III*, Edited by C. Watkins, Abstracts of the Third Lunar Science Conference, p. 504, Lunar Science Institute Contribution No. 88, 1972.

Marti, K., G.W. Lugmair, and H.C. Urey, Solar wind gases, cosmic ray spallation products, and the irradiation history, *Science*, 167, 548, 1970.

McDaniel, E.W., *Collision Phenomena in Ionized Gases*, 775 pp., John Wiley and Sons, New York, 1964.

Meister, J., Ein Experiment zur Bertimmung der Zusammenstezung and Isotopenverhaeltnisse des Sonnenwindes: Einfangverhalten von Aluminium für niederenergetische Edelgasionen, Ph.D. Thesis, University of Berne, 1969.

Michel, F.C., Interaction between the solar wind and the lunar atmosphere, Planet. Spa. Sci., 12, 1075, 1964.

Ness, N.F., Lunar Explorer 35, Goddard Preprint X-616-68-166, Presented at XIth COSPAR, Tokyo, May, 1968.

Ness, N.F., K.W. Behannon, C.S. Scearce, and S.C. Cantarano, Early results from the magnetic field experiment on lunar Explorer 35, J. Geophys. Res., 72, 5769, 1967.

O'Brien, B.J. and D.L. Reasoner, Charged-particle lunar environment experiment, In Apollo 14 Preliminary Science Report, NASA SP-272,193, 1971.

Öpik, E.J., The Lunar atmosphere, Planet. Space Sci., 9, 211, 1962.

Öpik, E.J. and S.F. Singer, Escape of gases from the moon, J. Geophys. Res., 65, 3065, 1960.

Repin, R.O., L.E. Nyquist, D. Phinney, and D.C. Black, Isotopic composition of rare gases in lunar samples, Science, 167, 550, 1970.

Robbins, D.E., A.J. Hundhausen, and S.J. Bame, Helium in the solar wind, J. Geophys. Res., 75, 1178, 1970.

Samson, J.A.R., Experimental photoionization cross sections in argon from threshold to 280 Å, J. Opical Soc. Amer., 54, 420, 1964.

Schatten, K.H., Large-scale properties of the interplanetary magnetic field, Rev. Geophys. Space Phy., 9, 773, 1971.

Snyder, C.W., D.R. Clay, and M. Neugebauer, The solar-wind spectrometer experiment, In Apollo 12 Preliminary Science Report, NASA SP-235, 75, 1970.

Snyder, C.W., D.R. Clay, and M. Neugebauer, An impact generated plasma cloud on the moon, Presented at the Second Lunar Science Conference, Houston, Texas, January 11-14, 1971.

Sonett, C.P., D.S. Colburn, and R.G. Currie, The intrinsic magnetic field of the moon, J. Geophys. Res., 72, 5503, 1967.

Vasyliunas, V.M., A survey of low-energy electrons in the evening sector of the magnetosphere with OGO 1 and OGO 3, J. Geophys. Res., 73, 2839, 1968.

Whipple, E.C. Jr., The equilibrium electric potential of a body in the upper atmosphere and interplanetary space, Thesis, George Washington University, Washington, D. C., 1965.

Yeh, T.T.J. and G.K. Chang, Density and flux distributions of neutral gases in the lunar atmosphere, _J. Geophys. Res._, _77_, 1720, 1972.